ELASTO-PLASTIC FRACTURE MECHANICS FINITE ELEMENT ANALYSIS

Emina S. Dzindo, A. Sedmak, B. Petrovski

Innovation Center of Faculty of Mechanical Engineering, University of Belgrade,
Kraljice Marije 16, 11120 Belgrade 35
Republic of Serbia
e-mail: edzindo@mas.bg.ac.rs

ABSTRACT. *The basic aim of this paper is to contribute to the assessment of structural integrity of a cracked combustion chamber, i.e. cylindrical pressure vessel. Toward this end elastic-plastic fracture mechanics parameters were evaluated, which could serve as crack driving forces for any cracked structure. As the relevant paramaters, the J-integral and crack tip opening displacement (CTOD) were chosen and evaluated by the elastic-plastic finite element method. The combustion chamber with an axial surface crack was represented as two-dimensional plane strain elastic-plastic finite element model, in a form of edge cracked plate loaded by remote tensile stress.*

Keywords: finite elements, pressure vessel, elasto-plastic fracture, J-integral

Application of the finite element method to the elasto-plastic fracture mechanics problem was in accordance with ESIS recommendations.Thus the quadrangle eight-nodded isoparametric finite elements were used, while the crack tip singularity was modeled by triangular elements with three independent nodes at crack tip and mid-side nodes and mid-side nodes.

The elasto-plastic stress analysis of solids which conform to plane stress or plane strain conditions is considered. The aim is to develop a working computer code for fracture prediction in ductile materials. Only the essential expressions will be reproduced here for theoretical and numerical treatment.

The mesh consisted of 1421 nodes and 435 elements, what is enough for the type of problem analyzed and required engineering accuracy.

The stress-strain relation was represented also in two different ways - as the bi-linear and as the multi-linear. In the first case two straight line were used with slopes defined by modulus of elasticity (198000 MPa) in the linear elastic range, and by hardening modulus (833 MPa) in the plastic range. The distinction point between these two ranges was yield strength (718 MPa). In the second case 12 points were used, taken from the real uniaxial stress-strain curve. The results for bi-linear curve are given in Table 1 and 2 for multi-linear curve.

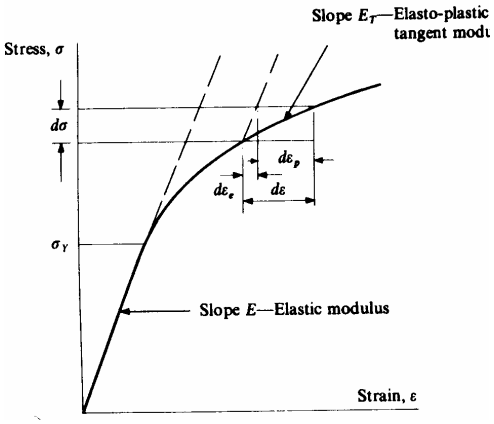

Figure 1. Non-linear stress-strain relation

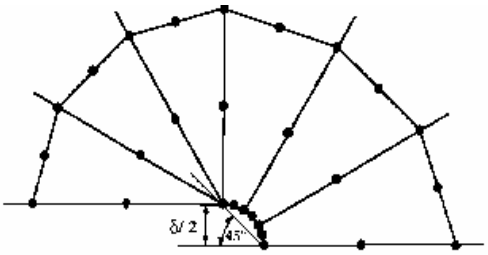

Figure 2. Finite element mesh around crack tip

If problems are investigated, a convergence study with variation of mesh refinement is advisable. "Starting" point in such a study can be mesh similar to the one which is shown in Fig. 2.

Isoperimetric elements with quadratic shape function (8-noded for 2D, 20-noded for 3D) are recommended. Constant strain triangles are also reliable (in global sense), but not capable of crack blunting modeling. The elements should be rectangular with a side ratio close to 1 in the regions of high strain gradients. Skewed elements should be avoided or, if unavoided, integrated by 3x3 points.
In transition region from small to larger elements the side of later one should not be larger more than twice the smaller side of neigh-boring elements.

In the case of non-linear problems stiffness reformation and equilibrium iteration at any time step is recommended, as well as a convergence study concering load/time step increments. Usually one increment should be done with not more than 10 iterations.
There is a good experience with reduced integration (2x2) for the standard 8-node isoperimetric elements. For special cases (large element deformations, curved, skewed or very fine elements) 3x3 integration is necessary.
Nodal point loads often leads to inaccurate deformations.

For elastic analysis use collapsed isoparametric, triangle crack tip elements with one crack-tip node and quarter-point midsize nodes. For elastic-plastic analysis use triangle elements with independent crack-tip nodes and midsize nodes lying in the middle. For simulation of crack growth rectangular elements without singularity can be used. It should be noted that the same element size as with collapsed elements leads to stiffer results.

Table 1 The finite element results displacement loading, bi-linear material

L.F.*	CTOD	CMOD	J-INTEGRAL	m=J/R_{eh}/CTOD
0.10	0.0178	0.0872	20.40	1.60
0.11	0.0202	0.0969	25.15	1.73
0.12	0.0230	0.1072	30.55	1.85
0.13	0.0260	0.1182	36.40	1.95
0.14	0.0296	0.1300	42.70	2.01
0.15	0.0333	0.1422	49.95	2.09
0.16	0.0377	0.1555	57.45	2.12
0.17	0.0426	0.1682	65.48	2.14
0.18	0.0486	0.1830	75.07	2.15
0.19	0.0553	0.1992	85.95	2.16
0.20	0.0637	0.2175	98.79	2.16

For. L.F. (0.10) CTOD graphic evaluations:

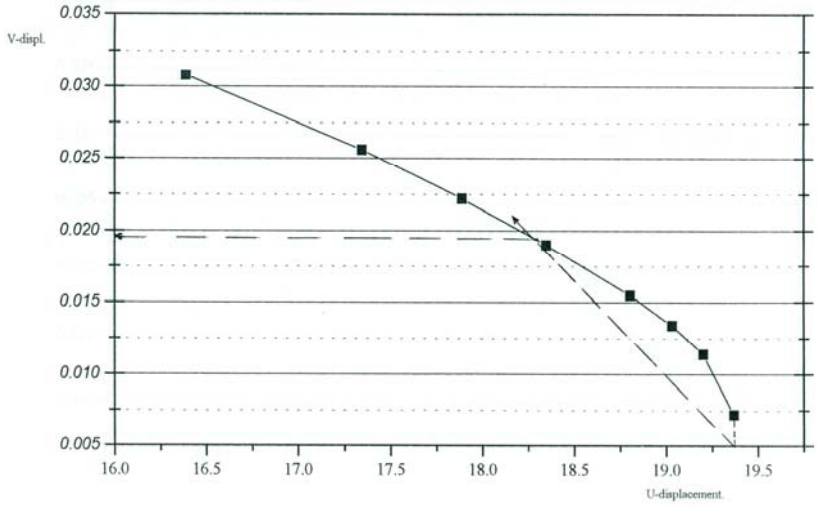

Using finite element method it is an easy task to check the J-integral path independency. As owe can see, the different between J-integral values are not significant and certainly less than numerical error for this type of problem.

If problems are investigated, a convergence study with variation of mesh refinement is advisable. “Starting” point in such a study can be mesh similar to the one which is shown in Fig. 2.

Isoperimetric elements with quadratic shape function (8-noded for 2D, 20-noded for 3D) are recommended. Constant strain triangles are also reliable (in global sense), but not capable of crack blunting modeling. The elements should be rectangular with a side ratio close to 1 in the regions of high strain gradients. Skewed elements should be avoided or, if unavoided, integrated by 3x3 points.

In transition region from small to larger elements the side of later one should not be larger more than twice the smaller side of neigh-boring elements.
In the case of non-linear problems stiffness reformation and equilibrium iteration at any time step is recommended, as well as a convergence study concering load/time step increments. Usually one increment should be done with not more than 10 iterations.

There is a good experience with reduced integration (2x2) for the standard 8-node isoperimetric elements. For special cases (large element deformations, curved, skewed or very fine elements) 3x3 integration is necessary.
Nodal point loads often leads to inaccurate deformations.

For elastic analysis use collapsed isoparametric, triangle crack tip elements with one crack-tip node and quarter-point midsize nodes. For elastic-plastic analysis use triangle elements with independent crack-tip nodes and midsize nodes lying in the middle. For simulation of crack growth rectangular elements without singularity can be used. It should be noted that the same element size as with collapsed elements leads to stiffer results.
Using finite element method it is an easy task to check the J-integral path independency. Toward this end six paths around the crack tip were used and the results given in Tab 5. Difference between J-integral values are not significant and certainly less than the numerical error for this type of problem.

Table 2. Results for J-integral path independency analysis

L.F.*	Path 1	Path 2	Path 3	Path 4	Path 5	Path 6
0.1	19.6	21.0	20.4	20.8	20.4	20.4
0.11	24.0	25.8	25.1	25.6	25.1	25.2
0.12	29.1	31.2	230.5	31.1	30.5	30.7
0.13	34.5	37.0	36.4	37.1	36.4	36.4
0.14	40.2	43.2	42.8	43.8	43.1	43.4
0.15	47.3	50.3	50.0	51.1	50.3	50.8
0.16	54.4	57.7	57.1	59.2	58.4	59.0

Use of the J-integral in elasto-plastic fracture

The J-integral has already been defined by the following expression

$$J = \int_{\Gamma}\left(U\mathrm{d}y - t_i \frac{\partial u_i}{\partial x} \mathrm{d}s \right) \tag{1}$$

For linear elastic problems, the J-integral has been numerically evaluated. For elasto-plastic applications the only change necessary is to employ the appropriate definition of the strain energy density, U. Separating U into its elastic and plastic components $U = U_e + U_p$ caused by then U_e is given by

$$U_p = \frac{1}{2}\sigma_{ij}\left(\varepsilon_{ij}\right)_e \tag{2}$$

where $\left(\varepsilon_{ij}\right)_e$ denotes the elastic components of strain. The value of U_p is obtained by accumulating the incremental work contributions $\overline{\sigma}\, d\overline{\varepsilon}_p$ over the strain path. Since the effective stress $\overline{\sigma}$ and plastic strain increment $d\overline{\varepsilon}_p$ are evaluated during each load increment, then the calculation of U_p is a trivial operation. Subject to the definition of U given by (2), the numerical process by which J is evaluated is given in the following form for an individual element

$$J^{(e)} = \int_{-1}^{+1} \left\{ \frac{1}{2}\left[\sigma_{xx}\left(\varepsilon_{xx}\right)_e + \sigma_{xy}\left(\varepsilon_{xy}\right)_e + \sigma_{yy}\left(\varepsilon_{yy}\right)_e\right]\frac{\partial y}{\partial \eta} + U_p \frac{\partial y}{\partial \eta} - \right.$$
$$\left. - \left[\left(\sigma_{xx}n_1 + \sigma_{xy}n_2\right)\frac{\partial u}{\partial x} + \left(\sigma_{xy}n_1 + \sigma_{yy}n_2\right)\frac{\partial v}{\partial x}\right]\sqrt{\left(\frac{\partial x}{\partial \eta}\right)^2 + \left(\frac{\partial y}{\partial \eta}\right)^2} \right\} d\eta \tag{3}$$

The elastics components of strain can be simply evaluated from the current stresses according to

$$\left(\varepsilon_{xx}\right)_e = \frac{1}{E}\left[\sigma_{xx} - \nu\left(\sigma_{yy} + \sigma_{zz}\right)\right]$$
$$\left(\varepsilon_{yy}\right)_e = \frac{1}{E}\left[\sigma_{yy} - \nu\left(\sigma_{xx} + \sigma_{zz}\right)\right] \tag{4}$$
$$\left(\gamma_{xy}\right)_e = \frac{2\left(1 + \nu\right)}{E}\sigma_{xy}$$

As mentioned previously, the value of U_p at the integrating points within each element is readily available from the standard finite element calculations. Once again the integration is performed numerically using Gaussian quadrature.

This technique, however, placed restrictions on the finite element mesh employed. In the particular, the crack geometry must be idealized by a radial fan of elements centered at the crack tip and the nodal nodal number of the elements through which the contour is to be taken must be such that the local ζ coordinate axes follow the tangential direction. While such an approach allows the numerical process for the evaluation of J to be elegantly formulated, it nevertheless places a considerable restriction on the finite element mesh topology; particularly when automatic mesh generation schemes are to be employed. Therefore in this section we develop a further subroutine for J integral evaluation, which can be applied to arbitrarily structured finite element meshes.

Therefore a deformable measuring zone was designed and placed underneath the tool gearing (fig. 1a). Strain gauges (fig. 1b), installed at the measuring zone (fig. 2), provide information about the deformation of the tool during the whole rolling process.

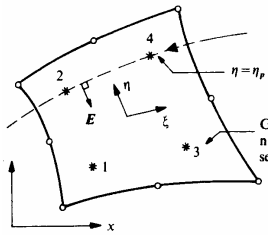

Fig. 1. Contour path along direction of constant η value

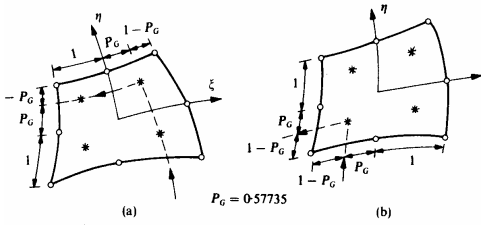

Fig. 2: Contributions from "corner" elements (a)Contributions from elements in which integration is made along paths $\zeta = \zeta_p$ (constant).(b) Contributions from elements in which integration is made along paths $\eta = \eta_p$ (constant).

Then the corresponding unit vector is

$$\mathbf{n}^T = \left[n_1, n_2, 0\right] = \left[\frac{E_1}{L}, \frac{E_2}{L}, 0\right]; \qquad L = \sqrt{E_1^2 + E_2^2} \tag{5}$$

The elemental arc length along the line $\eta = \eta_p$ is

$$d_s = -\sqrt{\left(\frac{dx}{d\xi}\right)^2 + \left(\frac{dy}{d\xi}\right)^2}\, d\xi \tag{6}$$

and also

$$d\,y = \frac{\partial\, y}{\partial\, \xi}\, d\,\xi \tag{7}$$

Then the contribution to the J-integral from an individual element is finally given as

$$J^{(e)} = \int_{-1}^{+1} \left\{ \frac{1}{2}\left[\sigma_{xx}\left(\varepsilon_{xx}\right)_e + \sigma_{xy}\left(\varepsilon_{xy}\right)_e + \sigma_{yy}\left(\varepsilon_{yy}\right)_e\right]\frac{\partial y}{\partial \xi} + U_p \frac{\partial y}{\partial \xi} \right.$$
$$\left. - \left[\left(\sigma_{xx} n_1 + \sigma_{xy} n_2\right)\frac{\partial u}{\partial x} + \left(\sigma_{xy} n_1 + \sigma_{yy} n_2\right)\frac{\partial v}{\partial x}\right]\sqrt{\left(\frac{\partial x}{\partial \xi}\right)^2 + \left(\frac{\partial y}{\partial \xi}\right)^2} \right\} d\xi \tag{8}$$

In designing the pressure vessels, a relatively high safety degree is applied. However, the designed safety degree can be significantly decreased due to insufficient knowledge of all the operating conditions, inadequate quality control during manufacturing, or changes in operating conditions. The sudden and unexpected brittle fracture, which can occur, represents a very serious and important problem in safety analysis and risks estimates. Such a fracture usually occurs either due to reasons like the existing flaw, which can suddenly expand, or due to interaction of an existing flaw and operating conditions influence.

To analyze the life span of this pressure vessel the thin walled cylinder subjected to internal pressure was considered, Figure 3. The cylinder is subjected to internal pressure *p*, it has the wall thickness *t* and diameter *D*. Due to action of the internal pressure appear the lateral and longitudinal stresses, $\sigma_{\theta\theta}$ and σ_{zz}, whose values are defined by expressions:

$$\sigma_{\theta\theta} = \frac{pD}{t} \tag{9}$$

and

$$\sigma_{zz} = \frac{pD}{2t} \tag{10}$$

respectively.

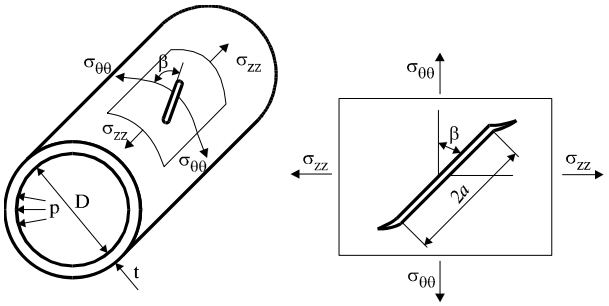

Figure 3. *The cracked thin-walled cylinder subjected to internal pressure*

The critical value of the cylinder wall thickness for the transverse crack, calculated based on the stress expression (9) is:

$$t_{cr,t} = \frac{p \cdot D}{\sigma_{0.2}}, \tag{11}$$

while the critical value of the cylinder wall thickness for the longitudinal crack, calculated based on the stress expression (2) is:

$$t_{cr,l} = \frac{p \cdot D}{2 \cdot \sigma_{0.2}} \tag{12}$$

with $\sigma_{0.2}$ being so-called technical yield stress value.

Results

Finally, it is necessary to consider the case of "corner" elements in which the path of integration changes from the ζ to the η direction (or vice versa) . The two cases which may be encountered are illustrated, where since we are dealing with elasto-plastic problems only a 2 point Gauss rule is considered. For the situation shown in Fig.2(a), the element contribution to J is evaluated in the normal manner by integrating across the complete element dimension according to (6). These values are then scaled to account for the actual shorter path length. The scaling factor S_G for both the ζ and η directions can be readily seen from Fig. 2(a) to be

$$S_G = \left(1 + P_G\right) / 2 = 0.788675 \tag{13}$$

A similar approach is adopted for the situation shown in Fig. (2b) where for this case the scaling factor is seen to be

$$S_G = \left(1 - P_G\right) / 2 = 0.211325 \tag{14}$$

Obviously some degree numerical inaccuracy is introduced by this scaling process, but since the contribution of such corner elements to the complete J integral will be small, then the error involved should be acceptable.

CONCLUSION

The elastic-plastic fracture mechanics parameters evaluated in this these, i.e. J-integral and CTOD, are not sensitive to calculation technique used. In other words, differences in their values, obtained by changing finite element techniques such as modeling the material behaviour (bi-linear or multi-linear) and prescribing the loading (by remote edge forces and by displacements), are not significant

The J-integral is path independent, as shown by its evaluation along six different paths, which is another proof of its correct evaluation. All paths were chosen to be in plastic strain region, which is most ″suspicious″ regarding J-integral path independency problem.

References

[1] ASTM E 1152-91, "Standard Test Method for Determining J-R Curve" *Annual Book of ASTM Standards 1986,* Vol. 04.01. p. 724
[2] Sedmak, A. "Primena mehanike loma na integritet konstrukcije" *Monografija*, Masinski fakultet, Beograd, 2003.
[3] J.W.Hutchinson, P.C.Paris, Stability Analysis of J-controlled Crack Growth, *ASTM STP668, ASMT*, 1979, pp. 37
[4] J. Fawkes, D.J.R.Owen, *Engineering Fracture Mechanics*, Pineridge Press, UK, 1983
[5] Exploitation Cracks in Pressure Vessels and Reservoirs", Monograph, The Fifth International Summer School on Fracture Mechanics, Ed. Sedmak, S. and A. Sedmak, Faculty of Technology and Metallurgy, Belgrade, 1991.

[6] Nikolic, R. R., J. M. Veljkovic, "The two methods for dimensioning the pressure vessels", *Materials Engineering*, Vol 14, 2007, No.4, pp. 8-12.
[7] H.Ş.Mateiu, N.Farbaş, T.Fleşer, R.Pascu, Research Concernig Damage State Assessment of Heat Resistant Steels Used for Power Plant Components, *Integritet i Vek Konstrukcija* **3**, ISSN 14151-3749, 2(2003), 51-64.
[8] J.Kurai, Z.Burzić, N.Garić, M.Zrilić, B.Aleksić, Initial Stress State of Bolier Tubes for Structural Integrity Assessment, *Integritet i Vek Konstrukcija* **7**, ISSN 14151-3749, 3(2007), 187-194.

DETERMINATION OF DETONATION PRODUCTS EQUATION OF STATE USING CYLINDER TEST

Predrag Elek[1], Vesna Džingalašević[2], Slobodan Jaramaz[1], Dejan Micković[1]

[1]University of Belgrade, Faculty of Mechanical Engineering,
Kraljice Marije 16, 11120 Belgrade 35, Serbia
e-mail: pelek@mas.bg.ac.rs
sjaramaz@mas.bg.ac.rs
dmickovic@mas.bg.ac.rs
[2]Military Technical Institute
Ratka Resanovića 1, 11132 Belgrade, Serbia
e-mail: dzingalasevic@sezampro.rs

Abstract. Contemporary research in the field of explosive applications implies utilization of „hydrocode“ simulations. Validity of these simulations strongly depends on used parameters in the equation of state for considered explosive compounds. A new analytical model for determination of Jones-Wilkins-Lee (JWL) equation of state parameters based on cylinder test has been proposed. The model relies on analysis of cylinder motion and detonation products expansion. Available cylinder test data for five explosive compositions are used for calculation of JWL parameters. Good compatibility between results of the model and the literature data is observed, justifying suggested analytical approach.

Keywords: explosive, detonation, cylinder test, JWL equation of state

1. Introduction

Modern approach to research in the field of explosive applications includes the use of so-called “hydrocodes” [1] – robust programs for numerical simulation of complex, high-energy physical-chemical processes involving the detonation, shock waves, large strains, high strain rates, etc. Validity of these simulations highly depends on the used equation of state of detonation products of explosive composition considered. There are a number of proposed equations that define the isentrope of gaseous detonation products [2], [3]: polytropic expansion law, Williamsburg, LJD (Lennard-Jones-Devonshire), BKW (Becker-Kistiakowsky-Wilson) and JWL (Jones-Wilkins-Lee). For simplicity, greater accuracy and availability of data for a significant number of explosive compositions, the most frequently used is the empirical JWL equation of state of detonation products, which has the form [4]:

$$p = A\mathrm{e}^{-R_1 V} + B\mathrm{e}^{-R_2 V} + CV^{-(1+\omega)} \tag{1}$$

where p is the pressure of detonation products, $V=\rho_0/\rho$ is expansion ratio of detonation products, while A, B, C, R_1, R_2 and ω are parameters determined by comparison with experimental results. The first term of the equation defines the behavior of detonation products at very high pressures and low expansion ratio, the second addend is related to the mean pressure, and the third term describes the isentrope in the domain of low pressure, i.e.

large expansion ratio. In this context, only the parameter ω has a physical meaning and approximately satisfies the relation:

$$\omega = \gamma - 1 , \tag{2}$$

where γ is polytropic constant for detonation products at pressures close to atmospheric.
There are two ways to determine the JWL parameters of equation of state: (i) by use a thermo-chemical code, (ii) using some of the tests. The former method implies a semi-empirical program that can predict a chemical reaction using thermodynamics, and will not be considered here. The latter approach is based on detonation products expansion physics, it is more reliable and will be further investigated.
The most common source of experimental data to obtain parameters of JWL equation of state is the cylinder test [5], [6], [7] and [8]. Standard copper tube is filled with explosive of interest and the planar detonation wave (normal to the cylinder axis) is generated. As the detonation wave passed through observed section, the radial displacement of copper tube obscure the backlighting (provided e.g. by an argon light bomb) and the history of displacement is recorded by streak camera (Fig. 1).

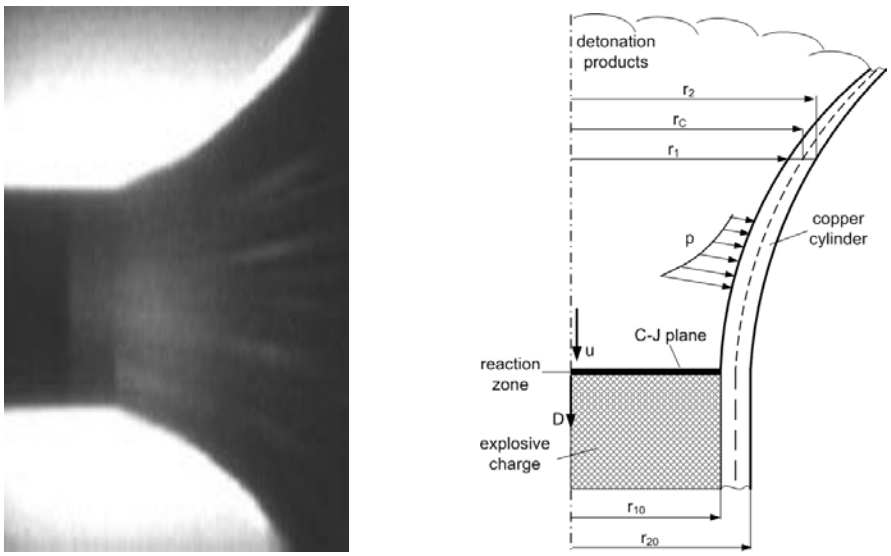

Figure 1. Cylinder test: a) streak camera record, b) motion of copper tube under the action of detonation products (geometry and notation)

The original way of determining the parameters of JWL equation of state [4] implied the variation of their values in a hydrocode, until a satisfactory correspondence between numerical and experimental results is obtained. It was also proposed several different ways of determining the unknown parameters of equations of state without applying the hydrocodes, e.g. [9], [10] and [11].
The aim of this paper is to propose a new analytical model for simple and reliable determination of unknown parameters of JWL equation of state based on the results of the cylinder test.

2. Model

Presented analytical model is based on integration of energetic approach [12] and the concept of the cylinder motion due to the detonation products pressure [13]. These models are analyzed in detail in [14].

Approximation of measured cylinder displacement. The result of experiment is the curve obtained by high-speed photography that represents history of the cylinder outer surface displacement:

$$\Delta r_2 = r_2 - r_{20} = f(t)\,. \tag{3}$$

This function is usually represented in discrete form

$$\left(t_i,\ (\Delta r_2)_i\right),\ i = \overline{1,\ n}\,, \tag{4}$$

where n is total number of measured points from the camera record.
In order to calculate tube wall velocity and acceleration, it is necessary to approximate experimental results (4) with a proper function. Analysis of a large number of possible functions showed that the two functions very well describe the results of experiments. The first function [15] has the form:

$$F_1(t) = \frac{v_\infty t g(t)}{\frac{2v_\infty}{a_0} g'(0) + g(t)}\,, \tag{5}$$

where a_0 is initial cylinder acceleration, v_∞ is asymptotic radial cylinder velocity, and function $g(t)$ is defined as:

$$g(t) = \left(1+t\right)^\sigma - 1\,. \tag{6}$$

Using numerical optimization methods, parameters a_0, v_∞ and σ are determined providing minimum deviation of function (5) from experimental results (4) in the sense of the least square method.
Different function, based on the assumption of exponential drop of detonation products pressure, is proposed in [l3]:

$$F_2(t) = \sum_{i=1}^{2} a_i \left[b_i t - \left(1 - e^{-b_i t}\right)\right], \tag{7}$$

where a_i, b_i (i=1,2) are parameters to be optimized.
For each experimental result, parameters in functions (5) and (7) are determined, and the function with better approximation of experiment is used for further calculation, so we have:

$$\Delta r_2 = F(t)\,. \tag{8}$$

We will assume that the cylinder motion is defined by displacement of the central cylinder surface, defined by relation:

$$r_2^2 - r_c^2 = r_c^2 - r_1^2 = \frac{1}{2}\left(r_{20}^2 - r_{10}^2\right). \tag{9}$$

Central surface displacement $\Delta r_c = F_c(t)$ and displacement of internal surface Δr_1 are easily obtained from (8) and (9).

Cylinder velocity and acceleration. Kinematics of the system was determined as described in [13] and [16]. Differentiation of the optimized function of central surface displacement gives the values of "apparent" velocity and acceleration of the cylinder:

$$v_a = \frac{\mathrm{d}F_c(t)}{\mathrm{d}t}, \quad a_a = \frac{\mathrm{d}^2F_c(t)}{\mathrm{d}t^2}. \tag{10}$$

Analysis of the motion of cylindrical liner shows that inclination centerline angle θ can be determined from relation:

$$v_a = D\tan\theta. \tag{11}$$

The real values of cylinder velocity and acceleration are:

$$v = 2D\sin\frac{\theta}{2}, \quad a = a_p\cos^3\theta. \tag{12}$$

Pressure of detonation products. Since the cylinder acceleration is determined, the pressure of detonation products can be determined from the equation of motion of an elementary cylinder part, taking into account the strength of the cylinder [17], considering that the circular stress is dominant:

$$p = \frac{\left(M + \frac{C}{2}\right)a}{2\pi r_1} + \sigma_f\left(\frac{r_2}{r_1} - 1\right). \tag{13}$$

In equation (13), M and C are the cylinder and explosive charge mass per unit length, respectively:

$$M = \pi\rho_m\left(r_{20}^2 - r_{10}^2\right), \quad C = \pi\rho_0 r_{10}^2, \tag{14}$$

where ρ_m and ρ_0 are densities of metal and explosive.
Flow stress of the cylinder σ_f is determined by empirical Johnson-Cook model [18]:

$$\sigma_f(\varepsilon, \dot{\varepsilon}, T) = \left[A + B\varepsilon^n\right]\left[1 + C\ln\dot{\varepsilon}^*\right]\left[1 - (T^*)^m\right]. \tag{15}$$

where ε is the equivalent plastic strain, $\dot{\varepsilon}$ is the plastic strain-rate and A, B, C, n, m are material constants. The normalized strain-rate and temperature in equation (15) are defined as:

$$\dot{\varepsilon}^* = \frac{\dot{\varepsilon}}{\dot{\varepsilon}_0}, \quad T^* = \frac{T - T_0}{T_m - T_0}, \tag{16}$$

where $\dot{\varepsilon}_0$ is the effective plastic strain-rate of the quasi-static test used to determine the yield and hardening parameters A, B and n; T_0 is a reference temperature, and T_m is a reference melt temperature. In the present analysis, the influence of thermal softening is neglected due to extremely short time nature of the process.

Detonation products expansion ratio. If it is assumed that the flow of detonation products is quasi-one-dimensional, the continuity equation applies in the form:

$$\rho_0 A_0 D = \rho A(D-u)\,, \tag{17}$$

where u, ρ and A are current values of velocity and density of detonation products, and the channel cross-section area. Using the equation of continuity and Bernoulli equation, we get [19]:

$$\left(\frac{M}{C}+\frac{1}{2}\right)\frac{v^2}{2} = \frac{p}{\rho_0}\frac{A}{A_0} - Du\,. \tag{18}$$

Combining relations (17) and (18), expansion ratio can be determined from

$$V = \frac{\rho_0}{\rho} = \frac{A}{A_0}\left[1 - \frac{A}{A_0}\frac{p}{\rho_0 D^2} + \frac{1}{2}\left(\frac{M}{C}+\frac{1}{2}\right)\left(\frac{v}{D}\right)^2\right], \tag{19}$$

where A/A_0 is the geometric expansion ratio:

$$\frac{A}{A_0} = \left(\frac{r_1}{r_{10}}\right)^2. \tag{20}$$

Energy balance. Energy conservation law for the system consisting of explosive charge and metallic cylinder can be written in form:

$$\rho_0 DA\Delta t\left(U - Q + \frac{u^2}{2} + T_{\text{kin}} + A_{\text{def}}\right) = puA\Delta t\,. \tag{21}$$

In eq. (21) U is internal energy of detonation products per unit mass, Q – detonation heat per unit mass, u – velocity of detonation products in axial direction, T_{kin} – kinetic energy of radial motion of cylinder and gases (Gurney energy) per unit mass of explosive, and A_{def} – cylinder deformation work per unit mass of explosive charge. Eq. (21) can be simplified to the form:

$$E - E_0 + \frac{\rho_0 u^2}{2} + E_{\text{kin}} + W_{\text{def}} = p\frac{u}{D}\,, \tag{22}$$

where $E=\rho_0 U$, and $E_0=\rho_0 U$ are internal energy and detonation heat per unit volume of explosive charge, $E_{\text{kin}}=\rho_0 T_{\text{kin}}$ and $W_{\text{def}}=\rho_0 A_{\text{def}}$ are Gurney energy and deformation work per unit volume of explosive charge.
Detonation heat E_0 is readily obtained by thermo-chemical analysis or from the experiment. Detonation products mass velocity is determined by:

$$u = D\left(1 - V\frac{A_0}{A}\right). \tag{23}$$

Specific Gurney energy can be calculated from [17]:

$$E_{\text{kin}} = \frac{\rho_0 v_1^2}{2}\left[\frac{M}{C}\left(\frac{r_1}{w}\right)^2 \ln\left[1+\left(\frac{w}{r_1^2}\right)^2\right]+\frac{1}{2}\right], \tag{24}$$

where v_1 is the internal cylinder surface velocity and w is defined as:

$$w^2 = r_{20}^2 - r_{10}^2. \tag{25}$$

Deformation work can be calculated from relation:

$$W_{\text{def}} = \frac{\sigma_y + \sigma_f}{2}\left[\left(\frac{r_{20}}{r_{10}}\right)^2 - 1\right]\ln\frac{r_1 + r_2}{r_{10} + r_{20}}, \tag{26}$$

where σ_f is the cylinder material yield stress.
Introducing the energy term:

$$E_1 = p\frac{u}{D} - \frac{\rho_0 u^2}{2}, \tag{27}$$

one can get energy equation (22) in the form:

$$E = E_0 + E_1 - E_{\text{kin}} - W_{\text{def}}, \tag{28}$$

that enables determination of the internal energy E of detonation products.

Internal energy of detonation products. Assuming adiabatic expansion of detonation products and having in mind Eq. (1), internal energy of gases is determined by:

$$E(V) = \int_V^\infty p\,\mathrm{d}V = \frac{A}{R_1}\mathrm{e}^{-R_1 V} + \frac{B}{R_2}\mathrm{e}^{-R_2 V} + \frac{C}{\omega}V^{-\omega}. \tag{29}$$

Since internal energy $E(V)$ is calculated from eq. (28), unknown JWL equation of state parameters A, B, C, R_1, R_2, and ω can be optimized in order to fit Eq. (29).
At the same time, the JWL parameters should satisfy three additional conditions:
(i) pressure at the Chapman-Jouget (CJ) state is equal to the experimentally determined value p_{CJ}:

$$A\mathrm{e}^{-R_1 V_{CJ}} + B\mathrm{e}^{-R_2 V_{CJ}} + C V_{CJ}^{-(1+\omega)} = p_{CJ}, \tag{30}$$

(ii) internal energy of detonation products at the CJ state is:

$$\frac{A}{R_1}\mathrm{e}^{-R_1 V} + \frac{B}{R_2}\mathrm{e}^{-R_2 V} + \frac{C}{\omega}V^{-\omega} = E_0 + \frac{\rho_0 u_{CJ}^2}{2}, \tag{31}$$

(iii) slope of the Rayleigh line is determined by:

$$AR_1 e^{-R_1 V_{CJ}} + BR_2 e^{-R_2 V_{CJ}} + C(1+\omega) V_{CJ}^{-(2+\omega)} = \rho_0 D^2 . \quad (32)$$

Algorithm for determination of JWL parameters. The procedure for determination of JWL equation of state parameters from the cylinder test is presented in flowchart (Fig. 2). Eq. (13) provides the initial detonation products pressure p_{initial}. This value is based on the second derivative of the fitting function $F_c(t)$ and therefore cannot be used as the definitive pressure of detonation products. Instead, p_{initial} is used for calculation of internal energy E, and then JWL parameters are optimized by fitting procedure, providing the new value for detonation product pressure p. Procedure is repeated with the new value of pressure until the difference between two pressures becomes small enough.

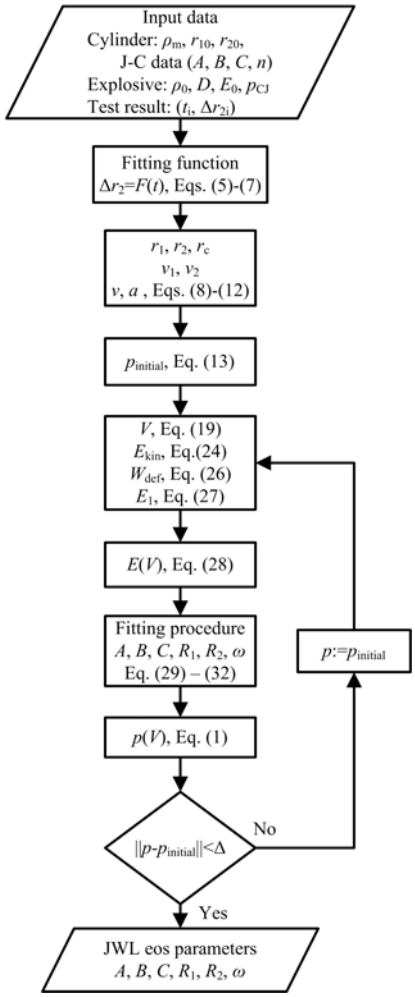

Figure 2. Algorithm for determination of JWL equation of state parameters from the cylinder test

3. Model results and comparison with experimental data

Presented model is applied to determination of the parameters of JWL equation of state for five explosives. Properties of the copper cylinder are listed in Table 1 [18] and [20]. Characteristics of tested explosives are given in Table 2 (all data are taken from [20], except for FH-5 [14]). Experimental cylinder test data (t_i, $(\Delta r_2)_i$) are also used from [20] and [14].

Table 1. Characteristics of copper cylinder

Density	**Dimension**		**Flow stress parameters by Johnson-Cock model**			
ρ_m (kg/m^3)	r_{10} (mm)	r_{20} (mm)	A (MPa)	B (MPa)	C	n
8940	12.70	15.30	89.63	291.6	0.025	0.31

Table 2. Detonation properties of examined explosive compositions

Explosive composition	**Density**	**Detonation velocity**	**Pressure at CJ state**	**Detonation heat**
	ρ_0 (kg/m^3)	D (m/s)	p_{CJ} (GPa)	E_0 (GPa)
TNT	1630	6930	21.0	7.0
Composition B (RDX/TNT-64/36)	1717	7980	29.5	8.5
PBX (HMX/NC/CEF-94/3/3)	1840	8800	37.0	10.2
HMX	1891	9110	42.0	10.5
FH-5 (RDX/W-95/5)*	1600	7930	24.96	8.7

* cylinder dimensions for FH-5 test: r_{10}=10.20 mm, r_{20}=12.70 mm

Model results for the cylinder test with TNT will be presented as a representative example. Experimentally determined cylinder displacement is fitted with analytical functions defined by Eq. (5) and (7). Exponential function (7) provided better agreement with experimental data in this case (Fig. 3).

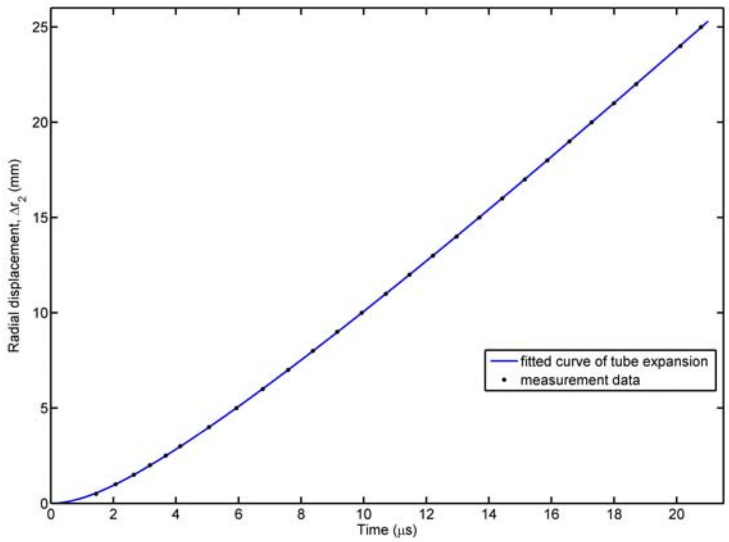

Figure 3. Experimental tube expansion data for TNT [20] fitted with analytical function (7)

Calculated evolution of internal and external cylinder radii is shown in Fig. 4.

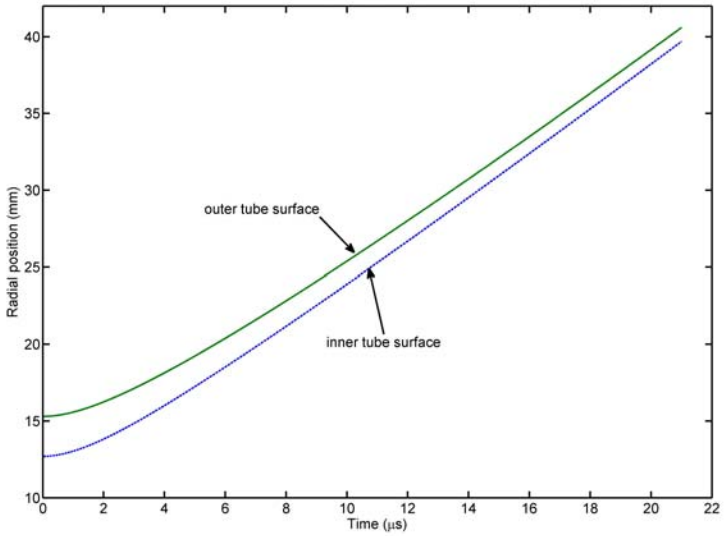

Figure 4. Computed radial position of inner and outer cylinder surface for TNT cylinder test

Velocity histories for both inner and outer tube surface are presented in Fig. 5. The Gurney limit velocity is also indicated (for TNT, literature data [20] v_G=2440 m/s is used), showing good accordance with calculated external cylinder surface velocity.

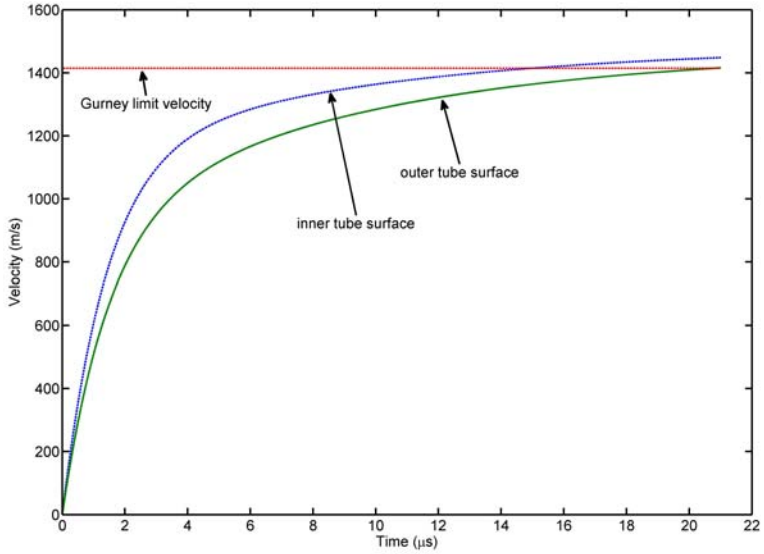

Figure 5. Computed velocities of inner and outer cylinder surface and the Gurney limit velocity

Determined expansion ratio V is compared to the geometric expansion ratio (Fig. 6):

$$V_{\mathrm{g}} = \frac{A}{A_0} = \left(\frac{r_1}{r_{10}} \right)^2 . \tag{33}$$

Significant deviation is noted, especially for very low and very high expansions. This means that simple calculation of expansion ratio by Eq. (33) is not sufficiently accurate.

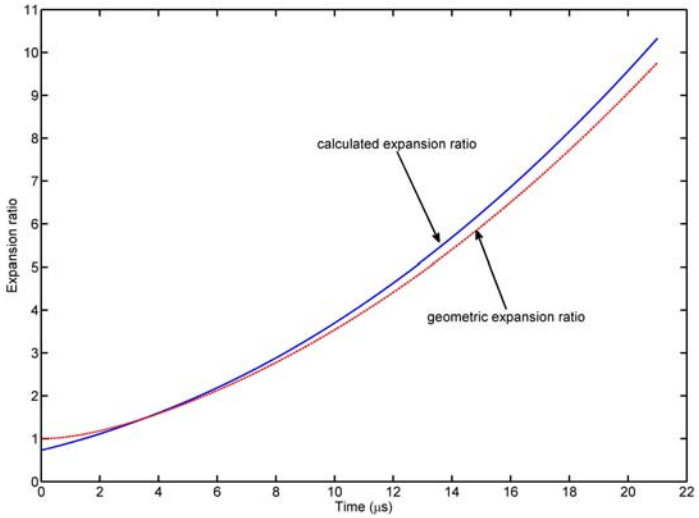

Figure 6. Detonation products expansion ratio from the model compared with simple geometric expansion ratio

Specific energy balance as a function of expansion ratio is given in Fig. 7. The known specific detonation energy E_0, and computed values of kinetic energy E_{kin}, deformation work W_{def} and specific energy E_1 enable determination of specific internal energy $E(V)$.

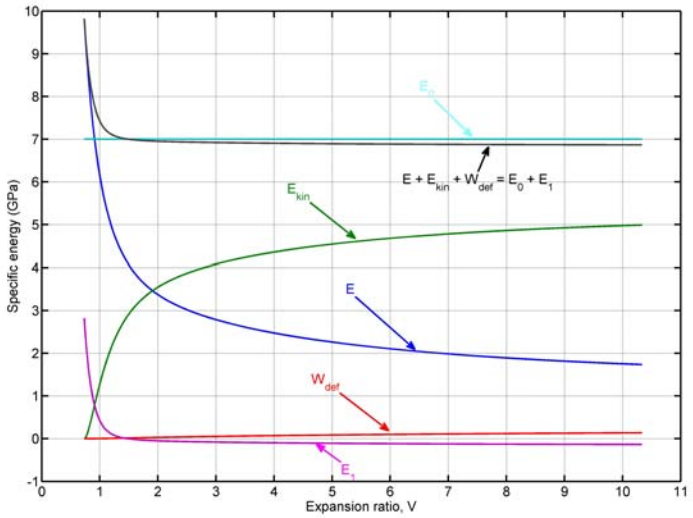

Figure 7. Balance of specific energies involved in the process of detonation product expansion in cylinder test

Specific internal energy of detonation products $E(V)$ obtained by the proposed model is compared with the literature curve (Fig. 8). Good agreement between model and literature curve can be noted.

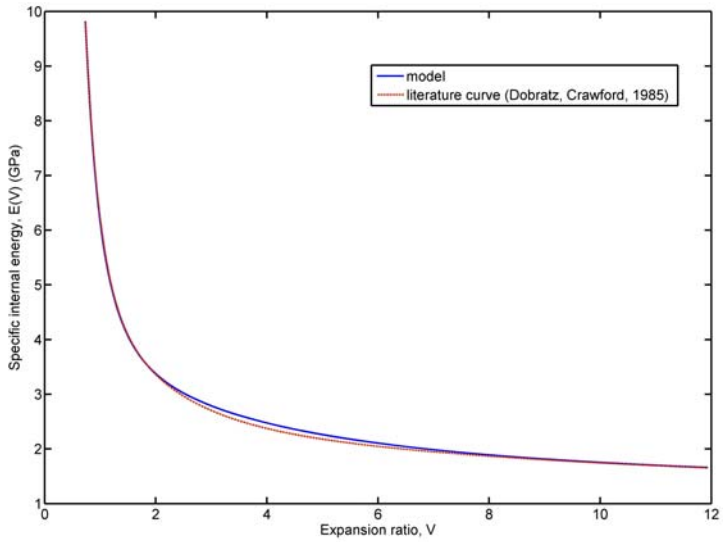

Figure 8. Comparison of calculated specific internal energy of detonation products with literature data

Fig. 9 shows the contribution of the three terms of JWL equation of state to the specific internal energy, after the fitting procedure. It is confirmed that the third term in Eq. (29) is

equal to the whole internal energy for large expansions (V>6), and the first term can be neglected for small expansion (V<2.5)

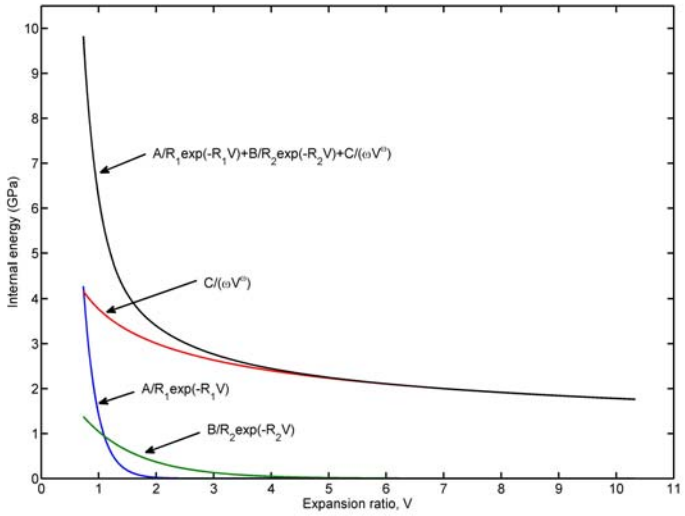

Figure 9. Specific internal energy of TNT detonation products as the sum of three term of JWL model

After the fitting procedure, obtained parameters are used to determine detonation products pressure curve that is compared with the literature data [20] (Fig. 10). Very good compatibility of these results is evident.

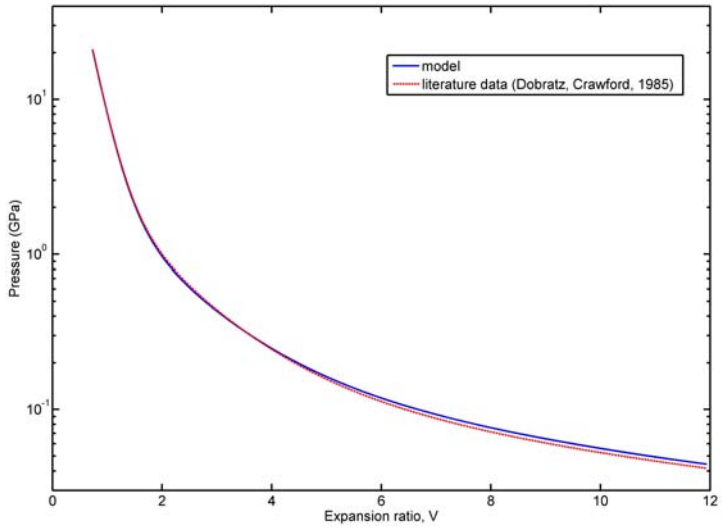

Figure 10. Comparison of p-V curves for TNT detonation products obtained by presented model and [20]

Calculated JWL parameters for all considered explosive compositions are presented in Table 3, along with literature data. Good agreement of model and literature p-V curves has been obtained.

Table 3. JWL parameters for five explosives – comparison of model results and literature data

Explosive	Method	R_1	R_2	ω	A (GPa)	B (GPa)	C (GPa)
TNT	model	4.1245	0.9436	0.3135	366.42	2.6983	1.1480
	lit. [20]	4.15	0.95	0.3	371.21	3.2306	1.0453
Comp B	model	4.0489	0.7833	0.3460	497.08	3.4246	1.1260
	lit. [20]	4.2	1.1	0.34	524.23	7.6783	1.0082
HMX	model	4.2018	1.1078	0.3072	768.74	1.2131	7.8843
	lit. [20]	4.2	1.0	0.30	778.28	7.0714	0.6430
PBX-9404	model	4.5403	1.3255	0.3007	832.26	1.7768	9.9479
	lit. [20]	4.60	1.30	0.38	852.40	18.020	1.2070
FH-5	model	4.2750	0.3175	0.2178	573.43	0.96006	0.82373

4. Conclusion

The paper considers problem of determination of detonation products JWL equation of state parameters from the cylinder test data. To solve this problem, a new analytical model has been proposed. The model is based on: (i) fitting the experimental data with analytical function, (ii) cylinder kinematics, (iii) cylinder motion dynamics, (iv) detonation products expansion analysis, (iv) energy balance, and (v) final fitting of detonation products internal energy. Computer program based on the model has been developed. Cylinder test data for five explosive compositions are used for calculation of JWL parameters. Extensive analysis indicates good compatibility between results of the model and the literature data.

Acknowledgement. This research has been supported by the Ministry of Education and Science, Republic of Serbia, through the project III-47029, which is gratefully acknowledged.

References

[1] Zukas J (2004) *Introduction to hydrocodes*, Elsevier Science
[2] Fickett W and Davis WC (2001) *Detonation: Theory and Experiment*, Dover Publications, New York
[3] Davis WC (2003) Shock waves; rarefaction waves; equations of state, in: *Explosive Effects and Applications*, JA Zukas and WP Walters (Eds), Springer
[4] Lee EL, Hornig HC, Kury JW (1968): *Adiabatic Expansion of High Explosive Detonation Products*, UCRL-50422, Livermore, California
[5] Hill LG, Catanach RA (1998) *W-76 PBX-9501 Cylinder test*, Los Alamos National Laboratories
[6] Reaugh JE, Souers PC (2004) A constant-density Gurney approach to the cylinder test, *Propellants, Explosives, Pyrotechnics*, 29 (2), pp. 124-128
[7] Souers PC, Haselman LC (1994) *Detonation Equation of State at LLNL,* LLNL, UCRL-ID-116113
[8] Džingalašević V, et al (2007) Cylinder test – develoment of the method for determination of the Gurney energy of explosves, *2nd Scientific Conference OTEH 2007*, Belgrade
[9] Polk JF (1981) Determination of equation of state of explosive detonation products from the cylinder expansion test, *6th International Symposium on Ballistics*, Orlando, USA
[10] Bailey WA et al (1981) Explosive equation of state determination by the AWRE method, *7th Symposium (International) on Detonation*, Annapolis, USA

[11] Ijsselstein RR (1986): On the expansion of high-explosive loaded cylinders and JWL equation of state, *9th International Symposium on Ballistics*, Shrivenham, UK
[12] Miller PJ, Carlson KE (1989) Determining JWL Equation of State Parameters using the Gurney Equation Approximation, *9th Symposium on Detonation*, Portland, Oregon, SAD, pp. 930-936
[13] Lan I-F et al (1993) An improved simple method of deducing JWL parameters from cylinder expansion test, *Propellants, Explosives, Pyrotechnics*, 18, pp. 18-24
[14] Elek P, Džingalašević V, Antić G, Jaramaz S (2009) Analytical approach to determination of JWL detonation products equation of state parameters from the cylinder test, *3rd Scientific-professional conference – OTEH 2009*, Belgrade
[15] Hill LG (1997) Detonation products equation-of-state directly from the cylinder test, *21st International Symposium on Shock Waves*, Great Keppel Island, Australia
[16] Hornberg H (1986) Determination of fume state parameters from expansion measurements of metal tube, *Propellants, Explosives, Pyrotechnics*, 11, pp. 23-31
[17] Elek, P (2008) Modeling of dynamic fragmentation in terminal ballistics, PhD dissertation, University of Belgrade – Faculty of Mechanical Engineering, Belgrade
[18] Johnson GR, Cook WH (1983) A constitutive model and data for metals subjected to large strains, high strain rates and high temperatures, *7th International Symposium on Ballistics*, The Hague
[19] Taylor GI (1963) *Scientific papers of sir Geoffrey Ingram Taylor,* edited by G.K. Batchelor*,* Vol. 3. Aerodynamics and the Mechanics of Projectiles and Explosions, Cambridge University Press
[20] Dobratz BM, Crawford PC (1985) *LLNL Explosives handbook: Properties of chemical explosives and explosive simulants*, UCRL-52997 Change 2, 1985.

METHODS OF VERIFYING THE FREQUENCY RESPONSE FUNCTIONS QUALITY IN MODAL TESTING

Valentina Golubović-Bugarski[1], Drago Blagojević[2], Jovan Škundrić[3]

[1, 2, 3] Faculty of Mechanical Engineering,
The University of Banja Luka, Stepe stepanovića 71, 78000 Banja Luka, RS, BiH
e-mail: valentina@urc.rs.ba, dbl@urc.rs.ba

Abstract. The paper presents examples of modal testing of the beam like structure. Modal testing is a form of vibration testing of mechanical structures which is performed in order to determine the modal model of the mechanical structure from the frequency response functions (FRF) data. The accuracy of measurement is the ability to accurately quantify the behavior of the test structure. Reducing the accuracy of measurement can arise from two sources: inability to measure the movement of the structure without affecting the measurement hardware to dynamic structure; inability to quantify the signal provided by sensors. During preliminary measurements, but also during the execution of the overall modal testing, one must run some checks to assess the quality of measured data. There are several techniques which application checks the quality of data, e.g. reciprocity test (Maxwell's rule of reciprocity), the repeatability test and coherence function. The repeatability and reciprocity test are performed almost always by visual inspection of recorded FRFs in order to identify whether there are some important differences between them. A good indicator of repeatability and reciprocity test is the difference ΔFRF of constituent FRFs which are compared. The coherence function shows a correlation between the measured excitation and response signals, calculated for each frequency. These techniques applied to verify the accuracy of the modal test are illustrated by an example of modal testing of freely supported beam and cantilever beam.

1. Introduction

Modal testing is a form of vibration testing which is performed in order to provide a set of Frequency Response functions (FRFs) that are sufficiently extensive and accurate to enable analysis and extraction of the properties for all the required modes of structure. There is no single right way to perform any vibration test. In almost every case the support, the excitation equipment or the transducers will influence the dynamic behavior of the article under test. Every structure poses its own special problems for modal testing and there are many different ways to treat the same problem. There is no definitive right way to test any given structure. All modal tests involve degree of compromise and the test engineer is encouraged to consider all aspects of the test set-up, test equipment, data collection and assessment at an early stage. Preparatory work is esential prerequisite for successful modal testing. Unfortunately, this key stage is often rushed in the bustle to collect data.

Many of the potential problems with modal testing only become apparent during the actual test. Frequently, it is not possible to predict such problems beforehand either because there is no analytical model or because the model of the structure is unrepresentative. For this reason it is advocated strongly that a preliminary survey should be performed prior to the full measurement survey.
As a part of preliminary survey and during the full survey critical assessments of the quality of the measured data should be made. Reciprocity and repeatability are two established methods for assessing the quality of measured data. However, it has been found that much of information that could be derived from these checks is lost because the respective FRFs are only compared by eye. Consequently, small differences between two large quantities are invariably overlooked despite the fact that the differences may be systematic and indicative of slight shifts in the structural resonance frequencies. To aid the assessment of data quality by these methods, the use of 'difference functions' alongside the actual FRFs has been found to be particularly beneficial [1].

2. Basic principles in modal testing

Theoretical modal analysis shows that any mechanical system can be described by the matrix of transfer functions of the system [H(ω)] or in short system matrix. Elements of the system matrix in the frequency domain are the frequency response functions FRFs (α_{ij}), which describe the relationship between outputs and inputs, i.e. response and excitation between two points on the structure and, therefore, modal testing can be described by the principle of "black box", Figure 1.

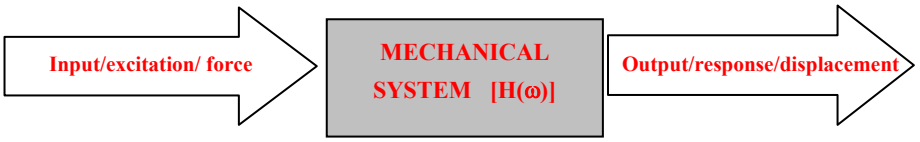

$$\{X(\omega)\} = [H(\omega)]\{F(\omega)\}$$

$$\alpha_{ij}(\omega) = \frac{X_i(\omega)}{F_j(\omega)} = \frac{\text{Output}}{\text{Input}} = \frac{\text{Response}}{\text{Excitation}} = \frac{\text{Displacement}}{\text{Force}}$$

Figure 1. Block diagram of FRF

In the experimental modal analysis defined force is the input, i.e. excitation of the structure at the j-th point. Response of the structure to the given excitation at the j-th position can be expressed by displacement, velocity or acceleration at the i-th position of the structure. Each FRF contains global modal parameters: natural frequencies and damping. Each row or column of FRFs matrix contains all modal shapes. Therefore, to define the modal model of the mechanical system at least one row or one column of FRFs matrix should be measured. As real structure is the object of modal testing, it should be discretised, i.e. final number of degrees of freedom should be defined, Figure 2. The number of measuring degrees of freedom is the number of physical locations on a structure in which we performed

measurement multiplied by the number of measurements performed on each of these locations (directions of measurement).

$$\begin{bmatrix} X_1(j\omega) \\ X_2(j\omega) \\ X_3(j\omega) \\ . \\ . \\ . \end{bmatrix} = \begin{bmatrix} . & . & . & h_{11}(j\omega) & . & . & . \\ . & . & . & h_{21}(j\omega) & . & . & . \\ . & . & . & h_{31}(j\omega) & . & . & . \\ . & . & . & . & . & . & . \\ . & . & . & . & . & . & . \\ . & . & . & . & . & . & . \end{bmatrix} \begin{bmatrix} . \\ . \\ F_7(j\omega) \\ . \\ . \\ . \end{bmatrix}$$

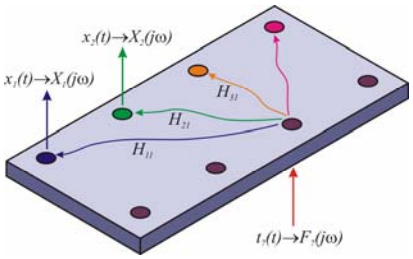

Figure 2. Measurement of FRF on the discretised structure

Before starting any modal test it is important to have a clear definition of the objectives of the test. The type of test, the extent of test and the required quality of the results all follow from the defined objectives of the test. In general, the requirement is usually of the form "to obtain a dynamic model of a structure that is suitable for a given purpose". The purpose of the test may be:

- to obtain mode frequencies of the structure;
- to obtain mode shapes and damping information for the structure;
- to correlate a FE model of the structure with measured results from the real structure;
- to obtain a dynamic model of the structure that can then be used to assess the effects of a range of modification to that structure;
- to obtain a dynamic model that is suitable for updating a FE model of that structure such that the theoretical model is a better representation of the dynamic characteristic of the real structure than it was previously.

The quality and extant of the modal test required to achieve these aims increases as one progresses down the list.

In modal testing, four basic assumptions are introduced concerning any observed structure:

1. The investigated structure is linear, i.e. the response of the structure to any combination of forces that act simultaneously represents the sum of individual responses equivalent to each force acting alone. For most structures this assumption is good for a limited range. However, it frequently happens that the real structures have some degree of nonlinearity due to nonlinear dynamic characteristics of the joints, boundary conditions and material properties. In practical effect, these structures are considered as linear, as long as the degree of nonlinearity is small and irrelevant to the scope of response of structure that is of interest.
2. The structure is time invariant, i.e. parameters be determined are not changing in time.
3. The structure is subjected to Maxwell's rule of reciprocity, i.e. excitation force applied to the j-th position causes response to the i-th position, which is the same

as the response to the j-th position caused by the excitation force for the same i-th position. Regarding the FRFs, the rule of reciprocity is such that the FRF determined by excitation in the j-th and response in the i-th is the same as FRF determined by excitation in the i-th and response in the j-th ($\alpha ij=\alpha ji$).

4. The structure should be observed, i.e. measured excitation and response of the structure contain sufficient information necessary for generating adequate model of structure behavior. The structures and machines that have such degrees of freedom which are not mensurable, are not fully observed. In practice, the most common situation is that the measurement is limited to some frequency band, so the data can be used for the formation of an incomplete model of the structure.

The basic assumptions are almost never fully satisfied in measuring the real structure, i.e. the assumptions will be approximately correct. Each of the assumptions could be confirmed experimentally, either during testing or after testing and data analysis.

3. Quality of measured data in modal testing

Measurement accuracy is the ability to quantify the behavior of the structure precisely. A lack of accuracy in test measurements may arise from two sources:

- The inability to measure the motion of the structure without affecting its behavior
- The inability to quantify the transducers signals.

Once the transducer and conditioning equipment have converted the force or response quantities into electrical signals, the signals have to be quantified. Nowadays, the measurement instrumentation is primarily digital in nature and a large proportion of the errors in quantification of these signals are associated with details of digital signal processing.

During the preliminary survey, and throughout the full modal test, some checks should be made to assess the quality of measured data. There are several techniques already in general use that can provide an indication of the quality of the measured data: reciprocity, repeatability and coherence.

4. One example of modal testing

Modal testing of beam like structure was carried out with the aim to collect FRFs for a number of measuring positions of the structure. Data from the measured FRFs were used in the process of detection of structural damage, so purpose of the test was to obtain a dynamic model of the structure that can be used to assess the effects of modification (damage) to that structure [2]. Modal testing was performed using the following measuring equipment, Figure 3:

- Excitation of the structures: modal hammer, Endevco
- Response of the structure: accelerometer, type 4507, Bruel&Kjaer
- Acquisition unit: Portable PULSE Type 3560, Bruel & Kjaer

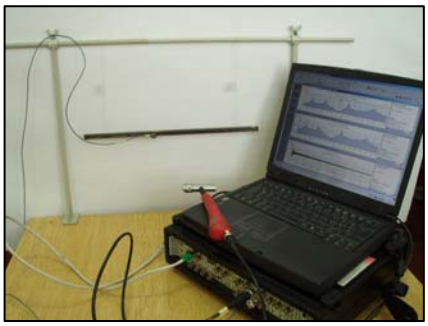

Figure 3. Measuring equipment for modal testing [2]

The steel beam of dimensions 400x15x15 mm was tested for two boundary conditions: free-free beam and cantilever beam. Testing was performed in the frequency range of 3200 Hz, with 5 averaging for each measured FRF. For the first test, the beam was suspended with the plastic string simulating free-free boundary conditions. That freely supported beam was discretized in 17 measurement degrees of freedom, Figure 4. For the second test, the beam was clamped at one end forming the cantilever beam. The cantilever beam was dicretized into 14 measurement DOFs, Figure 5. Modal testing was done using 'roving hammer" method: the accelerometer was placed in the fixed point (5th DOF for the freely supported beam and 11th DOF for the cantilever beam), the excitation was applied in all other measurement positions (17 DOFs for the freely supported beam and 14 for the cantilever beam) on the structure. In this way 17 FRFs and 14 FRFs were recorded, and verifying the quality of recorded data was performed using reciprocity and repeatability checks, coherence functions and differences function curves ΔFRF.

Figure 4. The free-free beam discretized into 17 measurment DOFs

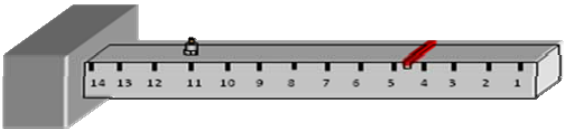

Figure 5. The cantilever beam discretized into 14 measurment DOFs

4.1 Reciprocity check

For a linear conservative system Maxwell's rule of reciprocity applies: the measured FRF for a force at location j and a response at location i should correspond directly with the measured FRF for a force at location i and response at location j. The FRF matrix is symmetric and this property can be used as a check on the quality of the measured data.

Figure 6 shows two overlie FRFs of the freely supported beam: one FRF was measured for a response at location 5 and excitation at location 12, second FRF was measured for a response at location 12 and excitation at location 5. From overlie plots of FRFs can be concluded that the functions meet the requirement of reciprocity.

Figure 7 shows two overlie FRFs of the cantilever beam: one FRF was measured for a response at location 5 and excitation at location 11, second FRF was measured for a response at location 11 and excitation at location 5. Overlie plot of FRFs indicates the functions meet the requirement of reciprocity.

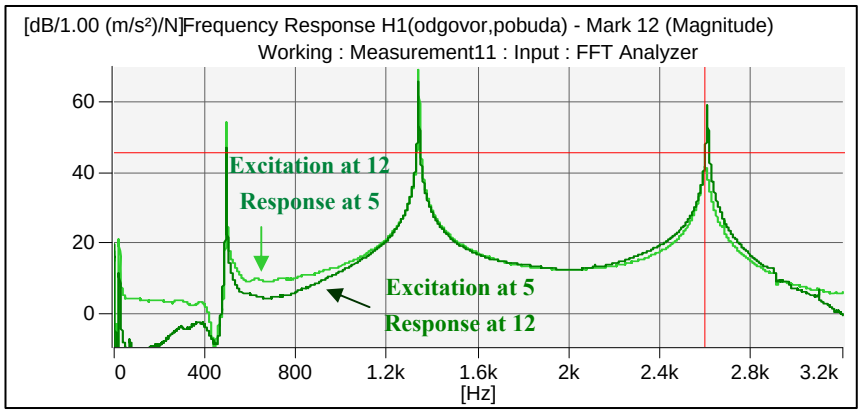

Figure 6. Reciprocity check of the freely supported beam [2]

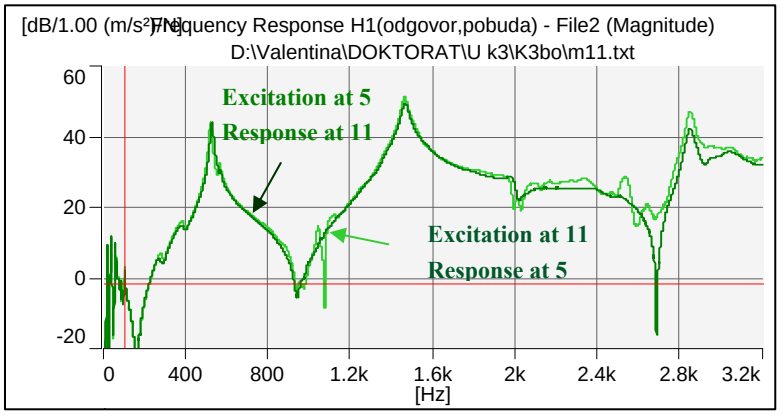

Figure 7. Reciprocity check of the cantilever beam [2]

4.2 Repeatability check

Repeatability checks are a means of assessing the stability of the structural characteristics over a period of time. It is usually assumed that the structure does not change with time or as a result of the excitation itself but there are a number of practical effects that can alter the characteristics of a structure, e.g. bolts slackening, release of pre-loads, fretting, environmental factors such as temperature and humidity, etc.
The repeatability test was done for freely supported beam by performing several measurements with the response at location 5 and the excitation at location 12, where the accelerometer was removed from the structure and re-placed on the same position, which undoubtedly caused a certain deviation of transducer location for each measurement. Overlaying of the measured FRFs confirmed the repeatability of the test, Figure 8. Overlaying FRFs measured at all 17 measurement locations, Figure 9, shows that there is no deviation of resonant peaks position, i.e. natural frequencies, showing the consistency of the measured results.

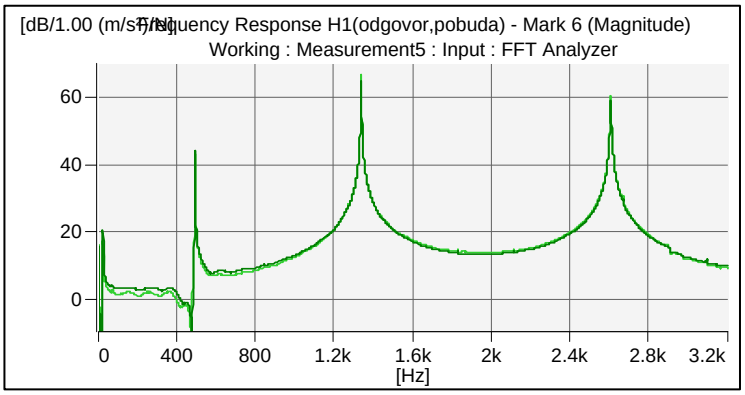

Figure 8. Repeatability check: Overlie FRFs for two measurements of response at 5 and force at 12 [2]

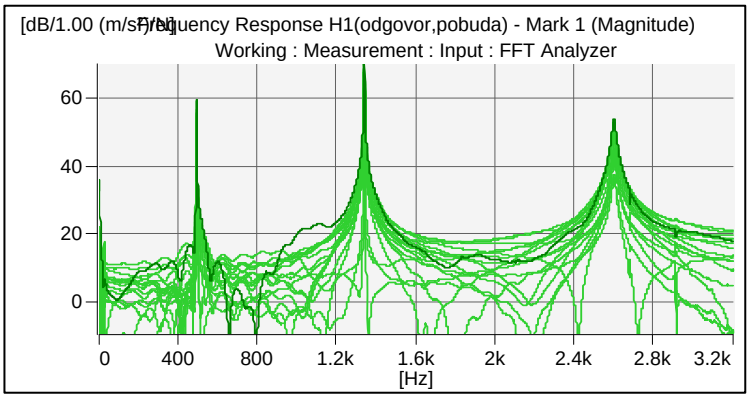

Figure 9. Consistency of results: overlie FRFs for measurements at 17 degrees of freedom [2]

4.3 Use of the ΔFRF in repeatability and reciprocity checks

Almost always reciprocity and repeatability checks are done by "eyeballing" sets of FRF curves to see if there are any major differences. The comparisons are made significantly easier if differences function curves ΔFRF are plotted for the sets of data.
The ΔFRF is the vector difference of the two FRFs at each frequency ω:

$$\Delta FRF(\omega) = FRF(\omega) \text{ for comparison} - \text{Reference } FRF(\omega)$$

Reciprocity and repeatability checks are usually carried out over a frequency range incorporating several modes, with the emphasis placed on the magnitude of the functions. The magnitude of the ΔFRFs is plotted alongside the two FRFs of the reciprocity and repeatability checks for comparison. If a large peak on the ΔFRF corresponds with a resonance region of the constituent FRFs, then it is likely that the difference is due to a slight shift in the natural frequency. When a peak occurs away from resonance, it is usually caused by differences in the magnitude of the FRFs.

The ΔFRF in repeatability checks: The two point FRF measurements, Figure 8, were made at different times as a check of measurement repeatability. The vector difference between these two functions has been calculated and forms the ΔFRF that shows clearly the large differences between the FRF measurements around the resonance region for the first and second resonancies, Figure 10a.

The ΔFRF in reciprocity checks: The use of the ΔFRF in assessing the reciprocity of measured FRFs is shown in Figure 10b. Two measured reciprocal FRFs, shown at Figure 6, are plotted together with ΔFRF. These FRFs were measured in the separate single input surveys, the excitation being moved from one input to the other for second survey, as well as the transducers position was changed. The graph in Figure 10b shows large peaks of ΔFRF in the regions of resonances. It indicates that there is a small shift in the resonance frequencies of the two constituent FRF, which is probably a consequence of local mass changes due to changes in the position of accelerometer during two measurements.

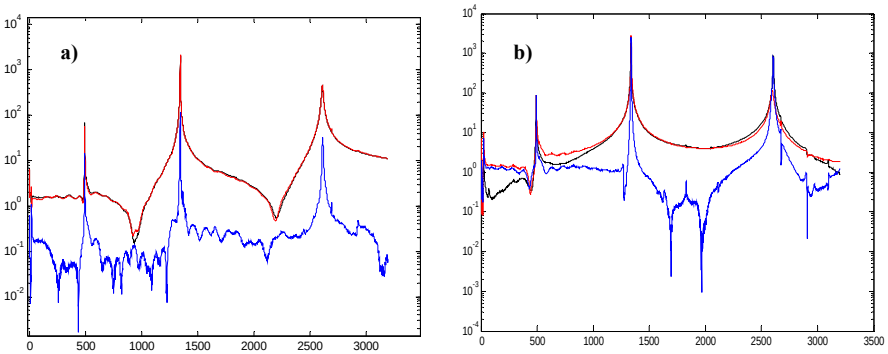

Figure 10. Use of the ΔFRF: a) repeatability check, b) reciprocity check [2]

4.4. Coherence function

An important parameter of the measurement accuracy is the coherence function. The coherence shows a correlation between the measured excitation and response signals, calculated for each frequency. In practice, the value of coherence is always greater than zero and less than unity. Good measurement is the measurement for which the value of coherence is closer to the unit. If the coherence is less than unity, it may be due to the following:

- noise is present in the excitation and response signals during FRF measurements;
- error "leakage" is present in the spectral analysis;
- the tested system is not linear;
- measured response x (t) is not only a consequence of entered excitation f (t), but also some other external reasons.

Figure 11 shows good coherence function very close to the unit value, but coherence function shown at Figure 12 indicates some the trouble due to impact excitation of structure.

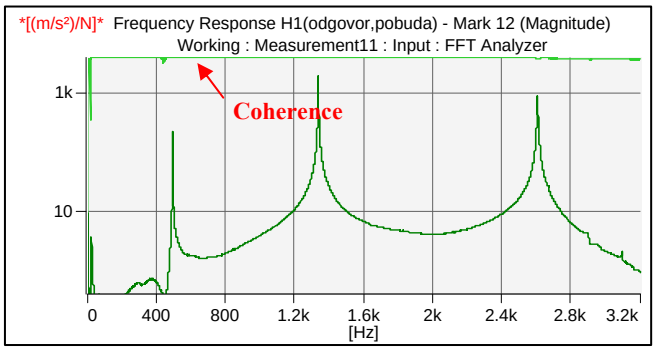

Figure 11. Coherence function of the freely supported beam [2]

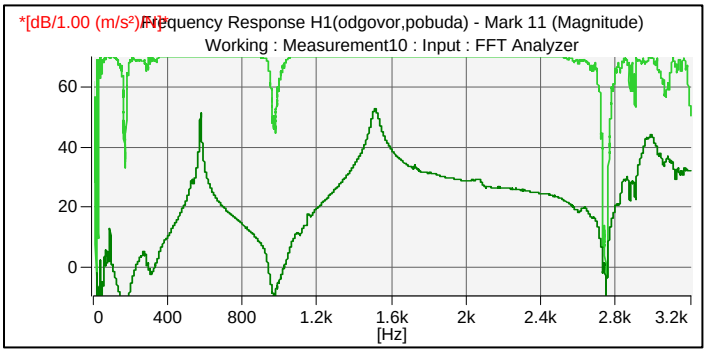

Figure 12. Coherence function of the cantilever beam [2]

5. Conclusion

There are many potential problems with modal testing which could be overcome by performing preliminary measurements. The preliminary measurement offers the opportunity to assess the influences of the test equipment on the structure, the selection of structure support, the way of excitation, etc. The accuracy of experimental data is very dependent on particular problems related to the experimental set-up and control of the different analysis steps. As a part of preliminary measurements, verifying the quality of the measured data can be made using reciprocity and repeatability checks and coherence functions. The goal of this paper was to demonstrate these methods for assessment the measurement data quality by performing modal analysis of beam like structure.

6. References

[1] Maia, Silva, He, Lieven, Lin, Skingle, To, Urgueira (1997) *Theoretical and experimental modal analysis*, Research Studies Press LTD.
[2] Golubović-Bugarski V. (2010) Models of correlation between structural damages and dynamic response of mechanical system (Modeli korelacije strukturnih oštećenja sa dinamičkim odgovorom mehaničkog sistema), PhD thesis, Faculty of mechanical Engineering, University of Banja Luka.

THE USE OF FINITE ELEMENT METHOD (FEM) FOR ANALYZING STRESS DISTRIBUTION IN ADHESIVE INLAY BRIDGES

A. Grbović[1], N. Vidanović[2], K Čolić[3], D. Jevremović[4]

[1]Faculty of Mechanical Engineering,
The University of Belgrade, Kraljice Marije 16, 11120 Belgrade
e-mail: agrbovic@mas.bg.ac.rs
[2] Faculty of Transport and Traffic Engineering,
The University of Belgrade, Vojvode Stepe 305, 11000 Belgrade
e-mail: n.vidanovic@sf.bg.ac.rs
[3] Innovation Center,
Faculty of Mechanical Engineering,
The University of Belgrade, Kraljice Marije 16, 11120 Belgrade
e-mail: kbojic@mas.bg.ac.rs
[4]Faculty of Dental Medicine,
The University of Business Academy in Novi Sad, Žarka Zrenjanina 179, 26000 Pančevo,
e-mail: dr.danimir@sbb.rs

Abstract. Adhesive inlay bridges are used in dentistry as a possible treatment modality, when a single anterior or posterior tooth is missing. In despite of their advantages, such are minimal invasiveness, simplicity and fast treatment, their main problem is retention loss, caused by reduction in bonding surface. The aim of this article is to analyzing stress distribution at restoration-tooth interface of selected preparatory design, by means of finite element analysis. The results show potential agreement with theoretical models. Finally, this model is suitable for use in everyday practice.

1. Introduction

Adhesive fixed partial dentures (AFPDs) are a part of a group of minimally invasive fixed constructions, with inlay retainers instead of classic-shell retainers. Reduced contact area, however, weakens the retention and makes these dentures prone to decementing during functioning. Decementing being a consequence of extensive stress on the cement layer, stress states of the cement layer can be observed, analysed and interpreted using FME, simulating loads affecting the denture during mastication cycles.
Adhesive fixed partial dentures (AFPDs) are a useful conservative prosthodontic treatment option and have proven their clinical reliability in combination with the metal-ceramic technique [2, 3]. When an esthetic single-tooth replacement with a minimally invasive tooth reduction is desired and an implant is refused by the patient, metal-free restorative options may be attractive. Since the bonding procedures strengthen the cusps and provide additional support for the dentition, minimally invasive preparation is feasible [4, 5, 6]. Some

developments in the application mode of dentin adhesives [7, 8, 9] have enabled the use of indirect (lab-made) bonded restorations.
Reinforced ceramics have been proposed for the fabrication of metal-free AFPDs. The brittleness of ceramics makes this project difficult [10]. In addition, high-elastic-modulus frameworks are expected to increase stress concentration at the adhesive interface, especially in the presence of long-span AFPDs [11]. One theoretical claim is that lower-elastic modulus frameworks would ensure a better stress transfer to the tooth and reduce tensile stresses at the adhesive interface [12].
Knowledge of stress distribution is important to the understanding of fatigue yielding, which generally occurs under subclinical micro-deformation. Overall stress distribution within the tooth-restoration complex is determined by geometry and hard tissue-restorative material arrangement [13]. As demonstrated by Reeh et al,[14] non-destructive approaches, rather than experimental load-to-failure, may be the best approach to determining significant differences in stress distribution.
Non-destructive approaches can provide greater insight into the performance of both tooth and restorative materials but may require complex modeling tools such as the finite element (FE) method. Experimental-numerical approaches now serve as comprehensive in vitro investigation methods for the examination of the complex mechanical behaviors of prostheses and surrounding structures. The aim of this study was to evaluate the stress distributionat the surface and interface of 3-unit posterior AFPDs with the 3-dimensional FE method. Restorative material used in this analysis was zirconia-dioxid (ZirCAD).

2. Material and methods

2.1. Description of modeled geometry

Two natural extracted teeth (a mandibular second premolar and second molar) were selected and scanned to simulate a lateral dental segment with partial edentulism (missing first molar) [16]. A space of 13 mm was left between the teeth which were prepared with interproximal slots of specific dimensions. The corresponding fixed partial denture (FPD) was fabricated and digitized with a scanning device and used as a reference to trace the detailed contours of dental hard tissues and FPD components in a graphics software program CATIA v5 (Figure 1). Next step was to import modeled geometry in Ansys13.

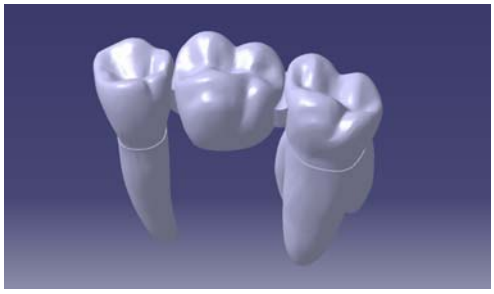

Figure 1. Catia model

Figure 2 shows geometry of the virtual model imported into Ansys13, consisting of a fixed partial denture made from ZirCAD, cemented onto two teeth, previously treated and prepared for attachment of the fixed denture.

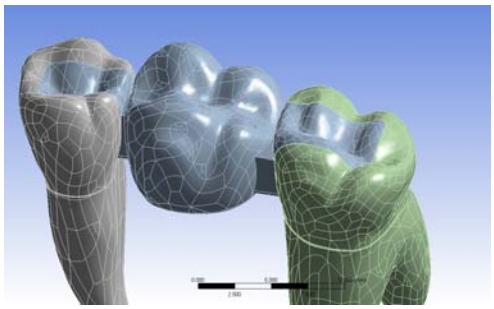

Figure 2. Modeled geometry after importing into Ansys13

The form of the fixed partial denture, and its associated finite element mesh are shown in Figures 3 and 4. The appearance of the prepared teeth with associated mesh of finite elements are shown in Figures 5 and 6. The final model was defined using 3.427.253 nodes, i.e. 2.178.305 elements.

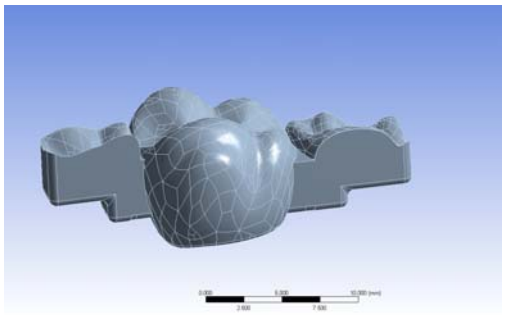

Figure 3. Geometry of the fixed partial denture attained by joining multiple segments

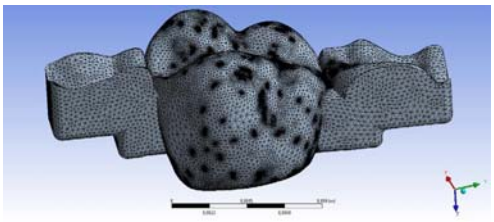

Figure 4. Finite element mesh of the fixed partial denture

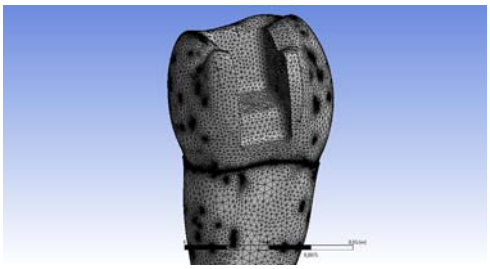

Figure 5. Finite element mesh of the premolar

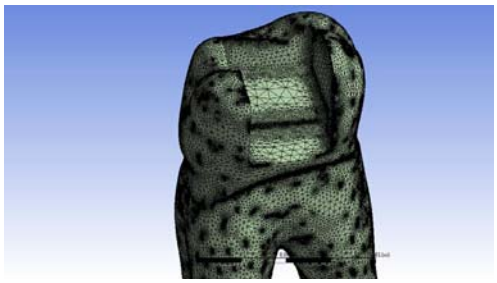

Figure 6. Finite element mesh of the second molar

2.2. Determination of the boundary conditions

To foster a systematic understanding of mechanical events, the simulation was performed in 2 steps. First, an evaluation and characterization of stress distribution with different abutment preparation configurations was undertaken. Second, the selected cofiguration was simulated to provide stress distribution in critical areas.
During defining the boundary conditions an assumption was made that the teeth were not fixed in place, and that the root (and therefore the tooth) was allowed a certain amount of vertical displacement inside the alveole, which should not amount to more than two hundredths of a millimetre (distance between the alveole and the root). Except for the allowed displacement, the tooth should behave like a fixed support, and it is adopted that the entire system is supported by virtual springs, which have the ability to simulate the behaviour previously described (Figure 7).

Table 1 shows the values of Young modulus of elasticity and Poisson coefficient used in all three cases:

Material	Young modulus of elasticity (MPa)	Poisson coefficient
Dentin	20000	0,3
ZirCAD	210	0,23

Table 1. The characteristics of the materials used in the analysis

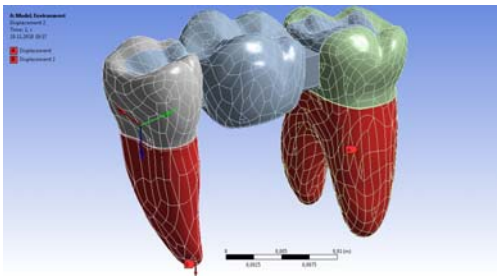

Figure 7. Allowed displacement of premolar and second molar roots (marked in red) was 2x10e-5m in the z-direction

Three-dimensional FE models derived from scanned 3-unit AFPD were subjected to a three types of loads. Loads were applied from three directions that simulated contact with the antagonistic tooth during mastication. To simulate mastication, three areas were loaded on the outer inclines of the buccal cusps. The total load was 75 N at each loading areas. The load was applied from three directions: at 90^0 to the tooth axis (horizontally) (Figure 8), at 45^0 to the tooth axis (angularly) (Figure 9) and at 0^0 to the tooth axis (vertically) (Figure 10). Namely, vertical force was replaced with pressure application (8.145MPa). The postprocessing files allowed the calculation of the equivalent von-Mises stress at the tooth-restoration interface.

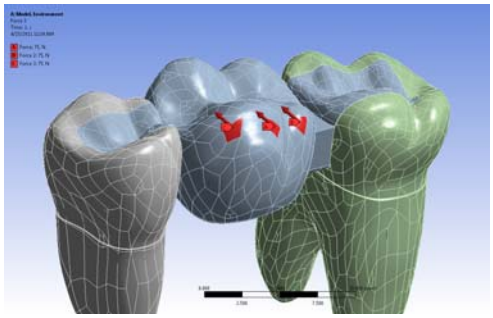

Figure 8. Directions and intensities of applied forces for the first loading case

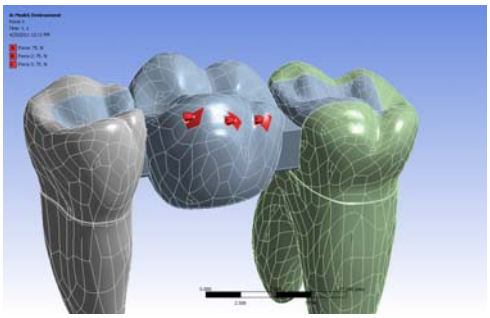

Figure 9. Directions and intensities of applied forces for the second loading case

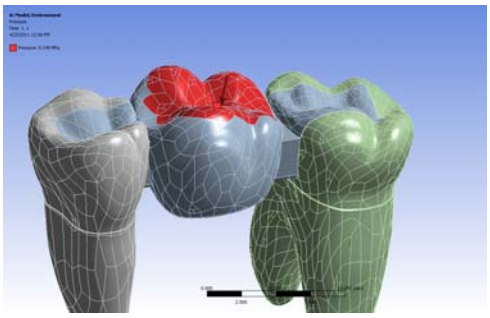

Figure 10. In the third case, a pressure of 8.145MPa was applied to the upper surface of the fixed denture on the area marked in red

3. Results

Figures 11, 12 and 13 show obtained stress state of the entire model for all three analyzed cases, whereas the maximum values of stress and deformation are given in the Table 2.

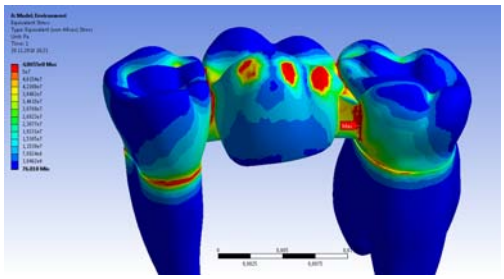

Figure 11. Three-dimensional stress distribution for the first loading case

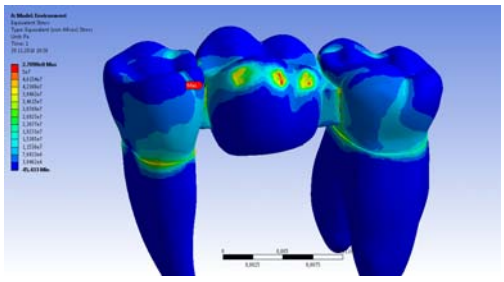

Figure 12. Three-dimensional stress distribution for the second loading case

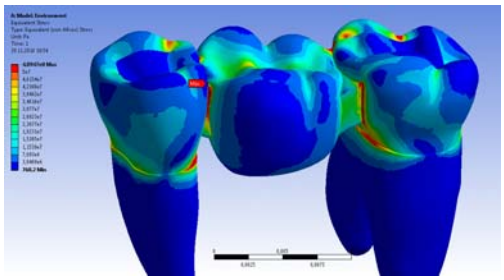

Figure 13. Three-dimensional stress distribution for the third loading case (8.145MPa pressure)

Loading case	Max model stress (Pa)	Element with maximum stress	Maximum model deformation (m)	Element with maximum def.
First	4.865×10^{8}	Second molar	1.699×10^{-3}	denture
Second	2.709×10^{8}	Premolar	0.650×10^{-3}	denture
Third	4.894×10^{8}	Premolar	0.870×10^{-3}	denture

Table 2. Maximum values of stress and deformation for all three loading cases

Figure 14, 15 and 16 show stress distributions for the most stressed elements of the system fixed denture – teeth, for external loads in all three cases.

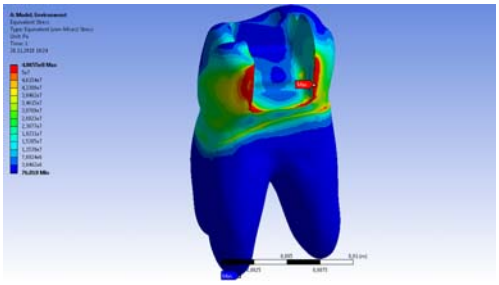

Figure 14. Three-dimensional stress distribution of the second molar for the first loading case

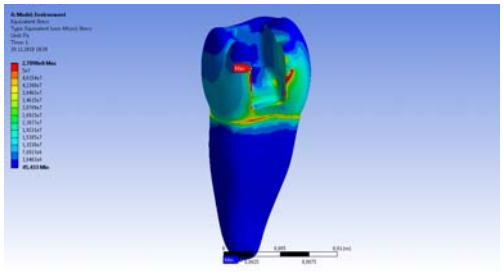

Figure 15. Three-dimensional stress distribution of the premolar for the second loading case

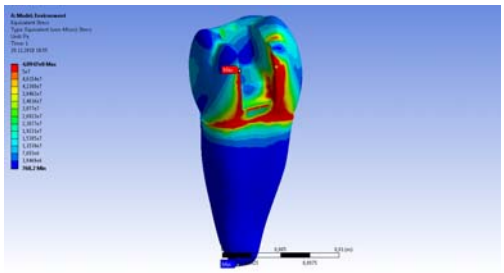

Figure 16. Three-dimensional stress distribution of the premolar for the third loading case

For the case of vertical loading, maximum stress values occur at contact points, i.e. at the connections of the beam with the supporting teeth (Figure 13). Maximum values appear at the edge area, which is prepared to be connected with the denture (Figure 16). The zone with significant stress concentration in the beam material is situated in the connector region, i.e. in the area of the transition to the retainer.
For the case of angular (inclined) loading, maximum stress values occur at contact points, for the reason of increased strength of the diagonal cross-section in comparison to the vertical loading. With angular loading, the increase in stress is carried to the root of the tooth, to the zone of the contact with the periosteum. Also, an assymetrical stress distribution on the surface of the prepared denture cavity was observed. In this case a stress concentration can also be seen at the points of contact of the bridge and supporting teeth (Figure 15). Like the previous model, maximum stress occurs in the zone of the connection of the denture with the supports (Figure 12), but the maximum value is lower in this case.
Like expected, the maximum deformation was obtained for horizontal force, followed by vertical load, while force at 45 degrees produced the smallest deformation (Table 2).

4. Discussion

By using digital scanning it is possible to obtain adequate and favourable model for finite element method analysis. Using appropriate software for processing the results of the scanning, it is possible to obtain aqurate models with reasonable expenditure of time and resources. The convergence of the models with different number of finite elements was adequate, which proved the reliability of procedure used.

References

[1] Magne P, Perakis N, Urs C Belser, Krejci I (2002) Stress distribution of inlay-anchored adhesive fixed partial dentures: A finite element analysis of the influence of restorative materials and abutment preparation design. *The Journal of Prosthetic Dentistry*, **87(5)**, pp. 516-528.
[2] Creugers NH. (1991) Resin bonded bridges. A status report for the American Journal of Dentistry. *Am J Dent*, **4**, pp. 251-5.
[3] Kerschbaum T, Haastert B, Marinello CP (1996) Risk of debonding in three-unit resin-bonded fixed partial dentures. *J Prosthet Dent*, **75**, pp. 248-53.
[4] Wendt SL Jr. (1991) Microleakage and cusp fracture resistance of heat-treated composite resin inlays. *Am J Dent*, **4**, pp. 10-4.

[5] Fissore B, Nicholls JI, Yuodelis RA (1991) Load fatigue of teeth restored by a dentin bonding agent and a posterior composite resin. *J Prosthet Dent*, **65**, pp. 80-5.
[6] Morin D, DeLong R, Douglas WH (1984) Cusp reinforcement by the acid-etch technique. *J Dent Res*, **63**, pp. 1075-8.
[7] Bertschinger C, Paul SJ, Luthy H, Scharer P (1996) Dual application of dentin bonding agents: effect on bond strength. *Am J Dent*, **9**, pp. 115-9.
[8] Paul SJ, Scharer P (1997) The dual bonding technique: a modified method to improve adhesive luting procedures. *Int J Periodontics Restorative Dent*, **17**, pp. 536-45.
[9] Magne P, Douglas WH (1999) Porcelain veneers: dentin bonding optimization and biomimetic recovery of the crown. *Int J Prosthodont*, **12**, pp. 111-21.
[10] Pospiech P, Rammelsberg P, Goldhofer G, Gernet W (1996) All ceramic resinbonded bridges. A 3-dimensional finite-element analysis study. *Eur J Oral Sci*, **104**, pp. 390-5.
[11] Philips RW. *Skinner's science of dental materials.* 9th ed. Philadelphia: WB Saunders; 1991. p. 373-5.
[12] Vallittu PK, Sevelius C (2000) Resin-bonded, glass fiber-reinforced composite fixed partial dentures: a clinical study. *J Prosthet Dent*, **84**, pp. 413-8.
[13] Magne P, Versluis A, Douglas WH (1999) Rationalization of incisor shape: experimental-numerical analysis. *J Prosthet Dent*, **81**, pp. 345-55.
[14] Reeh ES, Douglas WH, Messer HH (1989) Stiffness of endodontically-treated teeth related to restoration technique. *J Dent Res*, **68**, pp.1540-4.
[15] Grbović A, Tanasković M, Vidanović N, (2009) Comparative analysis of stress distribution on the toothless alveolar ridge at the bottom of the complete denture prosthesis and overdenture retained with mini implants, *2nd International Congress of Serbian Society of Mechanics*, D-14.
[16] Jevremović D (2008) Distribucija i koncentracija napona u adhezivnim mostovima, *Doctoral Thesis*, Belgrade.

THE USE OF FINITE ELEMENT METHOD (FEM) FOR SIMULATING CRACK GROWTH IN MINI DENTAL IMPLANTS (MDI)

A. Grbović[1], N. Vidanović[2], G. Kastratović[3]

[1]Faculty of Mechanical Engineering,
The University of Belgrade, Kraljice Marije 16, 11120 Belgrade
e-mail: agrbovic@mas.bg.ac.rs
[2] Faculty of Transport and Traffic Engineering,
The University of Belgrade, Vojvode Stepe 305, 11000 Belgrade
e-mail: n.vidanovic@sf.bg.ac.rs
[3] Faculty of Transport and Traffic Engineering,
The University of Belgrade, ul. Vojvode Stepe 305 11000 Belgrade
e-mail: g.kastratovic@sf.bg.ac.rs

Abstract. Developments in mini dental implants (MDI) manufacturing are aimed at making them more biocompatible and, at the same time, lighter, more durable and simultaneously safer than the existing implants. But, occasionally, during build-in process failure of MDI may occur or cracks may appear which could lead to the latter fatigue failure of MDI. In order to understand and assess crack growth in MDI, several different Finite Element (FE) tools capable of performing crack growth analyses on three dimensional models have been analyzed and the commercial tools Ansys13 and FRANC3D v5 have been selected. Using FRANC3D software different crack sizes and shapes have been made on 3D model of MDI and simulations of crack growth have been performed. Based on simulation results a more developed damage criterion is proposed and some hints on the mini dental modeling process are recapitulated.

1. Introduction

In recent years, both the literature and clinical practice showed more interest in finding new ways of treating and taking care of edentulous patients. Due to specificity of the lower muco-osseous foundation, construction of the lower complete denture is such a prosthetic problem, and in most cases represents a challenge for the therapist. During growth and development, teeth of the permanent dentition are in mandibular and maxillary alveolar extensions.

Soon after tooth extraction, the alveolar ridge remains on the spot and being resorpted eventually, changes into residual alveolar ridge. Residual alveolar ridge (RAR) with surrounding tissues makes the support of the mobile replacement. Numbers of researchers [1], [7] agree that in terms of the intensity and direction of reduction process, the alveolar ridge of the lower jaw has more unfavorable course than the upper alveolar ridge.

Implantology has improved the therapy of edentulous patients within the range of poor to much expressed RAR resorption. The oral rehabilitation, which uses two to four implants in supporting complete prosthesis, has been proved rather successful in 96% cases with one or

two-phase built-in implants. Many authors have published that patients were pleased with lower complete implant supported dentures.

The atrophy of a edentulous jaw could limit the possibility of building in implants, especially in the lower jaw area. The anatomic limit as well as alveolar ridge resorption may compromise the number of implants, their length and position. Using standard diameter implants as a support of a complete denture often requires the ridge extension in order to obtain sufficient bone size. In case of older patients with serious medical illness or those who use anticoagulant therapy, the procedure of building in more than one standard implants raises the risk of surgical complications. Narrow-diameter titanium implants (2TA11 Titanium, Young's Modulus 1.171e11Pa, Poisson's coefficient 0.3), which are implanted without lifting the chop so that they could support conventional existing denture, represent the rehabilitation method for patients suffering from mandibular atrophy.

Small-diameter dental implants have been used in different shapes for the last twenty years. Those implants have the diameter of 2.75 to 3.30mm, and they are placed on a jaw with a reduced bone volume. Mini dental implants (MDI) are even smaller- with the diameter of 1.8 to 2.4mm [8], [9]. The advantage to MDI (Figure 1) usage is minimally invasive building in procedure which is completed in one visit [10]. Comparing to MDI, the building in procedure of conventional implants (of diameters 3.5mm and more), is aggressive surgical procedure which requires a surgery cut of gingiva, lifting the chop and osteotomia-bone preparation as it relates to existing implants. Such procedure requires healing time process of a tissue, in other words its regeneration, establishing vascular function and osseointegration of the implant itself.

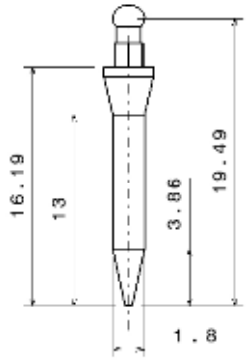

Figure 1. Mini dental implant

Minimally invasive MDI building in technique is consisted of screwing the implant into the bone through the initial opening (Figure 3), without complete preparation of the lies in the implant bone [10]. This is why there were no signs of a damaged bone, neither the areas of bone injury during the implantation. But, occasionally, during build-in process failure of MDI may occur or very small cracks may appear which could lead, after some time, to fatigue failure of MDI. In order to investigate this phenomenon FE model of MDI's crack growth has been developed and analyzed. For that purpose virtual geometry in Figure 2 has been used. Results of this investigation are presented in this paper.

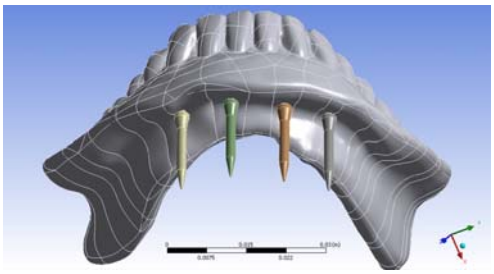

Figure 2. Total denture supported by four MDIs (Virtual model)

Figure 3. Real model of built-in MDIs used to define numerical model

Figure 4. Total denture supported by MDIs

2. Finite element model and analysis

In order to understand and assess crack growth in MDI, several different Finite Element (FE) tools, capable of performing crack growth analyses on three dimensional models, have been analyzed and the commercial tools Ansys13 and FRANC3D v5 have been selected.

Results published by the same authors in 2009 [21] have been used in order to define boundary conditions for crack growth analysis.

Figure 5. MDI before build-in

Figure 6. Broken MDI (during build-in)

2.1. Determination of the magnitude and direction of load input

During build-in of MDI there is a possibility of implant failure due to large torsional moment (Figure 6) or micro cracks may appear which can cause fatigue failure in cyclic stress environment. In order to simulate fatigue crack growth in damaged MDI, it is necessary to define realistic dynamic loads.
There is a detailed data in literature [13, 16] on the determination of the magnitude and direction of the mastication force and for the edentulous patients force magnitude varies from 50N to 210N. Since many authors take the average value of 100N, in this study horizontal and vertical forces of magnitudes 0.005 had been applied on MDI during different time intervals (Figures 8 and Figure 9) and later these values were multiplied by cyclic load amplitude of 20000N in order to get maximum predicted value of 100N. It must be emphasized that load on MDI, caused by mastication force acting on the denture, is much less than 100N and varies over time. In order to simulate these variations, random load spectrum has been generated (Figure 7) with mean value of 5N, standard deviation of 11.32N, maximum value of 100N and period of 94s.

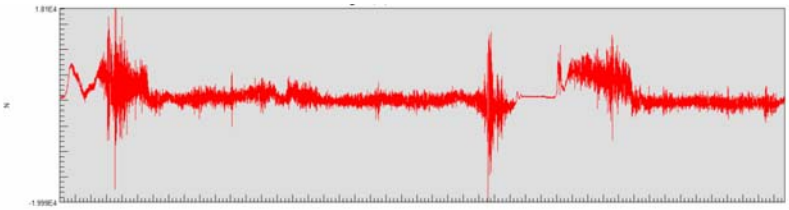

Figure 7. Load spectrum used for crack growth analysis

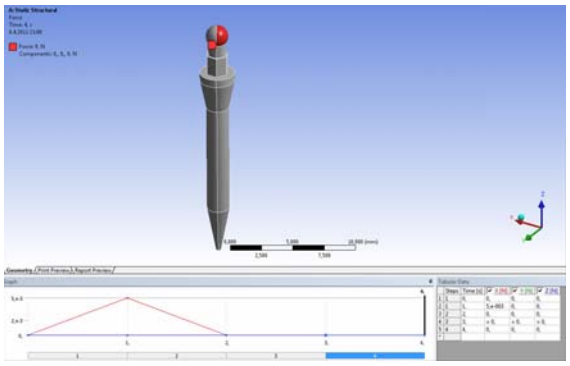

Figure 8. Horizontal component of load acting on MDI during first two seconds

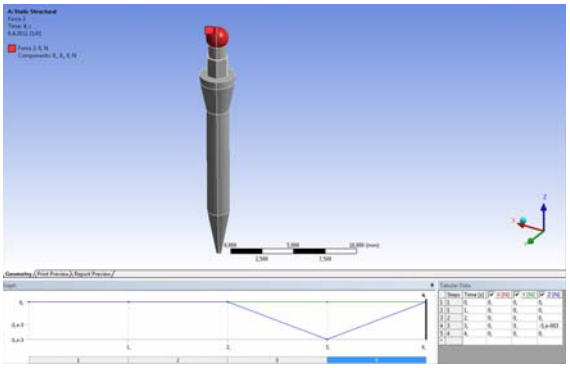

Figure 9. Vertical component of load acting on MDI during next two seconds

2.2. Stress analysis results and identification of the critical MDI area

After the loads had been applied, FE analysis has been performed and results are presented in Figure 10 and Figure 11. It can be seen that stress values are very low (0.0459MPa and 0.00639MPa, respectively). This is due to the fact that small loads (0.005N) have been applied on MDI. But, during the second phase of the simulation these small loads have been multiplied by load spectrum in order to get more realistic dynamic loads. The main idea was to identify critical area of MDI in terms of fatigue crack appearance and to calculate number of cycles which will initiate crack growth. In Figure 12 critical area is clearly labeled and number of cycles of load spectrum which would initiate crack growth was found to be between 533 and 20000. This means that total time before crack would start to grow due to cyclic load environment is between 14 hours (worst case) and 500 hours (optimal case).

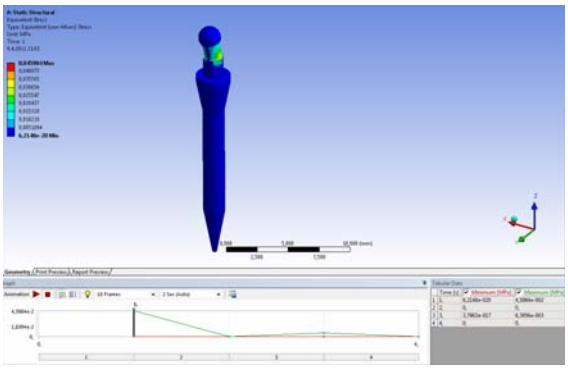

Figure 10. Stress distribution in MDI due to horizontal load component

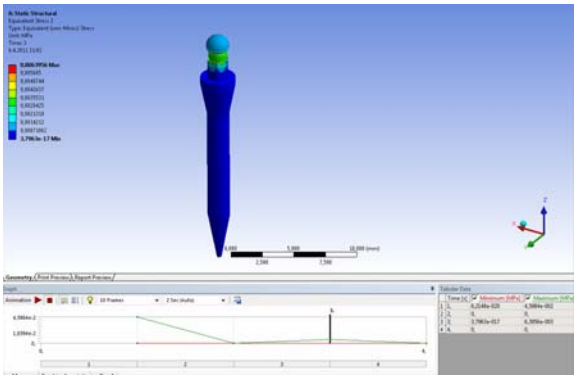

Figure 11. Stress distribution in MDI due to vertical load component

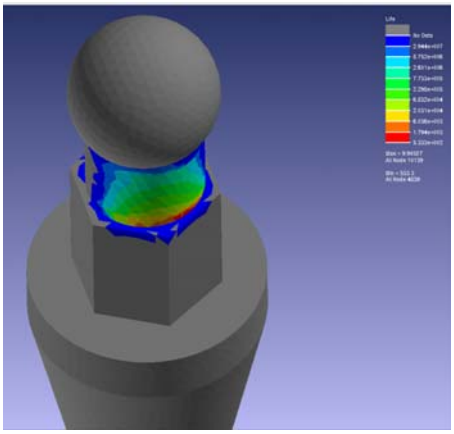

Figure 12. MDI's critical area in terms of fatigue crack appearance

2.3. Simulation of fatigue crack growth in Ansys13 and FRANC3d software

First step in setting the crack growth properties was to define initial crack length. Value of 0.05mm was chosen (Figure 13).

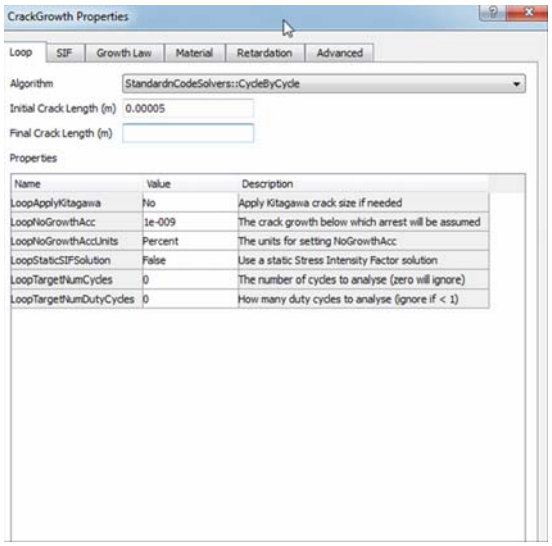

Figure 13. Crack Growth Properties setup (Initial Crack Length)

Second step was to define crack geometry. In our case, it is assumed that the crack in the implant is much like a semi-circular crack in tension (Figure 14).

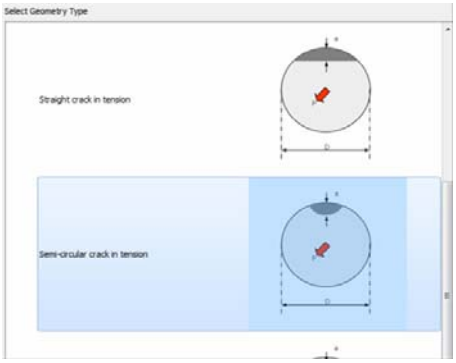

Figure 14. MDI's semi-circular crack in tension

Once the model is created in Ansys, the FRANC3D steps necessary to perform crack growth analysis are: read the mesh information, rebuild the mesh around the crack, perform

the Ansys analysis and compute stress intensity factors. The program begins the process of inserting the flaw into the original model and then meshes the resulting cracked model (Figure 15).

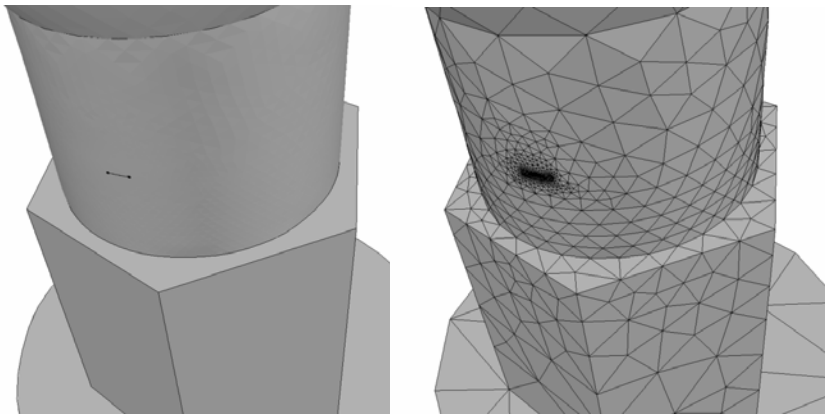

(a) (b)

Figure 15. MDI model with initial crack length 0.05mm (a) and FE mesh (b)

In Figure 16 interior view of generated crack in MDI is given.

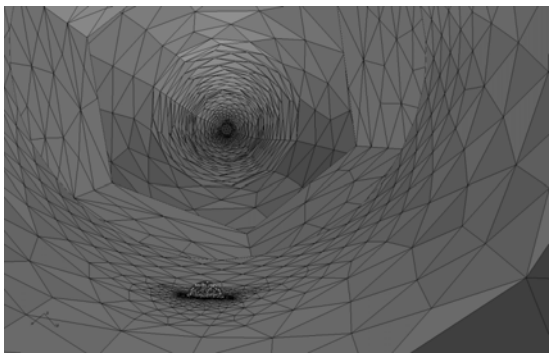

Figure 16. Interior view of generated crack and finite element mesh

The default crack extension criterion used for simulation was Specified Median Extension. The relative extension at each point along the crack front was computed based on the chosen equation and a user-specified median extension. The median extension occurs at the point along the crack front with the median Mode I SIF value. To simulate crack growth a Paris-like power law was used. Power law equation for determining relative extension is shown here:

$$\Delta a_{node\ i} = \Delta a_{mean}\left(\frac{\Delta K_{node\ i}}{\Delta K_{mean}}\right)^{n}$$

The next figures display the computed crack front in the model after five steps of calculation. After each step the extension was scaled, polynomial was adjusted to fit through the new crack front points, and the polynomial extrapolation was adjusted to ensure intersection with the model surface.

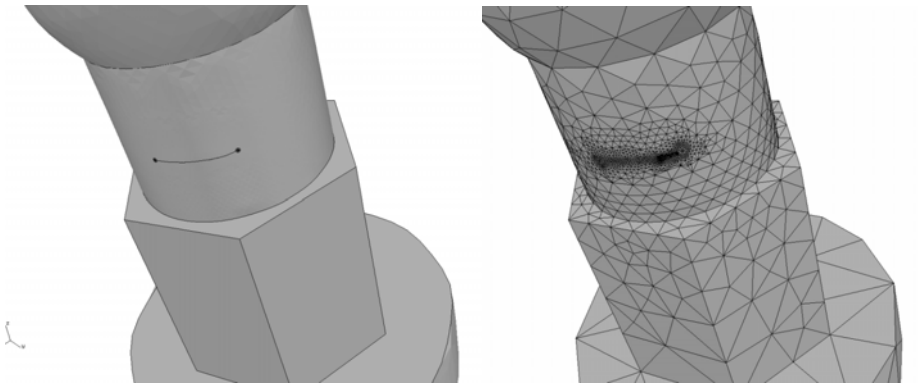

Figure 17. The computed crack shape in MDI after five steps of calculation

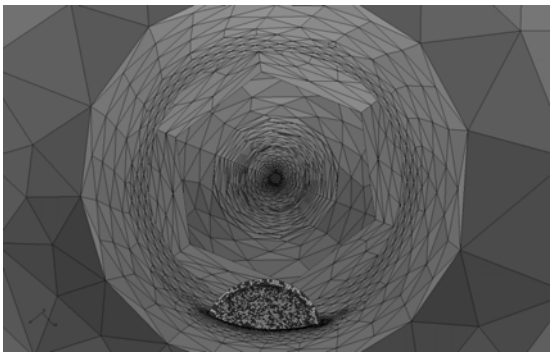

Figure 18. Interior view of crack front in the model after five steps of calculation

Crack growth can slow or even stop under certain loading conditions. This effect can be assessed using crack retardation models. Here standard retardation algorithm was used. At the same time a number of cycles which can lead to critical crack length was calculated in Ansys. Plot in Figure 19 shows crack length versus cycle number, as shown below. It must be noticed that the initial crack length was 0.05mm as we inputted earlier. The final crack length is just over 1mm at about 500000 cycles. This is why the calculation in FRANC3D

continued until the crack reached length of 1mm. It turned out to be after tenth step of calculation.

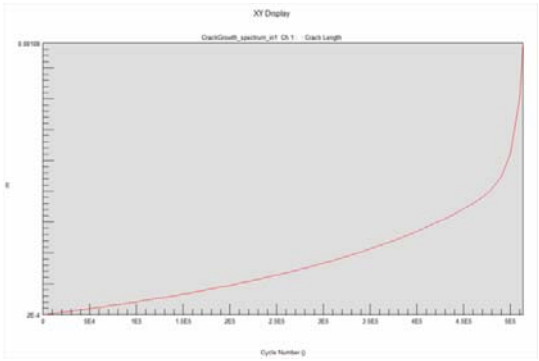

Figure 21. Crack length versus cycle number

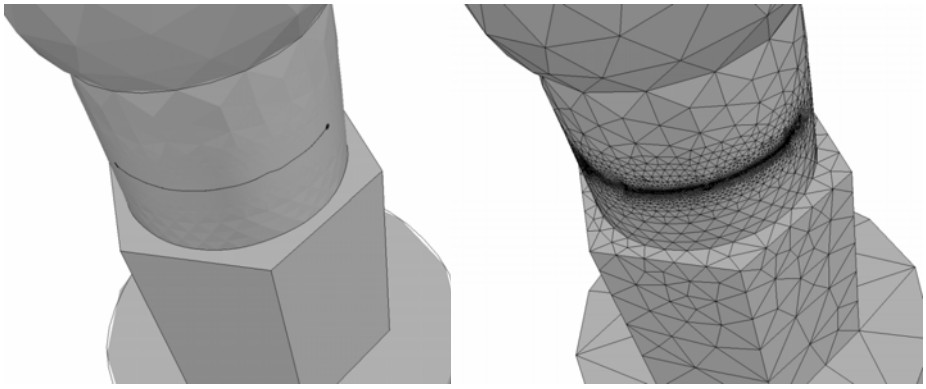

Figure 19. The computed crack shape in MDI after ten steps of calculation

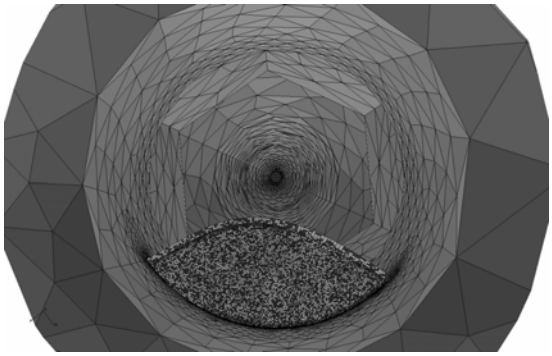

Figure 20. Interior view of crack front in the model after ten steps of calculation

3. Discussion

The objective of the analysis that was carried out in this paper was to establish and to accept the methodology of investigation of fatigue phenomena, which are, in the most cases, the main reason of the failure of the supporting structures. As the supporting MDI elements are of vital importance for the toothless patients, and as the analysis of the fatigue phenomena is usually very difficult, the FEM analysis of the crack growth and the determination of the number of cycles which will lead to fatigue crack failure, must be employed in order to obtain better solutions.
The vast number of software has the ability of determination of the critical areas in terms of fatigue crack appearance, but only FRANC3D has the capability of crack growth simulation through solid, i.e. 3D crack growth simulation, as well, and that was demonstrated in this paper. However, the FRANC3D uses Ansys solver for the model stress and strain state analysis, so it cannot be used independently. Furthermore, it cannot be used for geometry modeling, and the geometry of model must be imported from other software. Regardless of these limitations, it has been shown that FRANC3D has excellent algorithms for automatic and/or user defined crack growth simulation.

4. Conclusions

1. The main goal of this paper was to show that it is possible to simulate complex phenomena such as fatigue crack failure and micro crack growth in small supporting structures, such as MDI.

2. It is well known, from the clinical practice, that the MDI are very reliable, and that the crack failure at MDI rarely occurs during the exploitation. However, the crack failure at MDI often occurs during the built-in process. So, it is presumed that micro cracks in MDI can also occur during that process. In that sense, critical area of the initial crack, that could grow in the future, was identified. The initial crack length was set to be just 0.05mm.

3. After the crack was initiated, the number of cycles of randomly generated load spectrum of horizontal and vertical forces required to initiate crack growth was determined. It has been shown that those cycles number, when expressed in hours, vary between 14 and 500 hours of exploitation, depending on where the crack would appear.

4. Further calculation showed that the critical crack length that will lead to fatigue failure of MDI is slightly greater than 1 mm. It also showed that more than 500000 cycles were required for fatigue crack failure of MDI. This result confirmed the expectations that even the damaged implant will perform its function for a long period of time. This also concurs with clinical practice experiences, which shows that the fatigue crack failure at MDI rarely occurs during the exploitation.

5. Given that, during the calculations, the worst load case scenarios were applied (load spectrum was very abrupt and rather long), it can be concluded that the minimal designed life of slightly damaged MDI of 520000 cycles is absolutely acceptable, considering the fact that it is used mostly by elderly patients.

6. Finally, this study is basis for further analyses which should include the variation of MDI geometry, i.e. further diminish of its dimensions. This will enable the built-in of MDI in significantly reabsorbed RARs, which is impossible today.

7. References

[1] Awad M.A., Locker D., Korner-Bitensky N., Feine J.S.: Measuring the effect of intra-oral implant rehabilitation on health-related quality of life in a randomized controlled clinical trial. *Journal of dental research* 2000; 79(9): 1659-63.
[2] M.A., Lund J.P., Shapiro S.H., Locker D., Klemetti E.: Oral health status and treatment satisfaction with mandibular implant overdentures and conventional dentures: a randomized clinical trial in a senior population.*The Int.J. of Prosthodontics* 2003;16(4):390-6.
[3] .M., Lund J.P., Chehade A., Feine J.S.: Patient satisfaction with mandibular implant overdentures and conventional dentures 6 months after delivery. *The Int.J. of prosthodontics* 2003;16(5):467-73.
[4] Knezovic-Ziataric D., Celebic A.: Mandibular bone mineral density changes in complete and removable partial denture wearers: a 6-month follow-up study. *The International Journal of Prosthodontics* 2003; 16(6): 661-5.
[5] Krstić M. i sar.: *Stomatološka protetika-totalna proteza*. "Dečije novine" Beograd, 1991.
[6] Suvin M.: *Stomatološka protetika-Biološki temelji totalne ptoteze*. 4 dopunjeno izdanje, Školska knjiga, Zagreb, 1976.
[7] Tallgren, A.: The continuing reduction of the residual alveolar ridges in complete denture wearers: a mixedlongitudinal study covering 25 years. *The Journal of prosthetic dentistry* 1972;27(2):120-132.
[8] Shatkin TE, Shatkin S., Oppenheimer AJ.: Mini dental implants for the general dentists:A novel technical aproach for small-diameter implant placement. *Compend Contin Educ Dent*.2003;24(1):26-34.
[9] Shatkin TE., Shatkin S., Oppenheimer BD., OppenheimerAJ.: Mini dental implants for long-term fixed and removable prosthetics :a retrospective analysis of 2514 implants, placed over a five-year period. *Compend Contin Educ Dent*.2007;28(2):92-9.
[10] Gibney J.W.: Minimally invasive implant surgery. *J Oral Implantol*. 2001;27(2):73-6.
[11] Griffitts T.M., Collins C.P., Collins P.C.: Mini dental implants:an adjunct for retention, stability, and comfort for the edentulous patient. *Oral Surg Oral Med Oral Pathol Oral Radiol Endod*. 2005;100(5):e81-4.
[12] Balkin B.E., Steflik D.E., Naval F.: Mini-dental implant insertion with the auto-advance technique for ongoing applications. *J.Oral Implantol*. 2001;27(1):32-7.
[13] Zarb G.A., Schmitt A.: Osseointegration for elderly patients: The Toronto study. *J.Prosthet.Dent*. 1994;72:559-568.
[14] J., Husnjak M., Guljas K., Kraljevic K.&Zivko-Babic J.: The stimulation and calculation of fatigue of the lower complete denture in function by means of the finite element analysis. *J.of Oral Rehab*.,1988;25:560-565.
[15] D.A., Coy W.A.: Clinical, cephalometric, and densitometric study of reduction of residual ridges. *The Journal of prosthetic dentistry*1971;26(3): 280-295.
[16] Tallgren, A.: The continuing reduction of the residual alveolar ridges in complete denture wearers: a mixedlongitudinal study covering 25 years. *The Journal of prosthetic dentistry* 1972;27(2):120-132.
[17] Takayama Y.,Yamada T.,Araki O.,Seki T & Kawasaki T.: The dynamic behaviour of a lower complete during unilateral loads:analysis using the finite element method. *J.of Oral Rehabil*.,2001;28:1064-1074.
[18] Assuncao W.G., Tabata L.F., Barao V.A.R., Rocha E.P.: Comparison of stress distribution between complete denture and implant-retained overdenture-2D FEA. *Journal of Oral Rehabilitation* 2008;35: 766-774.
[19] Himova L., Dostalova T., Kacovsky A., Konvickova S.: Influence of implant length and diameter on stress distribution:A finite element analysis. *The Journal of Prosthetic Dentistry* 2004;91:20-25.
[20] Meijer H.J., Starmans F.J., Bosman F., Steen W.H.: A comparison of three finite element models of an edentulous mandible provided with implants**.** *Journal of Oral Rehabilitation* 1993;20(2):147-57.
[21] Grbović A., Tanasković M., Vidanović N., Comparative analysis of stress distribution on the toothless alveolar ridge at the bottom of the complete denture prosthesis and overdenture retained with mini implants, *2nd International Congress of Serbian Society of Mechanics*, (2009), D-14.
[22] Prieto L. L., Modelling and analysis of crack turning on aeronautical structures, *Doctoral Thesis*, (2007), Barcelona.
[23] Kastratović G., Određivanje faktora inteziteta napona nosećih vazduhoplovnih struktura sa višestrukim prskotinama, *Doctoral Thesis*, (2006), Belgrade.

NOISE INDUCED COHERENT OSCILATIONS IN FITZ HUGH-NAGUMO EXCITABLE SYSTEMS INFLUENCED BY COUPLING DELAY

I. Grozdanović

[1] Faculty of Mining and geology, Department of Applied Mathematics,
The University of Belgrade, Đušina 7, 11000 Belgrade
e-mail: ines@rgf.bg.ac.rs

Abstract. Influence of small time-delays in coupling between noisy FitzHugh-Nagumo excitable systems on the coherence resonance is studied. It is shown that small time-delays can have profound effect on the noise induced coherent oscillations.

1. Introduction

Excitability is a common property of many physical and biological systems. Although there is no unique definition [1] the intuitive meaning is clear: A small perturbation from the single stable stationary state can result in a large and long lasting excursion away from the stationary state before the system is returned back asymptotically to equilibrium, further more, as an external parameter is changed, the global attractor in the form of the stationary point bifurcates into a stable periodic orbit, and the excitability is replaced by the oscillatory dynamics.

Typical example of excitable behavior is provided by the dynamics of neurons. However, realistic models of coupled neurons must include the following two phenomena: (a) influence of different types of noise and (b) different time scales of the creation of impulses on one hand and their transmission between neurons on the other. It is well known that neurons *in vivo* function under influences of many sources of noise [2]. It is also well known that the noise of an appropriate small intensity can change the systems dynamics by turning the quiescent state of the neuron into the state of periodic firing [3]. There are different types of noise induced coherent oscillations that could occur in examples of excitable systems [4], as will be discussed later. Description of interactions between neurons should include the details of the electrochemical processes in real synapses which occur on much slower time scale then the occurrence of an impulse and its transport along axons [5]. Alternatively, the transport of information between neurons can be phenomenological described by the time-delayed inter-neuronal interaction. It is well known that, depending on the parameters the time-delay can, but need not, induce drastic qualitative changes on the evolution of coupled deterministic excitable systems (please see for example [6,7,8,9,10]). However, a system of delay-differential equations is infinite dimensional with initial states represented by a vector functions on the interval $(-\tau,0)$. Stability of stochastic delay-differential equations has been studied by mathematicians [11, 12]. Influence of noise on time-delay induced bifurcations and properties of

synchronization have been analyzed elsewhere, for example in [13, 14, and 15]. On the other hand the influence of coupling delay on different types of coherent oscillations that have been induced solely by the noise has, to the best of our knowledge, not been studied. Such analyzes would supply information complementary to the research on the effects of noise on the properties of oscillations and synchrony introduced by sufficient time-lag in the delayed coupling. It is our goal in this paper to study the effects of time-delay in the coupling between two excitable units on noise induced coherent oscillations in each of the units.

The structure of the paper is as follows. In the next section we present the model of two FitzHugh-Nagumo excitable systems wit noise perturbations and coupled by delayed electrical synapses. We restrict the parameter values to such domain that the deterministic system has the stable stationary state as the only attractor for any value of the time-delay. Both units are perturbed by noise in they second equations which can induce special type of coherent oscillations. In section 3 we present and discuss the results of our numerical computations. We have analyzed effects of small time delay on coherence in the case that both units display the same type of noise induced coherent oscillations. We study the effects of time-delay on coherence properties of both single units and coincidence of spiking between units. Finally, in section 4, we summarize our results.

2. The model

Excitable behavior of a single neuron could be of two qualitatively different types [1]. They are distinguished phenomenologicaly by different properties of the frequencies and the amplitudes of the oscillatory dynamics in each of the two types, and the corresponding qualitative mathematical models are characterized by different bifurcation mechanisms. In this paper we shall consider typical type II excitable systems, as modeled by the FitzHugh-Nagumo differential equation [1], where the excitable behavior bifurcates into the oscillatory regime via the Hopf bifurcation. Each of the excitable neurons in the model is subjected to white noise that could appear in the model equations in two qualitatively different ways. Thus each neuron is described by the following stochastic differential equations:

$$\begin{aligned} \varepsilon dx &= f(x,y) = (-x^3/3 + x - y)dt + \sqrt{\varepsilon}\sqrt{2D_1}\,dW_1 \\ dy &= g(x,y) = (x + a)dt + \sqrt{2D_2}\,dW_2, \end{aligned} \qquad (1)$$

where $dW_{x,y}$ are independent increment of normalized Winer processes, that is $E(dw_i) = 0,\ \ E(dW_i dW_j) = \delta_{ij},\ \ i, j = 1,2$ and $E(...)$ denotes expectation with respect to the stochastic process. The small parameter ε, which is in our paper fixed as $\varepsilon = 10^{-2}$, takes care of the different time scales in the dynamics of the excitatory variable x (membrane potential) and the recovery variable y. The parameter a is bifurcation parameter. For $|a| > 1$ the deterministic system (1) is excitable and for $|a| < 1$ the stationary state is unstable and there exist a stable limit cycle. In this paper a is fixed to

$a = 1.05$. The two noise terms can produces series of spikes in the x variable which for certain values of the parameters D_1 or D_2 occur regularly so that the dynamics appears simply periodic i.e. coherent with quite well defined frequency. However the coherent oscillations induced by $D_1 = 0,\ D_2 \neq 0$ are qualitatively different from those that occur due to $D_1 \neq 0,\ D_2 = 0$. The first case: $D_1 = 0,\ D_2 \neq 0$ has been extensively studied, since it was reported in [16]. The effect is traditionally called coherence resonance [3], but we shall use the term stochastic coherence (SC) [17] in order to emphasize the noisy origin of the coherent oscillations. SC occurs only when the parameter a is close to its bifurcation value, the properties of ensuing oscillation resemble the Hopf limit cycle of the deterministic system, and the properties of SC follow from this fact. The oscillations in the other case $D_1 \neq 0,\ D_2 = 0$ are induced by quite different mechanism from that of the SC, it has been studied in details for example in [4], where it has been called self-induced stochastic resonance (SISR), but this will not be subject in this paper.

We shall study a pair of excitable FHN neurons (1) coupled by the electrical synapses. This type of synapse is modeled by delayed diffusive coupling between the membrane potentials of the coupled neurons. The model equations are as follows:

$$\begin{aligned} \varepsilon dx_i &= f(x_i, y_i) + c(x_j(t-\tau) - x_i)dt \\ dy_i &= g(x_i, y_i), \end{aligned} \qquad i.j = 1,2 \tag{2}$$

where $f(x_i, y_i)$ and $g(x_i, y_i)$ are given by (1). The coupling constant c in this paper always assumes positive values, which ensures that the system (2) with $a = 1.05$ and for $D_1,\ D_2$ all equal to zero, has the stable stationary state as the only attractor *for any value of the time-lag* τ. Thus possible oscillatory behavior of (2) can occur only because of the noise, and not because of strong coupling or time-delay. However, as we shall see, once the noise has produced spike trains that look coherent, quite small time delay for sufficiently strong coupling can induce important qualitative changes in the SC as well as in the properties of synchronization between the two units.

3. Numerical results

Each of the isolated noisy FHN neurons can display a train of spikes due to the noise even when the only attractor of the deterministic case is the stable stationary solution. Time distribution of the spikes can be regular with almost constant inter-spike interval. Occurrence of coherent series of spikes for particular values of the noise intensity is the common manifestation of SC. However, the two cases occur via quite different mechanisms and have different properties, like dependence of the inter-spike period and on the noise intensity. Mechanisms of SC and SISR, and their properties, have been compared in [4]. Coupling between the neurons which are in the state of SC or SISR could preserve the coherence of each of the units and furthermore lead to synchronization of noise induced oscillations. This effects have been studied in case of equal units, and in [17] for the case of

one unit in the state of SC and the other in state of SISR. In this section we illustrate the main effects of the time-delay in the coupling on the properties for both units in the SC state.

The coherence of noise induced series of spikes in each of the neurons is commonly characterized by a kind of signal to noise ration defined by:

$$SISR = \frac{\overline{T}_k}{\left[Var(T_k)\right]^{1/2}} \tag{3}$$

Where $T_k = t_k - t_{k-1}$ is the k-th inter-spike time interval and the over line, like $\overline{T_k}$, denotes time averaging. Large $SISR$ corresponds to high coherence of the noise induced spike trains.

The are different types of synchronization between the two coherently spiking neurons that could be of interest. For example, the strongest kind is the exact synchronization, i.e. $x_1(t) = x_2(t)$ for all $t > t_0$, and another commonly studied is the synchronization between phases of the two oscillators. We shall analyze the kind of synchronization such that each spike of one of the neurons occurs within the duration of some spike of the other neuron. This notion of synchrony is motivated by neurological considerations [19], and is quantified by the so called coincidence function (CF). This is defined as the time average of the ratio between the numbers of spikes of one the neurons, which are coincident with some of spikes of the other neuron, the average number of spikes per neuron. Two spikes are considered coincident whenever the sum of $x_1(t) + x_2(t)$ is larger then some threshold, say the high of spikes $\max\{x_i\}$. This type of synchrony does not assume coherent spiking and is weaker then either exact or phase synchronization.
In our numerical integration we have used Runge-Kuta 4-th order routine for the deterministic part of (2) and the Euler methods for the stochastic part. Many sample paths for each values of the variable parameters $D_{1,2}$ and τ have been calculated. Values of $SISR$ and C that are presented in what follows represent values that have been obtained with single typical sample paths.

Results of our numerical calculations are illustrated in figures 1, and 2 where fig.1 corresponds to two SC with $\tau < 1$ and fig.2 corresponds to $\tau \geq 1$. We fix the noise intensity of one of the neurons (second in our case), D_2 to the maximal coherence of SC type (fig.1 and fig.2) and study the dependence of firing coherence of both neurons and coincidence on the noise intensity D_2 of the adjustable unit and on the time-lag τ. We consider only relatively small time-lags up to the refractory period of a single spike of an isolated excitable FHN neuron, which is about $\tau \leq 1.3$. Coherence of noise induced spiking is not qualitatively affected by weak coupling with arbitrary time-delay. However, stronger coupling introduces significant modifications which also very much depend on the time-lag as is illustrated in fig. 1,2.

Fig. 1

In fig.1a,b we show typical effects of small time-lag, illustrated with $\tau = 0.4$ and $\tau = 0.7$, on functions $SISR1(\log_{10} D_2)$ and $SISR2(\log_{10} D_2)$, when both neurons are of the SC type and the noise intensity of one of them (second) is held fixed at the SC maximum. We can see that those values of the time-lag less then $\tau < 1$ cause similar small modifications of the dependencies $SISR1(\log_{10} D_2)$ and $SISR2(\log_{10} D_2)$. However, large influence of the time-delay on $SISR1(\log_{10} D_2)$ and $SISR2(\log_{10} D_2)$ is demonstrated for all $\tau \geq 1$, as is illustrated in fig.2 a,b,c for $\tau = 1$, $\tau = 1.1$ and $\tau = 1.3$ respectively. The curves $SISR1(\log_{10} D_2)$ and $SISR2(\log_{10} D_2)$ with $\tau \geq 1$ are qualitatively and quantitatively different from those with $\tau < 1$. Let us stress that deterministic system with delayed coupling of the same coupling strength $c = 0.1$ show no bifurcation or other qualitative change for any $\tau \geq 0$. Thus, qualitative change in the properties of noise induced spiking coherence achieved with $\tau \geq 1$ should be attributed to the simultaneous action of noise and time-delay.

Fig. 2

Figure 2d illustrate the influence of time-delay on coincidence of spiking of the two neurons as measured by the coincidence function. Obviously, when there is no interaction time-delay spike in one neuron immediately causes the other neuron to fire so the spikes largely overlap and are considered coincident. Spikes also coincide when the time-lag is close to the inter-spike interval, if such is relatively well defined. Otherwise nonzero interaction time-lag destroys the coincidence of spiking. As the noise becomes larger the coincidence that occurs at special values of time-lag decreases.

In summary we can conclude that small time-lag $\tau < 1$ only slightly changes the properties of noise induced coherence in each of the considered cases. On the other hand $\tau \geq 1$ introduces significant qualitative and quantitative changes in the functions which characterize the noise induces coherence $SISR1$ and $SISR2$. The firing coherence of both neurons as measured by $SISR1(\log_{10} D_2)$ and $SISR2(\log_{10} D_2)$ is significantly smaller for any D_2 for $\tau = 1$ then for $\tau < 1$. The local maxima in $SISR1(\log_{10} D_2)$ and $SISR2(\log_{10} D_2)$ that appear for $\tau > 1$ must be considered as a consequence of very small variance over long time of the inter-spike intervals and not of large values of these intervals. In figure 3 we illustrate the coherent oscillations achieved with $\tau = 1.3$ and compare the time series with that for $\tau = 1$ and $\tau < 1$. It is obvious that the coherence is significantly improved in the case $\tau = 1.3$ compared to $\tau \leq 1$ even though the frequency of the spiking is also increased. Let us stress once again that the two deterministic FHN neurons in the considered range of the parameters with delayed coupling do not display any oscillatory dynamics for any value of time-lag.

Fig. 3

4. Summary

We have studied a pair of FitzHugh-Nagumo neurons with noise coupled by time-delay diffusive coupling. The bifurcation parameters of each of the neurons and the coupling strength were such that the only attractor of the system without the noise terms is the stable stationary state for any value of the time-lag. Thus the deterministic system is excitable with no oscillatory dynamics for any value of the time-lag. Addition of white noise in second equation produces spiking that appears periodic for particular values of the noise strength. We have studied the influence of time-delay in the coupling on the coherent spiking induced by noise in the slow variable, called stochastic coherence (SC). This research is complementary to analyzes of the effects of noise on the properties of oscillations and synchrony introduced by sufficient time-lag in the delayed coupling. Noise induced coherent spiking is studied using the signal to noise ratio and coincidence between the two neurons was measured using the coincidence function. As pointed before, the isolated neurons without noise were always in the excitable regime and the coupling strength was always positive, which guaranties that the train of spikes can only be introduced by noise, and not by time-delay. Then we numerically studied changes in the signal to noise ratio introduced by small time-delay for each of the neurons in the pairs of SC-SC. Our main results can be summarized as follows: a coupled pair of SC-SC with the time-lag $\tau < 1$ induces only small changes to the signal to noise ratio. However, the time-lag $\tau \geq 1$ and sufficiently strong coupling drastically change signal to noise ratio in the quantitative and qualitative way. New local minima and maxima of the signal to noise ratio as a function of the noise strength are created by the time-lag $\tau > 1$, and the coherence of spiking measured by (3) can be greatly enhanced. We also observed coincident spiking for small noise intensity and time-lag proportional to the inter-spike interval of the coherent spike trains.

Acknowledgement. This work is partly supported by the Serbian Ministry of Science contract No.174010

References

[1] Izhikevich E.M.(2005) *Dynamical Systems in Neuroscience: The Geometry of Excitability and Bursting*, MIT Press.
[2] Mainen Z.F. and Sejnowski T.J. (1995), Science **268**, 1503.
[3] Linder B., Garcia-Ojalvo, Neiman A. and Schimansky-Geier L.(2004*) Phys. Rep*. **392**, 321.
[4] Lee DeVille R.E., Vanden-Ejinden E. and Muratov C.B. (2005) *Phys.Rev.E*, **72**, 031150.
[5] Kandel E.R. Schwartz J. H. and Jessel T. M.(1991) *Principles of Neural Sciences,* 3rd. ed. Elsevier, New York.
[6] Strogatz S. H.(1998) *Nature*(London), **394**, 316.
[7] Burić N. And Todorović D. (2003) *Phys.Rev.E*, **67**, 066222.
[8] Burić N., Grozdanović I. and Vasović N. (2005), *Chaos Solitons and Fractals* **23**, 1221.
[9] Dhamala M. Jirsa V.K. and Ding M. (2004), *Phys.Rev.Lett,* **92**, 074104.
[10] Rossoni E. Chen Y. Ding M and Feng J. (2005) *Phys.Rev.E*, **71**, 061904.
[11] Liao X. and Mao X. (2001), *Stochast. Anal.Appl.* **14**, 165.
[12] Blythe S. Mao X. and Liao X.(2001) *J.Franklin Inst.* **338**,481.
[13] Burić N. Todorović K. And Vasović N.,(2008) *Phys.Rev E*, **78**, 036211.

[14] Janson N.B. Balanov and A.G. Scholl (2004), *Phys.Rev.Lett.*,**93**, 010601.
[15] Sainz-Trapaga M. Masoller M.C Braun H.A and Huber M.T.(2004), **70** 031904
[16] Pikovsky A.S and Kurths J. (1997), *Phys.Rev.Lett.*, **78**, 775.
[17] Zhang J. Yuan Z Wang J. and Zhou T. (2008), *Phys.Rev. E*, **77**, 021101.
[18] Han S.K. Yin T.G. Postnov D.E. and Sosnovceva O.V. (1999), *Phys.Rev.Lett.* **83**, 1771.
[19] Kistler W. Gesrner W. and Hemmen Van J. (1997), *Neural computation*, **9**, 1015.

FIGURE CAPTIONS

Figure1: Illustrates coherence in the SC-SC case. D_2 of the second (SC) neuron is fixed to $D_2 = 0.01$. D_2 of the second neuron, shown on the axes as $\log_{10} D_2$ is adjustable. $SISR1$ (circles) and $SISR2$ (triangles), for $\tau = 0$ (1a,1b black line), $\tau = 0.4$ (1a, red/gray line) and $\tau = 0.7$ (1b, green/gray line) are shown. Calculated values of $SISR1,2$ are indicated by symbols and the lines serve only to connect the values corresponding to the same τ and different $\log_{10} D_2$.

Figure2: Illustrates coherence in the SC-SC case. D_2 of the second (SC) neuron is fixed to $D_2 = 0.01$. D_2 of the second neuron, shown on the axes as $\log_{10} D_2$ is adjustable. $SISR1$ (circles) and $SISR2$ (triangles), for $\tau = 0$ (2a,b black line), $\tau = 0.1$ (2a, orange/gray line), $\tau = 1.1$ (2b, blue/gray line) and $\tau = 1.3$ (2c, cyan/gray) are shown. In 2d coincidence functions C for $\tau = 0$ (black full line), $\tau = 1$ (black dotted line) and $\tau = 2.7$ (gray dotted line) are shown. Calculated values of $SISR1,2$ and C are indicated by symbols and the lines serve only to connect the values corresponding to the same τ and different $\log_{10} D_2$.

Figure3: Time series $x_1(t)$ with $D_2 = 0.01$ for the first neuron and for 3a) $\tau = 0$, $D_2 = 0.01$ for the second; 3b) $\tau = 0$, $D_2 = 0.001$ for the second; 3c) $\tau = 1$, $D_2 = 0.01$ for the second and 3d) $\tau = 1.3$, $D_2 = 0.001$, corresponding to a local coherehce maxima in fig.2c, for the second.

OPTIMUM GIRDER DESIGN WITH MULTIPLE FUNCTIONS

Tomislav Igić[1], Dragana Turnić[2]

[1] Civil Engineering Faculty and Architecture,
University of Nis, Aleksandra Medvedeva 14, 18000 Nis, Serbia
e-mail: tomislav.igic@gaf.ni.ac.rs
[2] Civil Engineering Faculty and Architecture,
University of Nis, Aleksandra Medvedeva 14, 18000 Nis, Serbia
e-mail: draganaturnic@yahoo.com

ABSTRACT. The paper considers the case of optimum design of structures with multipurpose constraint functions.
A part of the paper addresses the general optimum criterion and it is focused on the case of optimum design of the girders with two behaviour constraint functions. There are frequent considerations of optimum design cases of multiple loads with one constraint function or of optimum design cases of single loads that are individually associated to one constraint function. As opposed to them, the problems of multipurpose behaviour constraints of structures are rare and more complex.
This paper presents an optimum design of beams with two functions referring to different physical behaviours . Each of them is related to different energies; one behaviour is elastic with bending ellastic deformation energy and the other is plastic behavior with plastic energy dissipation. Examples of such optimum designs are given in the paper.

Keywords: optimum design, multipurpose behavior constraints, plasticity.

1. Introduction

The optimum conditions related to successive generalizations of the function of cost, and to the various load conditions or behaviour constraints. Cases where optimization is treated under multiple loads are associated with the same behaviour constraint are frequent. There are also loads which are individually loaded with one behaviour constraint which is of the physical nature. This category of problems is relatively new, and optimizations for multiple functions of behaviour constraints under different loads are rare. In this paper is presented the optimum condition with two functions formulated by the various physical behaviour, elastic on one end and plastic on the other. The optimum criterion is obtained observing the general optimum criterion. The examples taken are of the optimum beam design with practical behaviour limitations: the limit load an characteristic generalized displacement in the elastic region.

2. Optimum condition

Designing of the structure is aimed to define the sense in which we wish to achieve optimization. One of the cases is determining the least structural weight, and also very frequent case is minimization of structure cost C in its broader sense. The parameters e_1, e_2,... are variable designing parameters, for instance, shell thickness.

An assumption that C (D_a, D_b,..., D_u) is a convex function is introduced. Each behaviour constraint function is added according to the principle of the minimum. Thus there is the inequation

$$\int D_b\left(q_{i,b}\right)d\xi \geq \int D_b^I\left(q_{i,b}\right)d\xi \tag{1}$$

where it is assumed that dimensioning number I is satisfied by the behaviour constraint relation with the equality sign, and that dimensioning number II, which is acceptable, is satisfied both by the sign of equality and of the inequality.
The optimum criterions is: „If any dimensioning satisfies "u" functions of behaviour constraint with the sign of equality the expression

$$\frac{\partial C}{\partial D_i} = \alpha_i > 0 \tag{2}$$

is sufficient to make this dimensioning optimum.

2.1. The optimum condition for two functions of behaviour constraint

From the optimum criterion (2) here the criterion condition becomes:

$$\frac{\partial C}{\partial D_a} = \alpha_a > 0\,, \qquad \frac{\partial C}{\partial D_b} = \alpha_b > 0\,, \tag{3}$$

where α_a and α_b are constants.
The behaviour constraint functions are here the bending elastic deformation energy and the specific energy of plastic deformation D_b.
There is:

$$D_a = \frac{B}{2} k\bar{k}\,, \tag{4}$$

here:

B- is the rigidity of the girder,

$k, \bar{k}$ - is the curve of elastic line;

$$D_b = M_p\left|\dot{k}\right|, \tag{5}$$

where M_p is the moment of plasticity. Starting from relation $C=ab$, the following is obtained

$$\alpha_a\beta_a k\bar{k} + \alpha_b\beta_b\left|\dot{k}\right| = \alpha \tag{6}$$

As α_a, α_b and α are random designed constants, and when taking care about the accuracy degree $\dot{k}$, the expression (6) gets the following form:

$$\gamma k\bar{k} + \left|\dot{k}\right| = 1 \tag{7}$$

and this represents the optimum condition in the case when these constraints have influence on the optimum dimensioning of the girder.

3. Optimum design

Without any limitations to our considerations let us take a random form of optimum continuous load of the intensity *p(x)* which is symmetrical in respect to the middle of the simple beam freely supported on its ends.
For the beam there is a limit load defined by the factor s and there is a limitation of displacement at the center of the beam $\delta\left(\frac{L}{2}\right)$. The function of the cost will be chosen so as the beam is designed with minimum usage of material.
We assume that a part of beam will be in the elastic zone, and the remaining parts in the completely plasticized zone at the moment of failure.
In this manner will the condition for the zone $0 \le x \le a$ will include both behavior constraint functions, thus the following is obtained:

$$\gamma k \bar{k} \le 1 \quad . \tag{8}$$

Regarding that the relation of the beam rigidity and the bending moment has the following form

$$B = \frac{sM}{d}, \tag{9}$$

at the border of the interval, from the condition

$$\gamma k \bar{k} = 1 \tag{10}$$

it is obtained:

$$\gamma = \frac{2s^2 M(p,a)}{ad^2} \tag{11}$$

Combination of the expressions (9) and (11) is written as

$$\frac{M(p,a)}{aM} < 1 \qquad (0 \le \mathrm{x} \le \mathrm{a}) \tag{12}$$

If now the condition that the maximum displacement of the beam in the middle has been reached is expressed in the following way

$$\int_0^a \frac{M\overline{M}}{B_1} dx + \int_a^{L/2} \frac{M\overline{M}}{B_2} dv = \frac{kL}{2}, \tag{13}$$

that is,

$$\frac{2}{m_1}\left(\int_0^a \overline{M}dx+\sqrt{\frac{\overline{M}(1,a)}{M(p,a)}}\int_a^{L/2}\left(M\overline{M}\right)^{\frac{1}{2}}dx\right)=kL\,, \tag{14}$$

the sought dimensioning b(x) are obtained from the expression B_1 and $B_2=\sqrt{\gamma M\overline{M}}$.

3.1 Freely supported beam with constant evenly distributed load

Starting form the expression from the bending moment in this case

$$M(p,x)=\frac{px}{2}(L-x) \tag{15}$$

The condition (12) obtains the form

$$\frac{L-a}{L-x}<1 \qquad (0 \le x \le a) \tag{16}$$

the limit value of plastic and elastic zone is now determined, and after integration, those are the equations

$$\frac{da^2}{2s}+\frac{2d}{15s\sqrt{L-a}}\left[(3a+2L)(L-a)^{3/2}-\frac{7L^{5/2}}{4\sqrt{2}}\right]=kL\,, \tag{17}$$

and the dimensioning expressions are:

$$B_1=\frac{spx}{2d}(L-x) \quad ; \tag{18}$$

$$B_2=\frac{spx}{2d}\sqrt{(L-a)(L-x)}\,. \tag{19}$$

When this case of dimensioning is in question, one should endeavor to avoid the trivial case of dimensioning, which is indicated in (5).

Parameter $\alpha=Ld/kS$ determines the area in which both constrains will be simultaneously valid, and that is:

$$8\le\alpha\le 9{,}835 \tag{20}$$

For the values below the lower limit, dimensioning will be determined, and the plastic dimensioning will be relevant, while for $\alpha > 9{,}835$ the optimum dimensioning will be in the elastic zone only.

3.2 The case of the beams with technological limitations

The problem of the beam considered in the previous part of the paper will be extended by the requirement that there is a lower limit of the girder width b_0. In this manner the actual girder, in which there is influence of the transversal force, will be able to receive this influence. We are looking for the optimum design of the beam of minimum volume, requiring:

- That the minimum width of the beam is b_0, i.e. $b(x) \geq b_0$;
- That due to the evenly distributed load p the displacement of the middle of the beam is within previously set range;
- That the failure load parameter is higher than the previously set values (see Fig.1.)

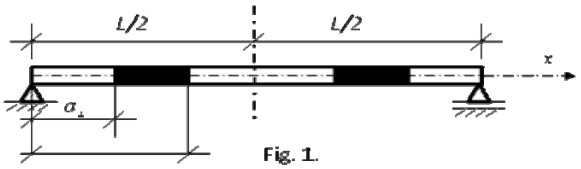

Fig. 1.

The optimum condition for the zone $a_1 \leq x \leq a_2$, becomes:

$$\frac{xM(p,a_2)}{a_2 M} < 1, \tag{21}$$

For the zone $0 \leq x \leq a_1$

$$\frac{xMM(p,a_2)}{a_2 M^2(p,a_1)} < 1; \qquad (0 \leq x \leq a_1) \tag{22}$$

3.2.1 Constant distributed load

The optimum criterion becomes

$$\frac{L-a_2}{L-x} < 1 \qquad ; \qquad (a_1 \leq x \leq a_2)$$

$$\frac{x^2(L-x)(L-a_2)}{a_1^2(L-a_1)^2} < 1 \qquad ; \qquad (0 \leq x \leq a_1) \quad .$$

For dimensioning, the following condition is used

$$\int_0^{a_1} \frac{M\overline{M}}{B_0} dx + \int_{a_1}^{a_2} \frac{d}{s}\overline{M} dx + \int_{a_2}^{L/2} \sqrt{\frac{M\overline{M}}{\gamma}} dx = \frac{kL}{2} \tag{23}$$

and the following is obtained:

$$b(x) = b_0 \qquad (0 \le x \le a_1) \tag{24}$$

$$Y(x) = sM(p,x) \qquad (a_1 \le x \le a_2) \tag{25}$$

$$B(x) = \sqrt{8M\overline{M}} \qquad (a_2 \le x \le L/2) \tag{26}$$

In the special case, when B_0=0, the beam with technological limitations is reduced to the case of the beam without technological limitations which has already been considered, and for which a_1=0 and a_2=a. If then the value is a=0, we will have such optimum dimensioning in the elastic zone which can resist the anticipated plastic failure load.
In the other limit case, when *a=L/2*, we will have such optimum plastic dimensioning which is capable to meet the condition that the maximum displacement is lower than the previously sat value of this displacement.
The borders of the valid zone of elastic, mixed and only plastic dimensioning are determined by the relation (20).

3. Cantilever beam case

In this case, the bending moment is given by the expression

$$M = -\frac{p_0 x^2}{2} \quad . \tag{27}$$

The optimum condition for the zone a ≤ x ≤ L is in the plastic zone (Fig. 2.). The optimum condition for this zone yields

$$\frac{a}{x} < 1 \tag{28}$$

and it is satisfied in all the points of the plasticized zone because x>a.

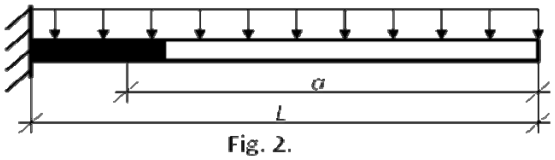

Fig. 2.

For determination of the plasticized zone, we start from the equation

$$\frac{1}{m_1}\left(\sqrt{\frac{-a}{M(p,a)}}\int_0^a (M\overline{M})^{1/2}\,dx - \int_a^1 x\,dx\right) = kL \tag{29}$$

After determining the value of the integral and after arrangement, the following is obtained

$$9a^2 - 5L^2 = 10kLm \quad . \tag{30}$$

Two behaviour constraint functions of the cantilever beam will have simultaneous effects in dimensioning if the parameter β is in the range

$$-0{,}5 \le \beta \le 0{,}4 \tag{31}$$

Purely elastic optimum dimensioning at the action of the load sp_0 will be capable not to sustain plastic failure at the previously set value of the load parameter in this zone when $\beta \ge 0{,}4$. For $-0{,}5 \ge \beta$ we have purely plastic optimum design for which the maximum displacement, that is displacement of the free end of the cantilever is smaller than the previously set displacement limit.

4 Conclusions

(a) This paper laid out the optimum conditions and optimum plastic dimensioning examples of the beam supported on two points, separately for two zones in the surrounding of the support points and for the central zone of the beam. It has been proved that the zones in surrounding the support points are plasticized, and that the central zone is in the elastic zone and the validity ranges of two behavior constraint functions have been determined.
(b) An example of a cantilever beam was presented for which the optimum condition was determined where two behavior constraint functions are valid. Here, too, was determined a zone when there is only elastic, only plastic and mixed optimum dimensioning.
(c) The examples of simpler beams presented here represent a basis for solution of other more complex cases in an analogous way, and comprise a sort of a catalogue of solutions of simpler problems which can also serve for assessment of quality of approximate dimensioning which is solved in the framework of numerical analysis.

This research was conducted in the framework of the research program in the field of technological development in the period 2011-2014, in the domain of Transport, town planning and civil engineering, project no. 36016, entitled Experimental and theoretical research of linear and planar systems with semi-rigid joints from the aspect of second order theory and stability University of Nis, The Faculty of Civil Engineering and Architecture.

References

[1] Cheu C. Y., Prager W., Optimal Design of Sandwich Beams For Elastic Deflection and Load Factor at Plastic Collapse, *Journal of Appl. Math. and Physics, Z.A.M.P.*, (1969), p. 289-297.
[2] Save M., Igic T., Examples de poutres optimales a deux fonctions, *Journal de Mecanique theorique et appliqué (European Journal of Mechanics)*, (1982), p. 311-322.

[3] Save M. A., Prager W., Minimum-Weight Design of Beams Subjected to Fixed and Moving Loads, *Journal of Mechanics and Physics of Solids*, Vol.11, 1963., pp.255-267.
[4] Save M. A., Shield R. T.., Minimum-Weight Design of Sandwich Shells Subjected to Fixed and Moving Loads, *Proceedings of the 11th International Congress of Applied Mechanics,* Munich, Germany, 1964.
[5] Igić T., Contribution au dimensionnement optimal des structures, *These de doctorat,* Faculty of Civil Engineering, Niš, 1980.
[6] Prager W., Shield R. T., Optimal Design of Multipurpose Structures, *Int. J. of Solids and Structures,* Vol. 4, 1968., pp 469-475.
[7] Igić T., Turnić D., Marković N., Design of a System for Control, Monitoring, Regulation and Data Acquistion (CMRA) on Civil Engineering Objects, Constructions and Mobile Modules, *7th EUROMECH Solid mechanics Conference, J. Ambosioet et. al.* Lisbon, Portugal, 2009.
[8] Adrade-Campos A., Development of an Optimization Framework for Parameter Identification and Shape Optimization Problems in Engineering, *7th EUROMECH Solid mechanics Conference, J. Ambosioet et. al.* Lisbon, Portugal, 2009.

MOMENT LYAPUNOV EXPONENTS AND STOCHASTIC STABILITY OF A THIN-WALLED BEAM DRIVEN BY REAL NOISE

G. Janevski[1], P. Kozić[2], I. Pavlović[3]

[1] University of Niš, Department of Mechanical Engineering, Medvedeva 14, 18000 Niš, Serbia, e-mail: gocky.jane@gmail.com
[2] University of Niš, Department of Mechanical Engineering, Medvedeva 14, 18000 Niš, Serbia, e-mail: kozicp@yahoo.com
[3] University of Niš, Department of Mechanical Engineering, Medvedeva 14, 18000 Niš, Serbia, e-mail: ivanp79@gmail.com

Abstract. The Lyapunov exponent and moment Lyapunov exponents of two degrees-of-freedom linear systems subjected to real noise are investigated. The method of regular perturbation is used to determine the explicit asymptotic expressions for these exponents in the presence of small intensity noises. The Lyapunov exponent and moment Lyapunov exponents are important characteristics for determining the almost-sure and moment stability of a stochastic dynamic system. As an example, we study the almost-sure and moment stability of a thin-walled beam subjected to eccentric stochastic axial load.

1. Introduction

In recent years there has been considerable interest in the study of the dynamic stability of non-gyroscopic conservative elastic systems whose parameters fluctuate in a stochastic manner. To have a complete picture of the dynamic stability of a dynamic system, it is important to study both the almost-sure and the moment stability and to determine both the maximal Lyapunov exponent and the *p*th moment Lyapunov exponent. The maximal Lyapunov exponent, defined by

$$\lambda_q = \lim_{t\to\infty} \frac{1}{t} \log \left\| \boldsymbol{q}(t;q_0) \right\|. \tag{1}$$

where $\boldsymbol{q}(t;q_0)$ is the solution process of a linear dynamic system. The almost-sure stability depends upon the sign of the maximal Lyapunov exponent which is an exponential growth rate of the solution of the randomly perturbed dynamic system. A negative sign of the maximal Lyapunov exponent implies the almost-sure stability, whereas a non-negative value indicates instability. The exponential growth rate $E[\left\| \boldsymbol{q}(t;q_0,\dot{q}_0) \right\|^p]$ is provided by the moment Lyapunov exponent defined as

$$\Lambda_q(p) = \lim_{t\to\infty} \frac{1}{t} \log E[\left\| \boldsymbol{q}(t;q_0) \right\|^p]. \tag{2}$$

where $E[\ ]$ denotes the expectation. If $\Lambda_q(p) < 0$, then, by definition $E[\|\boldsymbol{q}(t;q_0,\dot{q}_0)\|^p] \to 0$ as $t \to \infty$ and this is referred to as the *p*th moment stability. Although the moment Lyapunov exponents are important in the study of the dynamic stability of stochastic systems, the actual evaluations of the moment Lyapunov exponents are very difficult.

Arnold et al. [1] constructed an approximation for the moment Lyapunov exponents, the asymptotic growth rate of the moments of the response of a two-dimensional linear system driven by real or white noise. A perturbation approach was used to obtain explicit expressions for these exponents in the presence of small intensity noises. Khasminskii and Moshchuk [2] obtained an asymptotic expansion of the moment Lyapunov exponents of a two-dimensional system under white noise parametric excitation in terms of the small fluctuation parameter ε, from which the stability index was obtained. Sri Namachchivaya et al. [3] used a perturbation approach to calculate the asymptotic growth rate of a stochastically coupled two-degrees-of-freedom system. The noise was assumed to be white and of small intensity in order to calculate the explicit asymptotic formulas for the maximum Lyapunov exponent. Sri Namachchivaya and Van Roessel [4] used a perturbation approach to obtain an approximation for the moment Lyapunov exponents of two coupled oscillators with commensurable frequencies driven by small intensity real noise with dissipation. The generator for the eigenvalue problem associated with the moment Lyapunov exponents was derived without any restriction on the size of *p*th moment. Kozić et al. [5, 6] investigated the Lyapunov exponent and moment Lyapunov exponents of two degrees-of-freedom linear systems subjected to white noise parametric excitation. In the first, almost-sure and moment stability of the flexural-torsion stability of a thin elastic beam subjected to a stochastically fluctuating follower force were studied. In the second, moment Lyapunov exponents and stability boundary of the double-beam system under stochastic compressive axial loading were obtained. Pavlović et al. [7] investigated the dynamic stability of thin-walled beams subjected to combined action of axial loads and end moments. By using the direct Lyapunov method, the authors obtained the almost-sure stochastic boundary and uniform stochastic stability boundary as the function of characteristics of stochastic process and geometric and physical parameters.

The aim of this paper is to determine an asymptotic expansion for the moment Lyapunov exponent of the four-dimensional stochastic system under real noise excitation, which is modelled as an Orstein-Uhlenbeck process. The noise is assumed to be white noise of small intensity such that one can obtain an asymptotic growth rate. We apply the perturbation theoretical approach given in Khasminskii and Moshchuk [2] to obtain second-order weak noise expansions of the moment Lyapunov exponents. The Lyapunov exponent is then obtained using the relationship between the moment Lyapunov exponents and the Lyapunov exponent. These results are applied to study the *p*th moment stability and almost-sure stability of a thin-walled beam subjected to eccentric stochastic axial loads. The stability regions for the I-cross section and narrow rectangular cross section are shown in the plane of variances of stochastic force and viscous damping coefficient. The motion of such an elastic system is governed by the partial differential equations in the paper by Pavlović et al. [7].

2. Theoretical formulation

Consider linear oscillatory systems described by equations of motion of the form

$$\begin{aligned} &\ddot{q}_1 + \omega_1^2 q_1 + 2\varepsilon^2\beta_1\dot{q}_1 - \varepsilon\xi(t)\left(K_{11}q_1 + K_{12}q_2\right) = 0, \\ &\ddot{q}_2 + \omega_2^2 q_2 + 2\varepsilon^2\beta_2\dot{q}_2 - \varepsilon\xi(t)\left(K_{21}q_1 + K_{22}q_2\right) = 0, \end{aligned} \tag{3}$$

where q_1, q_2 are generalized coordinates, ω_1, ω_2 are natural frequencies and $2\varepsilon^2\beta_1, 2\varepsilon^2\beta_2$ represent small viscous damping coefficients and $\xi(t)$ is an Ornstein –Uhlenbeck process given by

$$d\xi(t) = -\alpha\xi(t)dt + \sigma dW(t)\,, \tag{4}$$

where $W(t)$ is a standard Wiener process with. The correlation function and spectral density of the Ornstein-Uhlenbeck process $\xi(t)$ are

$$R(T) = \frac{\sigma^2}{2\alpha}e^{-\alpha|T|}, \quad S(\Omega) = \frac{\sigma^2}{\alpha^2 + \Omega^2}\,. \tag{5}$$

Using the transformation

$$q_1 = x_1,\ \dot{q}_1 = \omega_1 x_2,\ q_2 = x_3,\ \dot{q}_2 = \omega_2 x_4\,, \tag{6}$$

and denoting

$$p_{ij} = \frac{K_{ij}}{\omega_i}\,,\ (i, j=1,2), \tag{7}$$

the above Eq.(3) can be represented in the first-order form by a set of stochastic differential equations

$$\frac{dX}{dt} = \left(A_0 + \varepsilon^2 A\right)X + \varepsilon B\,\xi(t)X\,, \tag{8}$$

where $\mathbf{X} = \left(x_1 \quad x_2 \quad x_3 \quad x_4\right)^T$ is the state vector of the system and matrices A_0, A and B are constant 4×4 matrices given by

$$A_0 = \begin{bmatrix} 0 & \omega_1 & 0 & 0 \\ -\omega_1 & 0 & 0 & 0 \\ 0 & 0 & 0 & \omega_2 \\ 0 & 0 & -\omega_2 & 0 \end{bmatrix},\ A = \begin{bmatrix} 0 & 0 & 0 & 0 \\ 0 & -2\beta_1 & 0 & 0 \\ 0 & 0 & 0 & 0 \\ 0 & 0 & 0 & -2\beta_2 \end{bmatrix},\ B = \begin{bmatrix} 0 & 0 & 0 & 0 \\ p_{11} & 0 & p_{12} & 0 \\ 0 & 0 & 0 & 0 \\ p_{21} & 0 & p_{22} & 0 \end{bmatrix}. \tag{9}$$

Applying the transformation

$$\begin{aligned} &x_1 = a\cos\varphi\cos\theta_1,\quad x_2 = -a\cos\varphi\sin\theta_1,\quad x_3 = a\sin\varphi\cos\theta_2,\quad x_4 = -a\sin\varphi\sin\theta_2, \\ &P = \|a\|^p = (x_1^2 + x_2^2 + x_3^2 + x_4^2)^{p/2}, \\ &0 \le \theta_1 \le 2\pi,\quad 0 \le \theta_2 \le 2\pi,\quad 0 \le \varphi \le \pi/2\,,\quad -\infty < p < \infty, \end{aligned} \tag{8}$$

yields the following set of Itô stochastic equations for the *p*th power of the norm of the response and phase variables $(\varphi, \theta_1, \theta_2)$

$$\begin{aligned} dP &= P\sum_{j=1}^{2}\varepsilon^j g_j(\xi,\varphi,\theta_1,\theta_2)dt, \quad d\varphi = \sum_{j=1}^{2}\varepsilon^j s_j(\xi,\varphi,\theta_1,\theta_2)dt, \\ d\theta_i &= \left[\omega_1 + \sum_{j=1}^{2}\varepsilon^j h_{ij}(\xi,\varphi,\theta_1,\theta_2)\right]dt, \quad i = 1,2. \end{aligned} \tag{9}$$

In the above transformations, *a* represents the norm of the response, θ_1 and θ_2 are the angles of the first and second oscillators, respectively, and φ describes the coupling or exchange of energy between the first and second oscillator. In the previous equation we introduced the following marking

$$\begin{aligned} &g_1(\xi,\varphi,\theta_1,\theta_2) = \xi(t)g_{10}(\varphi,\theta_1,\theta_2), \quad s_1(\xi,\varphi,\theta_1,\theta_2) = \xi(t)s_{10}(\varphi,\theta_1,\theta_2), \\ &g_{10}(\varphi,\theta_1,\theta_2) = -\frac{1}{4}p\left(p_{11}\sin 2\theta_1 + p_{22}\sin 2\theta_2\right) - \frac{1}{4}p\left(p_{11}\sin 2\theta_1 - p_{22}\sin 2\theta_2\right)\cos 2\varphi \\ &\qquad - \frac{1}{2}p\left(p_{12}\sin\theta_1\cos\theta_2 + p_{21}\cos\theta_1\sin\theta_2\right)\sin 2\varphi, \\ &s_{10}(\varphi,\theta_1,\theta_2) = \frac{1}{2}\left(p_{12}\sin\theta_1\cos\theta_2 - p_{21}\cos\theta_1\sin\theta_2\right) \\ &\qquad - \frac{1}{2}\left(p_{12}\sin\theta_1\cos\theta_2 + p_{21}\cos\theta_1\sin\theta_2\right)\cos 2\varphi + \frac{1}{4}\left(p_{11}\sin 2\theta_1 - p_{22}\sin 2\theta_2\right), \\ &g_2(\xi,\varphi,\theta_1,\theta_2) = -\frac{1}{2}p\left[\beta_1\left(1-\cos 2\theta_1\right) + \beta_2\left(1-\cos 2\theta_2\right)\right] \\ &\qquad + \frac{1}{2}p\left[-\beta_1\left(1-\cos 2\theta_1\right) + \beta_2\left(1-\cos 2\theta_2\right)\right]\cos 2\varphi, \\ &s_2(\xi,\varphi,\theta_1,\theta_2) = \frac{1}{2}\left[\beta_1\left(1-\cos 2\theta_1\right) - \beta_2\left(1-\cos 2\theta_2\right)\right]\sin 2\varphi, \\ &h_{11}(\xi,\varphi,\theta_1,\theta_2) = -\frac{1}{2}\xi(t)\left[p_{11}\left(1+\cos 2\theta_1\right) + p_{12}\cos\theta_1\cos\theta_2 \operatorname{tg}\varphi\right], \\ &h_{21}(\xi,\varphi,\theta_1,\theta_2) = -\frac{1}{2}\xi(t)\left[p_{22}\left(1+\cos 2\theta_2\right) + p_{21}\cos\theta_1\cos\theta_2\cot\varphi\right], \\ &h_{12}(\xi,\varphi,\theta_1,\theta_2) = -\beta_1\sin 2\theta_1, \quad h_{22}(\xi,\varphi,\theta_1,\theta_2) = -\beta_2\sin 2\theta_2. \end{aligned} \tag{10}$$

Following Wedig [8], we perform the linear stochastic transformation

$$S = T(\xi,\varphi,\theta_1,\theta_2)P, \quad P = T^{-1}(\xi,\varphi,\theta_1,\theta_2)S, \tag{11}$$

introducing the new norm process S by means of the scalar function $T(\xi,\varphi,\theta_1,\theta_2)$ which is defined in the stationary phase processes θ_1, θ_2 and φ

$$dS = P\left[L_0 + \varepsilon_1 L_1 + \varepsilon_1^2 L_2\right]\ T(\xi,\varphi,\theta_1,\theta_2)dt. \tag{12}$$

Here L_0, L_1 and L_2 are the following first and second-order differential operators

$$\begin{aligned} L_0 &= \frac{1}{2}\sigma^2 \frac{\partial^2}{\partial \xi^2} - \alpha\xi \frac{\partial}{\partial \xi} + \omega_1 \frac{\partial}{\partial \theta_1} + \omega_2 \frac{\partial}{\partial \theta_2}, \\ L_1 &= s_1 \frac{\partial}{\partial \varphi} + h_{11} \frac{\partial}{\partial \theta_1} + h_{21} \frac{\partial}{\partial \theta_2} + q_1, \\ L_2 &= s_2 \frac{\partial}{\partial \varphi} + h_{12} \frac{\partial}{\partial \theta_1} + h_{22} \frac{\partial}{\partial \theta_2} + q_2. \end{aligned} \tag{13}$$

If the transformation function $T(\xi, \varphi, \theta_1, \theta_2)$ is bounded and non-singular, both processes P and S possess the same stability behavior. Therefore, transformation function $T(\xi, \varphi, \theta_1, \theta_2)$ is chosen so that the drift term, of the Itô differential Eq. (12), does not depend on the phase processes ξ, θ_1, θ_2 and φ, so that

$$dS = \Lambda(p)\, S dt = P\Lambda(p)\, T(\xi, \varphi, \theta_1, \theta_2) dt\,. \tag{14}$$

By comparing Eqs. (12) and (14), it can be seen that such a transformation function $T(\xi, \varphi, \theta_1, \theta_2)$ is given by the following equation

$$\left[L_0 + \varepsilon_1 L_1 + \varepsilon_1^2 L_2\right]\, T(\xi, \varphi, \theta_1, \theta_2) = \Lambda(p) T(\xi, \varphi, \theta_1, \theta_2)\,. \tag{15}$$

Eq. (15) defines an eigenvalue problem for a second-order differential operator of three independent variables, in which $\Lambda(p)$ is the eigenvalue and $T(\xi, \varphi, \theta_1, \theta_2)$ the associated eigenfunction. From Eq. (14), the eigenvalue $\Lambda(p)$ is seen to be the Lyapunov exponent of the *p*th moment of system (8). This approach was first applied by Wedig [8] to derive the eigenvalue problem for the moment Lyapunov exponent of a two-dimensional linear Itô stochastic system. In the following section, the method of regular perturbation is applied to the eigenvalue problem (15) to obtain a weak noise expansion of the moment Lyapunov exponent of a four-dimensional stochastic linear system (3).

3. Weak noise expansion of the moment Lyapunov exponent

Applying the method of regular perturbation, both the moment Lyapunov exponent $\Lambda(p)$ and the eigenfunction $T(\xi, \varphi, \theta_1, \theta_2)$ are expanded in power series of ε as

$$\Lambda(p) = \sum_{i=0}^{n} \varepsilon^i \Lambda_i(p), \quad T(\xi, \varphi, \theta_1, \theta_2) = \sum_{i=0}^{n} \varepsilon^i T_i(\xi, \varphi, \theta_1, \theta_2). \tag{16}$$

Substituting the perturbation series (16) into the eigenvalue problem (15) and equating terms of the equal powers of ε leads to the following equations

$$\begin{aligned} &L_0 T_0 = \Lambda_0(p) T_0, \\ &L_0 T_1 + L_1 T_0 = \Lambda_0(p) T_1 + \Lambda_1(p) T_0, \\ &\sum_{k=0}^{2} L_k T_{j-k} = \sum_{i=0}^{2} \Lambda_i(p) T_{j-i}, \quad j = 2, 3, 4 \ldots n \end{aligned} \tag{17}$$

where each function $T_i = T_i(\xi, \varphi, \theta_1, \theta_2)$, $i = 0,1,2,\ldots$ must be positive and periodic in the range $0 \le \varphi \le \pi/2$, $0 \le \theta_1 \le 2\pi$ and $0 \le \theta_1 \le 2\pi$.

3.1. Zeroth-order perturbation

The zeroth-order perturbation equation is first equation of system (17)

$$\frac{1}{2}\sigma^2 \frac{\partial^2 T_0}{\partial \xi^2} - \alpha\xi \frac{\partial T_0}{\partial \xi} + \omega_1 \frac{\partial T_0}{\partial \theta_1} + \omega_2 \frac{\partial T_0}{\partial \theta_2} = \Lambda_0(p)\, T_0 . \tag{18}$$

Since the momnet Lyapunov exponent $\Lambda(p) = 0$ passes through the origin, i.e.

$$\Lambda(0) = \Lambda_0(0) + \varepsilon\Lambda_1(0) + \varepsilon^2\Lambda_2(0) + \cdots + \varepsilon^n\Lambda_n(0) = 0 , \tag{19}$$

one obtain $\Lambda_j(0) = 0$, j=0, 1, 2, … Because the left side of equation (18) does not depend on p, $\Lambda_0(0) = 0$ implies $\Lambda_0(p) = 0$. Applying the method of separation of variables and letting

$$T_0(\xi, \varphi, \theta_1, \theta_2) = \psi_0(\varphi) H_1(\theta_1) H_2(\theta_2) Z_0(\xi). \tag{20}$$

Eq. (18) becomes

$$\frac{\sigma^2}{2Z_0}\frac{d^2 Z_0}{d\xi^2} - \frac{\alpha\xi}{Z_0}\frac{dZ_0}{d\xi} + \frac{\omega_1}{H_1}\frac{dH_1}{d\theta_1} + \frac{\omega_2}{H_2}\frac{dH_2}{d\theta_2} = 0 , \tag{20}$$

and will be satisfied only if

$$\frac{\omega_1}{H_1}\frac{dH_1}{d\theta_1} = a_1 , \ \frac{\omega_2}{H_2}\frac{dH_2}{d\theta_2} = a_2 , \ \frac{\sigma^2}{2Z_0}\frac{d^2 Z_0}{d\xi^2} - \frac{\alpha\xi}{Z_0}\frac{dZ_0}{d\xi} = -(a_1 + a_2), \tag{21}$$

where are a_1 and a_2 constants. Solutions of previous systems are

$$H_1(\theta_1) = C_1 e^{\frac{a_1}{\omega_1}\theta_1} , \ H_2(\theta_2) = C_2 e^{\frac{a_2}{\omega_2}\theta_2} , \ Z_0(\xi) = C_3 \int e^{\frac{\alpha}{\sigma^2}\xi^2} d\xi + C_4 . \tag{22}$$

For $T_0(\xi, \varphi, \theta_1, \theta_2)$ to be periodic function of period 2π, constants must be $a_1 = 0$, $a_2 = 0$ and $C_3 = 0$. Without reducing the generality, we adopt that the integration constants $C_1 = 1$, $C_2 = 1$, $C_4 = 1$. Finally, the solution of zeroth-perturbation is

$$\Lambda_0(p) = 0 , T_0(\xi, \varphi, \theta_1, \theta_2) = \psi_0(\varphi). \tag{23}$$

where $\psi_0(\varphi)$ is a function to be determined.
The associated adjoint differential equation of (18) is

$$\frac{1}{2}\sigma^2 \frac{\partial^2 T_0^*}{\partial \xi^2} + \alpha\xi \frac{\partial T_0^*}{\partial \xi} + \alpha T_0^* - \omega_1 \frac{\partial T_0^*}{\partial \theta_1} - \omega_2 \frac{\partial T_0^*}{\partial \theta_2} = 0 . \tag{24}$$

Employing the method of separation of vearibles with

$$T_0^*(\xi,\varphi,\theta_1,\theta_2)=\psi_0^*(\varphi)H_1^*(\theta_1)H_2^*(\theta_2)Z_0^*(\xi), \tag{25}$$

it is easy to show that

$$H_1^*=H_2^*=\frac{1}{2\pi},\ Z_0^*=\frac{1}{\sqrt{2\pi}\sigma_\xi}\exp\left(-\frac{\xi^2}{2\sigma_\xi^2}\right), \tag{26}$$

i.e. the Ornstein-Uhlenbeck process $\xi(t)$ is a normally distributed random variable with mean $\mu_\xi=0$ and standard deviation $\sigma_\xi=\sigma/\sqrt{2\alpha}$. Finally, the solution of (24) is

$$T_0^*(\xi,\varphi,\theta_1,\theta_2)=\frac{1}{4\pi^2}\psi_0^*(\varphi)Z_0^*(\xi), \tag{27}$$

where $\psi_0^*(\varphi)$ is a function to be determined.

3.2. First-order perturbation

Since $\Lambda_0(p)=0$, the first-order perturbation becomes

$$L_0T_1+L_1T_0=\Lambda_1(p)T_0. \tag{28}$$

Form the Fredholm Alternative, for previous equation to have nontrivila solutions, it is required that

$$\left(L_0T_1,T_0^*\right)=\left(\Lambda_1(p)\psi_0-s_1\frac{d\psi_0}{d\varphi}-q_1\psi_0,T_0^*\right)=0, \tag{29}$$

where $(f.g)$ denotes the inner product

$$(f,g)=\int_0^{\pi/2}\int_{-\infty}^{+\infty}\int_0^{2\pi}\int_0^{2\pi}f(\xi,\varphi,\theta_1,\theta_2)g(\xi,\varphi,\theta_1,\theta_2)\,d\theta_1d\theta_2d\xi d\varphi. \tag{30}$$

Both $s_1(\xi,\varphi,\theta_1,\theta_2)$ i $g_1(\xi,\varphi,\theta_1,\theta_2)$ are linear function of ξ, it is required that

$$\left(s_1\frac{d\psi_0}{d\varphi}+q_1\psi_0,T_0^*\right)=0. \tag{31}$$

Equation (29) can be satisfied only if

$$\Lambda_1(p)=0. \tag{32}$$

Now, equation (28) becomes

$$L_0T_1=\xi\left[-s_{10}(\varphi,\theta_1,\theta_2)\frac{d\psi_0(\varphi)}{d\varphi}-q_{10}(\varphi,\theta_1,\theta_2)\psi_0(\varphi)\right]. \tag{33}$$

The solution of the previous equation we can determine on the form

$$T_1(\xi,\varphi,\theta_1,\theta_2)=\xi\left[S_1(\varphi,\theta_1,\theta_2)\frac{d\psi_0(\varphi)}{d\varphi}+Q_1(\varphi,\theta_1,\theta_2)\psi_0(\varphi)\right], \tag{34}$$

where, according to the author of [9], $S_1(\varphi,\theta_1,\theta_2)$ and $Q_1(\varphi,\theta_1,\theta_2)$ are

$$\begin{aligned} S_1(\varphi,\theta_1,\theta_2)&=-\int_0^s s_{10}(\varphi,\psi+\omega_1 r,\psi+\omega_2 r)e^{-\alpha(r-s)}dr,\\ Q_1(\varphi,\theta_1,\theta_2)&=-\int_0^s q_{10}(\varphi,\psi+\omega_1 r,\psi+\omega_2 r)e^{-\alpha(r-s)}dr. \end{aligned} \tag{35}$$

Finally, function $T_1(\xi,\varphi,\theta_1,\theta_2)$ is

$$\begin{aligned} T_1(\xi,\varphi,\theta_1,\theta_2)=\xi(t)f_{11}\psi_0+f_{12}\frac{d\psi_0}{d\varphi}+\xi(t)\left[f_{13}\psi_0+f_{14}\frac{d\psi_0}{d\varphi}\right]\cos 2\varphi\\ +\xi(t)\left[f_{15}\psi_0+f_{16}\frac{d\psi_0}{d\varphi}\right]\sin 2\varphi \end{aligned} \tag{36}$$

where $f_{1i}=f_{1i}(\theta_1,\theta_2)$, $i=1,2...6$ are function on the form

$$\begin{aligned} &f_{11}(\theta_1,\theta_2)=-\frac{p\,p_{11}}{4K_1}J_1-\frac{p\,p_{22}}{4K_2}J_2,\quad f_{12}(\theta_1,\theta_2)=\frac{p_{12}+p_{21}}{4K_M}J_M+\frac{p_{12}-p_{21}}{4K_P}J_P,\\ &f_{13}(\theta_1,\theta_2)=-p\,f_{16}(\theta_1,\theta_2),\quad f_{14}(\theta_1,\theta_2)=-\frac{p_{12}-p_{21}}{4K_M}J_M-\frac{p_{12}+p_{21}}{4K_P}J_P,\\ &f_{15}(\theta_1,\theta_2)=p\,f_{14}(\theta_1,\theta_2),\quad f_{16}(\theta_1,\theta_2)=\frac{p_{11}}{4K_1}J_1-\frac{p_{22}}{4K_2}J_2. \end{aligned} \tag{37}$$

In the previous equation we introduced the following marking

$$\begin{aligned} &K_1=\alpha^2+(2\omega_1)^2,\ K_2=\alpha^2+(2\omega_2)^2,\\ &K_M=\alpha^2+(\omega_1-\omega_2)^2,\ K_P=\alpha^2+(\omega_1+\omega_2)^2.\\ &J_1=2\omega_1\cos 2\theta_1+\alpha\sin 2\theta_1,\quad J_2=2\omega_2\cos 2\theta_2+\alpha\sin 2\theta_2,\\ &J_M=(\omega_1-\omega_2)\cos(\theta_1-\theta_2)+\alpha\sin(\theta_1-\theta_2),\\ &J_P=(\omega_1+\omega_2)\cos(\theta_1+\theta_2)+\alpha\sin(\theta_1+\theta_2). \end{aligned} \tag{38}$$

3.3. Second-order perturbation

With respect to Eqs. (23) and (32), the second-order perturbation becomes

$$L_0T_2+L_1T_1+L_2T_0=\Lambda_2(p)T_0. \tag{39}$$

Form the Fredholm Alternative, for previous equation to have nontrivial solutions, it is required that

$$\left(L_0\, T_2, T_0^*\right)=\left(\Lambda_2(p)\,\psi_0 - L_1\, T_1 - L_2\,\psi_0, T_0^*\right)=0\ . \tag{40}$$

After integration by θ_1, θ_2 i ξ, the previous equation has the form

$$\int_0^{\pi/2}\left[-R_2\frac{d^2\psi_0(\varphi)}{d\varphi^2}-R_1\frac{d\psi_0(\varphi)}{d\varphi}+\left(\Lambda_2(p)-R_0\right)\psi_0(\varphi)\right]\psi_0^*(\varphi)d\varphi=0\ . \tag{41}$$

Where the function $R_0(\varphi,\theta_1,\theta_2)$, $R_1(\varphi,\theta_1,\theta_2)$ i $R_2(\varphi,\theta_1,\theta_2)$ given by the expressions

$$R_0(\varphi,\theta_1,\theta_2)=-\frac{p}{2}\left(\beta_1+\beta_2\right)+\frac{p}{128}\left[\left(10+3p\right)P_1+\left(6+p\right)\left(P_3+P_6\right)\right]$$
$$+\left[-\frac{p}{2}\left(\beta_1-\beta_2\right)+\frac{p(p+2)P_2}{32}-\frac{p}{16}\left(P_5+P_6\right)\right]\cos 2\varphi+\frac{p(p-2)}{128}\left[P_1-P_3-P_6\right]\cos 4\varphi,$$

$$R_1(\varphi,\theta_1,\theta_2)=\left[\frac{1}{2}\left(\beta_1-\beta_2\right)-\frac{(p+2)P_2}{32}-\frac{(p-1)\left(P_5+P_6\right)}{32}\right]\sin 2\varphi-\frac{(p-1)\left(P_1-P_5-P_6\right)}{64}\sin 4\varphi$$
$$-\frac{1}{32}\left[\left(p_{12}^2\,\mathrm{tg}\varphi-p_{21}^2\cot\varphi\right)-\left(p_{12}^2\,\mathrm{tg}\varphi+p_{21}^2\cot\varphi\right)\cos 2\varphi\right]\left[S(\omega_1+\omega_2)+S(\omega_1-\omega_2)\right],$$

$$R_2(\varphi,\theta_1,\theta_2)=\frac{P_1+2P_3+3P_4+P_5}{128}-\frac{P_3+P_4}{32}\cos 2\varphi-\frac{P_1-P_3-P_6}{128}\cos 4\varphi\,, \tag{42}$$

with the constants given by

$$\begin{aligned}
&P_1=p_{11}^2S(2\omega_1)+p_{22}^2S(2\omega_2),\ P_2=p_{11}^2S(2\omega_1)-p_{22}^2S(2\omega_2),\\
&P_3=\left(p_{12}+p_{21}\right)^2S(\omega_1+\omega_2),\ P_4=\left(p_{12}+p_{21}\right)^2S(\omega_1-\omega_2),\\
&P_5=\left(p_{12}-p_{21}\right)^2S(\omega_1+\omega_2),\ P_6=\left(p_{12}-p_{21}\right)^2S(\omega_1-\omega_2).
\end{aligned} \tag{43}$$

How Eq. (41) must be satisfied for arbitrary function $\psi_0^*(\varphi)$, this leads to the following differential equation for $\psi_0(\varphi)$

$$\overline{L}[\psi_0]=0, \tag{44}$$

where

$$\overline{L}[\psi_0]=R_2\frac{d^2\psi_0(\varphi)}{d\varphi^2}+R_1\frac{d\psi_0(\varphi)}{d\varphi}-\left(\Lambda_2(p)-R_0\right)\psi_0(\varphi). \tag{45}$$

As in Wedig [8], the solution of Eq. (44) can be calculated from an orthogonal expansion, where may assume ψ_0 as a Fourier cosine series [10]. Thus, inserting

$$\psi_0(\varphi)=\sum_{k=0}^{N}K_{2k}\cos 2k\varphi\ . \tag{46}$$

When N tends to infinity, the solution (46) of equations tends to the exact solution. The existence of a nontrivial solution for K_{2k} requires that the determinant of the coefficient of matrice

$$K_{mn} = \begin{bmatrix} a_{00} & a_{01} & a_{02} & a_{03} & \dots \\ a_{10} & a_{11} & a_{12} & a_{13} & \dots \\ a_{20} & a_{21} & a_{22} & a_{23} & \dots \\ a_{30} & a_{31} & a_{32} & a_{33} & \dots \\ \dots & \dots & \dots & \dots & \dots \end{bmatrix}, \tag{47}$$

equals zero, where

$$a_{mn} = \int_0^{\pi/2} \bar{L}[\cos(2m\varphi)]\cos(2n\varphi)d\varphi, \text{ (m, n=0,1 2, 3, ... N)}, \tag{48}$$

Assuming a solution for the function of $\psi_0(\varphi)$ to take only the first member of the cosine series, i.e. K_0, the conditions of existence nontrivial solution $a_{00} = 0$ gives us the solution of $\Lambda_2(p)$ in the form

$$\Lambda_2(p) = -\frac{p}{2}(\beta_1 + \beta_2) + \frac{p(10+3p)}{128}P_1 + \frac{p(6+p)}{128}(P_3 + P_6). \tag{49}$$

When $\alpha = \sigma \to \infty$, the Ornstein-Uhlenbeck process $\xi(t)$ approaches $\dot{W}(t)$, where $\dot{W}(t)$ denotes formally a unit Gaussian white-noise process. In this case, the spectral density of stochastic proces is constant

$$S(2\omega_1) = S(2\omega_2) = S(\omega_1 + \omega_2) = S(\omega_1 - \omega_2) = \sigma^2, \tag{50}$$

and, from Eq. (49), one obtains the moment Lyapunov exponent in the form

$$\Lambda_1(p) = -\frac{p}{2}(\beta_1 + \beta_2) + \frac{p(10+3p)\sigma^2}{128}(p_{11}^2 + p_{22}^2) + \frac{p(6+p)\sigma^2}{64}(p_{12}^2 + p_{21}^2), \tag{51}$$

obtained by Janevski at all. [11].
Assuming a solution for the function of $\psi_0(\varphi)$ in the form

$$\psi_0(\varphi) = K_0 + K_2 \cos 2\varphi, \tag{52}$$

we can determine moment Lyapunov exponent $\Lambda_2(p)$ in form

$$\begin{aligned} \Lambda_2(p) = &-\frac{p}{2}(\beta_1 + \beta_2) + \left(\frac{13p^2}{512} + \frac{21p}{256} - \frac{1}{64}\right)P_1 \\ &+ \left(\frac{3p^2}{512} + \frac{11p}{256} - \frac{3}{64}\right)(P_3 + P_6) - \frac{1}{16}(P_4 + P_5) + \sqrt{D_2(p)}, \end{aligned} \tag{53}$$

where

$$
\begin{aligned}
D_2(p) = {} & \frac{(p+4)^2(p-2)^2}{2^{18}}P_1^2 + \frac{p(p+2)^3}{2^{11}}P_2^2 + \frac{\left(p^2+2p+24\right)^2}{2^{18}}\left(P_3+P_6\right)^2 + \frac{1}{2^8}\left(P_4+P_5\right)^2 \\
& - \frac{p}{2^9}\left(P_3P_5 + 2\sqrt{P_3P_5P_4P_6} + P_4P_6\right) - \frac{(p+4)(p-2)\left(p^2+2p+24\right)}{2^{17}}P_1\left(P_3+P_6\right) \\
& - \frac{(p+4)(p-2)}{2^{12}}P_1\left(P_4+P_5\right) + \frac{\left(p^2+2p+24\right)}{2^{12}}\left(P_3P_4 + P_3P_5 + P_4P_6 + P_5P_6\right) \\
& - \frac{p(p+2)^2}{2^6}P_2(\beta_1-\beta_2) + \frac{p(p+1)}{2^6}\left(\sqrt{P_3P_5} + \sqrt{P_4P_6}\right)(\beta_1-\beta_2) + \frac{p(p+2)}{2^3}(\beta_1-\beta_2)^2.
\end{aligned}
\tag{54}
$$

4. Application to a thin-walled beam subjected to eccentric stochastic axial load

The purpose of this section is to present the general results of the above sections in the context of real engineering applications and show how these results can be applied to physical problems. To this end, we consider the flexural-torsinal vibration stability of a homogeneous, isotropic, thin waled beam with two planes of summetry which is subjected to eccentric axial load (Fig.1.a) where R is eccentricity. By transferring the eccentric load to the plane of symmetry of the cross-section of the beam, an axial load and a couple are obtained which are shown in Fig. 1.b.

a.

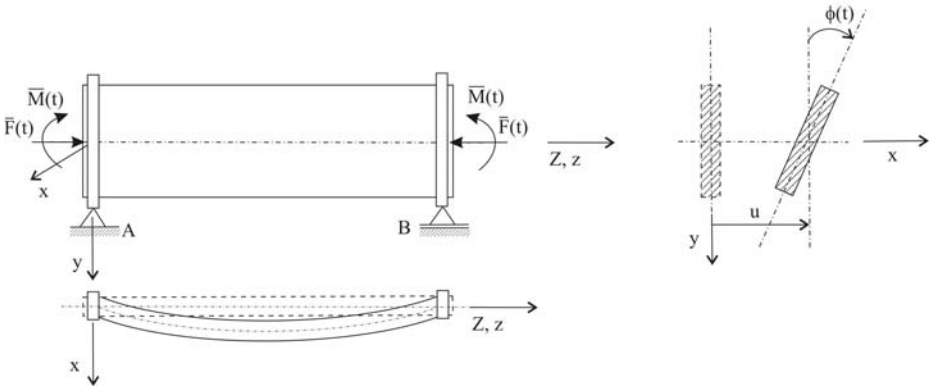

b.

Fig. 1 Geometry of a thin-walled beam system

The governing differential equations for the coupled flexural and torsional motion of the beam can be written as (Pavlović et al. [7])

$$\begin{aligned}
&\rho A\frac{\partial^2 U}{\partial T^2}+\alpha_u\frac{\partial U}{\partial t}+EI_y\frac{\partial^4 U}{\partial Z^4}+\overline{M}(T)\frac{\partial^2\phi}{\partial Z^2}+\overline{F}(T)\frac{\partial^2 U}{\partial Z^2}=0,\\
&\rho I_p\frac{\partial^2\phi}{\partial T^2}+\alpha_\phi\frac{\partial\phi}{\partial T}-\left(GJ-\overline{F}(t)\frac{I_p}{A}\right)\frac{\partial^2\phi}{\partial Z^2}+\overline{M}(T)\frac{\partial^2 U}{\partial Z^2}+EI_s\frac{\partial^4\phi}{\partial Z^4}=0,
\end{aligned} \tag{55}$$

where U is the flexural displacement in the x-direction, ϕ is torsional displacement, ρ is mass density, A is area of the cross-section of beam, I_y, I_p, I_S are axial, polar and sectorial moment of inertia, J is Saint–Venant torsional constant, E is Young modulus of elasticity, G is shear modulus, α_U, α_ϕ are viscous damping coefficients, T is time and Z is axial coordinate. Using the following transformations

$$\begin{aligned}
&U=u\sqrt{\frac{I_p}{A}},\ Z=zl,\quad R=rl,\quad T=k_t t,\quad \overline{M}(T)=R\overline{F}(T),\\
&\overline{F}(T)=F_{cr}F(t),\quad F_{cr}=\frac{\pi^2 EI_y}{l^2},\quad k_t^2=\frac{\rho A l^4}{EI_y},\quad e=\frac{AI_s}{I_y I_p},\\
&\varepsilon^2\beta_1=\frac{1}{2}\alpha_U\frac{l^2}{\sqrt{\rho AEI_y}},\quad \varepsilon^2\beta_2=\frac{1}{2}\alpha_\phi l^2\sqrt{\frac{A}{\rho EI_y I_p^2}},\\
&S_1=\frac{l^2 r^2 A}{I_p},\quad S_2=\frac{GJAl^2}{\pi^2 EI_y I_p},
\end{aligned} \tag{56}$$

where *l* is the length of the beam, F_{cr} is Euler critical force for the simply supported narrow rectangular beam, S_1 and S_2 are slenderness parameters, β_1 and β_2 are reduced viscous damping coefficients, we get governing equations as

$$\begin{aligned}
&\frac{\partial^2 u}{\partial t^2}+2\varepsilon^2\beta_1\frac{\partial u}{\partial t}+\frac{\partial^4 u}{\partial z^4}+\pi^2\sqrt{S_1}F(t)\frac{\partial^2\phi}{\partial z^2}+\pi^2 F(T)\frac{\partial^2 u}{\partial z^2}=0,\\
&\frac{\partial^2\phi}{\partial t^2}+2\varepsilon^2\beta_2\frac{\partial\phi}{\partial T}-\pi^2\left(S_2-F(t)\right)\frac{\partial^2\phi}{\partial z^2}+\pi^2\sqrt{S_1}F(t)\frac{\partial^2 u}{\partial z^2}+e\frac{\partial^4\phi}{\partial z^4}=0.
\end{aligned} \tag{57}$$

Taking free warping displacement and zero angular displacements into account, boundary conditions for the simply supported beam are

$$\begin{aligned}
&u(t,0)=u(t,1)=\left.\frac{\partial^2 u}{\partial z^2}\right|_{(t,0)}=\left.\frac{\partial^2 u}{\partial z^2}\right|_{(t,1)}=0,\\
&\phi(t,0)=\phi(t,1)=\left.\frac{\partial^2\phi}{\partial z^2}\right|_{(t,0)}=\left.\frac{\partial^2\phi}{\partial z^2}\right|_{(t,1)}=0.
\end{aligned} \tag{58}$$

Consider the shape function $\sin(\pi z)$ which satisfies the boundary conditions for the first mode vibration, the displacement $u(t.z)$ and twist angle $\phi(t,z)$ can be described by

$$u(t,z) = q_1(t)\sin\pi z\,,\quad \phi(t,z) = \psi_1(t)\sin\pi z\,. \tag{59}$$

Substituting $u(t,z)$ and $\phi(t,z)$ from (59) into the equations of motion (57) and employing Galerkin method unknown time functions can be expressed as

$$\begin{aligned} &\ddot{u}_1 + \omega_1^2 u_1 + 2\beta_1\varepsilon^2\,\dot{u}_1 - \varepsilon\left[K_{11}u_1 + K_{12}\psi_1\right]F(t) = 0,\\ &\ddot{\psi}_1 + \omega_2^2\psi_1 + 2\beta_2\varepsilon^2\,\dot{\psi}_1 - \varepsilon\left[K_{21}u_1 + K_{22}\psi_1\right]F(t) = 0\,. \end{aligned} \tag{60}$$

If we define the expressions

$$\omega_1^2 = \pi^4\,,\ \omega_2^2 = \pi^4\left(S_2 + e\right),\ \ K_{11} = K_{22} = \pi^4\,,\ K_{12} = K_{21} = \pi^4\sqrt{S_1}\,, \tag{61}$$

and assume that the compressive axial force is stochastic processes (4) with small intensity

$$F(t) = \varepsilon\xi(t)\,, \tag{62}$$

then Eq. (57) is reduced to Eq. (3).
Using the above result for the moment Lyapunov exponent

$$\Lambda(p) = \varepsilon^2\Lambda_2(p) + O(\varepsilon^3)\,, \tag{63}$$

with the definition of the moment stability $\Lambda(p) < 0$, we determine analytically (the case where N = 0, $\Lambda_2(p)$ is shown with Eq.(49)) the *p*th moment stability boundary of the oscillatory system in the second-order perturbation

$$\begin{aligned} \beta > {}& \frac{10+3p}{128}\pi^4\left[S(2\omega_1) + \frac{1}{S_2+e}S(2\omega_2)\right]\\ &+ \frac{6+p}{128}\frac{\pi^4 S_1}{S_2+e}\left[\left(1+\sqrt{S_2+e}\right)^2 S(\omega_1+\omega_2) + \left(1-\sqrt{S_2+e}\right)^2 S(\omega_1-\omega_2)\right], \end{aligned} \tag{64}$$

where, for the sake of simplicity, we assume, in previous equation and in what follows, that two viscous damping coefficients are equal

$$\beta_1 = \beta_2 = \beta \tag{65}$$

It is known that the oscillatory system (60) is asymptotically stable only if the Lyapunov exponent $\lambda < 0$. Then expression

$$\lambda = \varepsilon^2\lambda_2 + O(\varepsilon^3)\,, \tag{66}$$

is employed to determine the almost-sure stability boundary of the oscillatory system in the first-order perturbation (the case where N = 0)

$$\begin{aligned} \beta > {}& \frac{5}{64}\pi^4\left[S(2\omega_1) + \frac{1}{S_2+e}S(2\omega_2)\right]\\ &+ \frac{3}{64}\frac{\pi^4 S_1}{S_2+e}\left[\left(1+\sqrt{S_2+e}\right)^2 S(\omega_1+\omega_2) + \left(1-\sqrt{S_2+e}\right)^2 S(\omega_1-\omega_2)\right]. \end{aligned} \tag{67}$$

For the case where N = 1 ($\Lambda_2(p)$ is shown with Eq.(53)), the *p*th moment stability boundary of the oscillatory system in the second-order perturbation is expressed by

$$\beta > \frac{13p^2+42p-8}{512p}\pi^4\left[S(2\omega_1)+\frac{1}{S_2+e}S(2\omega_2)\right]$$
$$+\frac{3p^2+11p-24}{512p}\frac{\pi^4 S_1}{S_2+e}\left[\left(1+\sqrt{S_2+e}\right)^2 S(\omega_1+\omega_2)+\left(1-\sqrt{S_2+e}\right)^2 S(\omega_1-\omega_2)\right] \qquad (68)$$
$$-\frac{1}{p}\frac{\pi^4 S_1}{S_2+e}\left[\left(1+\sqrt{S_2+e}\right)^2 S(\omega_1-\omega_2)+\left(1-\sqrt{S_2+e}\right)^2 S(\omega_1+\omega_2)\right]+\frac{1}{p}\sqrt{D_2(p)},$$

and the almost-sure stability boundary is expressed by, when $\lambda < 0$,

$$\beta > \frac{21}{256}\pi^4\left[S(2\omega_1)+\frac{1}{S_2+e}S(2\omega_2)\right]$$
$$+\frac{11}{256}\frac{\pi^4 S_1}{S_2+e}\left[\left(1+\sqrt{S_2+e}\right)^2 S(\omega_1+\omega_2)+\left(1-\sqrt{S_2+e}\right)^2 S(\omega_1-\omega_2)\right], \qquad (69)$$
$$-\frac{1}{16}\frac{\pi^4 S_1}{S_2+e}\left[\left(1+\sqrt{S_2+e}\right)^2 S(\omega_1-\omega_2)+\left(1-\sqrt{S_2+e}\right)^2 S(\omega_1+\omega_2)\right]+\frac{1}{2\sqrt{D_2(0)}}\left.\frac{dD_2(p)}{dp}\right|_{p=0}.$$

5. Numerical results and conclusions

Inequalities (64) and (69) give the possibility to obtain almost-sure stability regions for thin-walled beams. Also, by using expressions (67) and (68), we can determine the *p*th moment stability regions. Numerical results are calculated for steel beams with elastic constant ratio $E/G \approx 2.59$ and two types of cross sections: I-section and narrow rectangular cross section.

With respect to standard I-section, we can approximately take $h/b \approx 2$, $b/\delta_1 \approx 11$, where h is the depth, b is the width, d is the thickness of the flanges and δ_1 is the thickness of the rib of I-section. These ratios yield $S_1 \approx 6(R/h)^2$ $S_2 \approx 0.01928(l/h)^2$ and $e \equiv 1.276$. For the thin-walled cross section, according to assumption $\delta/h < 0.1$, $S_1 \approx 12(R/h)^2$, $S_2 \approx 0.01928(l/h)^2$ and $e \equiv 0$, using the approximation $1+(\delta/h)^2 \approx 1$. All examples in this paper were presented to the values of small parameter $\varepsilon = 0.1$ and the relative eccentricity $r = 0.02$.

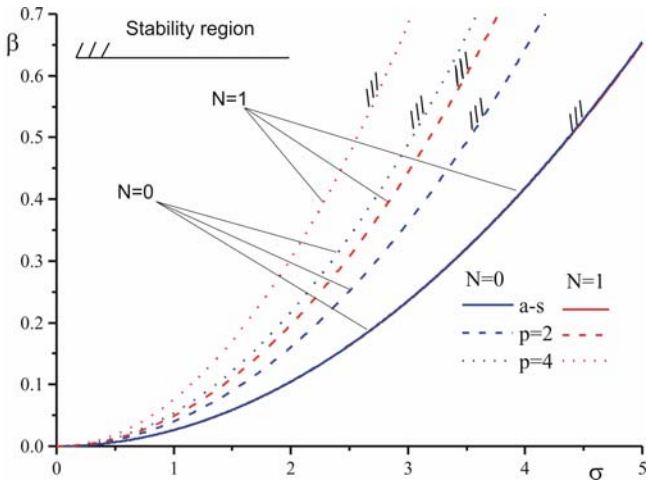

Fig. 2 Stability regions for standard I-section

Fig.2 shows the almost-sure and *p*th moment stability boundaries with respect to the damping coefficient β and the intensity of random process σ for the standard I-section. The figure shows the stability boundaries for when this function is assumed in the form of Fourier cosine series (46) taking the first one or two members. Almost sure stability boundaries coincide, while the stability limit for the values p = 2 and p = 4 is slightly different, with stricter criteria for the case N = 1. This is not true in the case of rectangular plates (Fig 3.), when the criteria for the case N =1 is a lot tighter, and not taking another member of the line (46) can lead to erroneous conclusions.

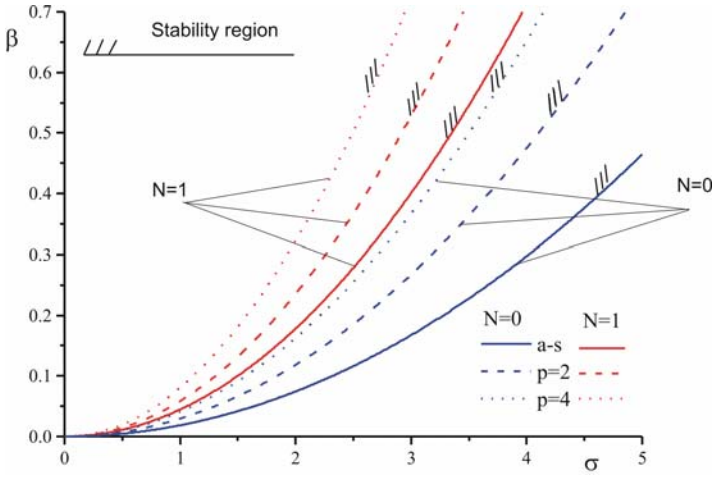

Fig. 3 Stability regions for the narrow rectangular cross section

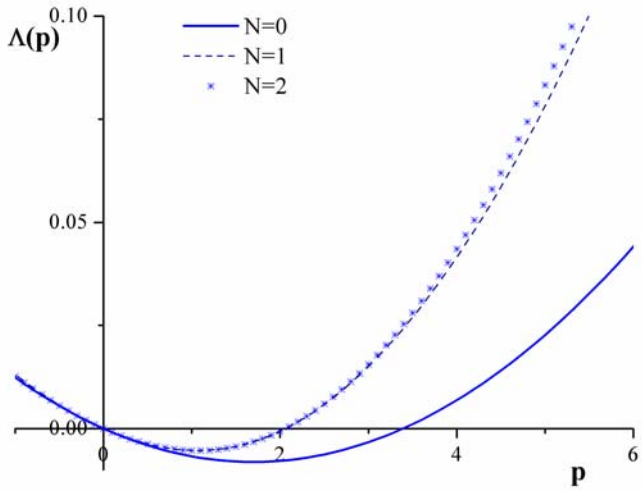

Fig. 4 Moment Lyapunov exponent $\Lambda(p)$ for standard I-section

Typical results of the moment Lyapunov exponents $\Lambda(p)$ for system (55) in the second perturbation are shown in Fig. 4 for I-section and Fig. 5 for rectangular cross section. Both views are presented for values of damping coefficient $\beta = 0.2$ and characteristic of stochastic process $\sigma = 2$ and $\alpha = 5$. The moment Lyapunov exponents are shown for the case N = 0, 1 and 2, for when we take the three members of the order (46). It is observed that the discrepancies exist between the curves for case N=0 (does not depend on the φ) and the cases when function T_0 depend on φ (N=1 and 2).

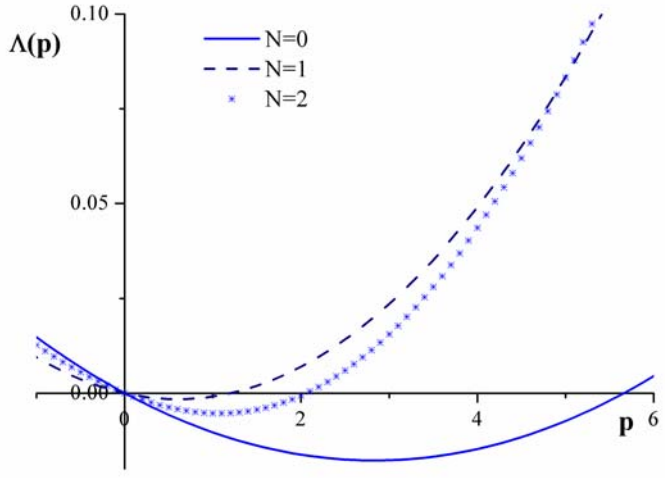

Fig. 5 Moment Lyapunov exponent $\Lambda(p)$ for the narrow rectangular cross section

Further increase of N number of members does not make sense, because the curves merge into one. Generally speaking, function ψ_0 should assume the form (46), where the satisfying accuracy is achieved by getting the first two members.

Acknowledgement. Research supported by Ministry of Science and Environment Protection of Republic Serbia, grant N_0 ON 174011.

References

[1] Arnold L, Doyle M M and N Sri Namachchivaya N (1997) Small noise expansion of moment Lyapunov exponents for two-dimensional systems, *Dynamics and Stability of Systems,* **12 (3)**, pp.187-211.
[2] Khasminskii R and Moshchuk N (1998) Moment Lyapunov exponent and stability index for linear conservative system with small random perturbation, *SIAM Journal of Applied Mathematics*, **58 (1)**, pp.245-256.
[3] Sri Namachchivaya N, Van Roessel H J and Talwar S (1994) Maximal Lyapunov exponent and almost-sure stability for coupled two-degree of freedom stochastic systems, *ASME Journal of Applied Mechanics*, **61**, pp.446-452.
[4] Sri Namachchivaya N and Van Roessel H J (2004) Stochastic stability of coupled oscillators in resonance: A perturbation approach, *ASME Journal of Applied Mechanics*, **71**, pp.759-767.
[5] Kozić P, Janevski G and Pavlović R (2009) Moment Lyapunov exponents and stochastic stability for two coupled oscillators, *The Journal of Mechanics of Materials and Structures*, **4 (10)**, pp.1689-1701.
[6] Kozić P, Janevski G and Pavlović R (2010) Moment Lyapunov exponents and stochastic stability of a double-beam system under compressive axial load, *International Journal of Solid and Structures*, **47(10)**, pp.1435-1442.
[7] Pavlović R, Kozić P, Rajković P and Pavlović I (2007) Dynamic Stability of a Thin-walled Beam Subjected to Axial Loads and end Moments, *Journal of Sound and Vibration*, **301**, 690-700
[8] Wedig W (1988) Lyapunov exponent of stochastic systems and related bifurcation problems, *Stochastic Structural Dynamics – Progress in Theory and Applications, Elsevier Applied Science*, Ariaratnam T S, Schuëller G I and Elishakoff I (Eds.), pp. 315 – 327.
[9] Xie W –C (2001) Moment Lyapunov exponents of a two-dimensional system under real-noise excitation. *Journal of Sound and Vibration*, **239(1)**, pp.139-155
[10] Sri Namachchivaya N and Van Roessel H J (2001) Moment Lyapunov exponent and stochastic stability of two coupled oscillators driven by real noise, *ASME Journal of Applied Mechanics*, **68**, pp.903-914.
[11] Janevski G, Kozić P and Pavlović R, **In Press**, Moment Lyapunov exponent and stochastic stability of a thin-walled beam subjected to eccentric axial load, Journal of Theoretical and Applied Mechanics, ISSN 1429-2955.

ON ENTROPY FLUX OF ANISOTROPIC ELASTIC BODIES

J. P. Jarić[1], **R. Vignjević**[2], **Z. DJ. Golubović**[3], **D. S. Kuzmanović**[4]

[1] The University of Belgrade, Faculty of Mathematics, Jagićeva 16, 11000 Beograd, Serbia
e-mail: jovojaric@yahoo.com
[2] Applied Mechanics Department, School of Engineering, Cranfield University, Cranfield, Bedford, MK43 OAL, UK
e-mail: v.rade@cranfield.ac.uk
[3] The University of Belgrade, Faculty of Mechanical Engineering, Kraljice Marije 16, 11120 Belgrade 35
e-mail: zogol@eunet.rs
[4]The University of Belgrade, Faculty of Transport and Traffic Engineering, Vojvode Stepe 305, 11000 Belgrade
e-mail: d.kuzmanovic@sf.bg.ac.rs

Abstract. In this paper the consequences of the assumption that $\Lambda^{\varepsilon} = \Lambda^{\varepsilon}(\theta)$ (irrespective of whether the classical entropy flux relation is valid or not) are investigated. We consider it as a sufficient condition in order to derive the entropy flux – heat flux relation for all isotropic materials as well as for some crystal classes including transverse isotropy, orthotropy, triclinic systems and rhombic systems. Under this assumption first the entropy flux and heat flux relation for viscoelastic materials, isotropic elastic materials, transversely isotropic elastic bodies and transversely isotropic rigid heat conductors examined by I. Müller and I-Shih Liu is reexamined. In addition all crystal classes given in [14], for which representations of anisotropic functions with respect to the symmetry groups of these crystal classes can be expressed in terms of isotropic functions, are considered. For all of them the entropy flux and heat flux relation is derived explicitly. The procedure is very general in the sense that the constitutive relations used here are non linear. Particularly, it appears that all crystal elastic bodies, examined here, are hyperelastic which is a generalization of I-Shih Liu conclusion for the transversely isotropic bodies he examined.

Also, the entropy flux and heat flux relations were derived for the all crystal classes when considering them as rigid conductors.

1. Introduction

One of the important problems in thermodynamics is the relationship between the entropy flux and the heat flux for phenomena far from equilibrium.

The entropy principle based on the Clausius-Duhem inequlity in the spacial description is

$$\rho\dot{\eta} + \operatorname{div}\frac{\mathbf{q}}{\theta} - \rho\frac{r}{\theta} \geq 0, \tag{1}$$

where ρ is the masss density, θ is the temperature, η is the specific entropy density, $\mathbf{q}$ the heat flux and r the heat supply; by $\dot{()}$ and "div" the time derivative and divergence operator are denoted, respectively. It has been widely adopted in the development of modern rational thermodynamics, after the fundamental work of Coleman and Noll [1]. The main assumptions, motivated by the result of classical thermostatics, are that the entropy flux $\mathbf{\Phi}$

and the entropy supply s are proportional to the heat flux and the heat supply, respectively. Moreover, both constants of proportionality are assumed to be the reciprocal of the absolute temperature., i.e.

$$\mathbf{\Phi}_\kappa = \frac{1}{\theta}\mathbf{q}_\kappa, \qquad s = \frac{1}{\theta}r. \tag{2}$$

These main assumptions, while tacit in the classical theory of continuum mechanics, are not particularly well motivated for materials in general. In fact, it is known that they are inconsistent with the kinetic theory of ideal gases, and are also found to be inappropriate to account for the thermodynamics of diffusion.

There is an alternative approach to the formulation of the second law of thermodynamics which has been extended and applied to nonequilibrium thermodynamics by J. Serrin [2] and Šilhavy [3] and summarized by C. Truesdell and S. Bharatha [4]. See also Muschik [5]

One of the extension of this inequality has been proposed by I. Müller [6], [7]. It is usually called the entropy inequality and seems to be the most general formulation of the continuous second law of thermodynamics which has been proposed so far. In this theory, Müller [8] abandon the assumptions, given in (2), by treating the entropy flux $\mathbf{\Phi}$ and the heat flux vector $\mathbf{q}$ as independent constitutive quantities and hence leaving the entropy inequality in its general form

$$\rho\dot{\eta} + \mathrm{div}\mathbf{\Phi} - \rho s \geq 0. \tag{3}$$

Making use of this inequality Müller [7] first proved that for viscous heat-conducting fluids and isotropic thermoelastic bodies [6], the entropy flux is proportional to the heat flux with the coefficient, called the coldness, depending only on the empirical temperature.

Further, I-Shih Liu proposed in [9] a method of exploitating the inequality (3) which is of the classical method of Lagrange multipliers in mechanics. Instead of this inequality restricting the solution of field equations he consider solutions of an extended inequality which should hold for all fields. This can be done if one consider the field equations as constraints on solutions of the energy inequality.

Recently Liu [10] analyzed the thermodynamics theory of viscoelastic bodies and proved that for isotropic viscoelastic materials, the results are identical to the classical results $(2)_1$. In the same paper, he also proved that the body is hyperelastic as *a consequence of the Lagrange multiplier* $\Lambda^\varepsilon = \Lambda(\theta)$*, irrespective of whether the classical entropy flux relation is valid or not*.

However, for anisotropic elastic materials in general, the validity of the classical entropy flux relation is yet to be explored.

The first contribution in this direction has been given very recently by Liu [11]. It is proved by considering transversely isotropic elastic bodies that the classical entropy flux relation $(2)_1$ need not be valid in general. The same conclusion also holds for transversely isotropic rigid heat conductors [12].

In this paper we explore the functional dependence of *the Lagrange multiplier* $\Lambda^\varepsilon = \Lambda(\theta)$, *irrespective of whether the classical entropy flux relation is valid or not* in general. The consequence of this enable us to derive the entropy flux and heat flux relations for some crystal classes including *transverse isotropy, orthotropy, triclinic systems, monoclinic systems and rhombic systems*.

2. The entropy principle

Here we present the basic idea of the entropy principle proposed by Müller and I-Shih Liu for viscoelastic materials. We state the balance laws of mass, linear momentum and energy

$$\begin{aligned} &\dot{\rho} + \rho \mathrm{div}\dot{\mathbf{x}} = 0, \\ &\rho\ddot{\mathbf{x}} - \mathrm{div}\mathbf{T} = \rho\mathbf{b}, \\ &\rho\dot{\varepsilon} + \mathrm{div}\mathbf{q} - \mathbf{T}\cdot \mathrm{grad}\dot{\mathbf{x}} = \rho r, \end{aligned} \tag{4}$$

where $\mathbf{x}$ is the spacial position material particle X, $\mathbf{T}$ is Cauchy stress tensor and ε is the specific internal energy density; the external supplies $\mathbf{b}$ and r are given.

Note that for solid bodies it is more convenient to use a referential description. Also since constitutive relations do not depend on external supplies, in exploiting thermodynamic restrictions it suffices to consider only supply-free bodies. Then we have the following balance laws

$$\begin{aligned} &\rho = J^{-1}\rho_{\kappa}, \\ &\rho_{\kappa}\ddot{\mathbf{x}} - \mathrm{Div}\mathbf{T}_{\kappa} = \mathbf{0}, \\ &\rho_{\kappa}\dot{\varepsilon} + \mathrm{Div}\mathbf{q}_{\kappa} - \mathbf{T}_{\kappa}\cdot\dot{\mathbf{F}} = 0, \end{aligned} \tag{5}$$

and the entropy inequality

$$\rho_{\kappa}\dot{\eta} + \mathrm{Div}\boldsymbol{\Phi}_{\kappa} \geq 0. \tag{6}$$

Here the first Piola-Kirchhoff stress tensor $\mathbf{T}_{\kappa}$, the material heat flux vector $\mathbf{q}_{\kappa}$ and the material entropy flux vector $\boldsymbol{\Phi}_{\kappa}$ are related to the Cauchy stress tensor $\mathbf{T}$, the heat flux vector $\mathbf{q}$ and the entropy flux vector $\boldsymbol{\Phi}$ by

$$\mathbf{T}_{\kappa} = J\mathbf{T}\mathbf{F}^{-T}, \quad \mathbf{q}_{\kappa} = J\mathbf{F}^{-1}\mathbf{q}, \quad \boldsymbol{\Phi}_{\kappa} = J\mathbf{F}^{-1}\boldsymbol{\Phi}, \tag{7}$$

where $\mathbf{F} = \nabla\mathbf{x}$ is the deformation gradient in referential coordinates and $J = |\det\mathbf{F}|$. "Div" is the divergence operator with respect to the referential coordinates.

It has been shown that the entropy principle imposes severe restrictions on constitutive functions and the exploitation of such restrictions based on the Clausius Duehem inequality are relatively easy. For elastic materials, in general, the thermodynamic restrictions can be easily obtained by the well-known Coleman-Noll procedure [1].

On the other hand, the exploitation of the entropy principle based on the general entropy inequality for a supply free body, first considered by Müller [6], [7], was much more difficult and later the procedure, based on the use of Lagrange multipliers, has been improved greatly by Liu [9]. The derivation of the relation between the entropy flux and the heat flux, referred to simply as *entropy flux relation*, is a typical problem in this new theory. The problem usually relies on the isotropic properties of material bodies with the use of either explicit isotropic representations or the flux relation theorems for isotropic vector functions given in [13].

Here we outline the analysis for isotropic viscoelastic materials with isotropic elasticity as a special case. The constitutive relations for viscoelastic materials can be written as functions of the state variables

$$\left(\mathbf{F}, \dot{\mathbf{F}}, \theta, \mathbf{g}_{\kappa}\right), \tag{8}$$

i.e.

$$\begin{aligned}
\mathbf{T}_\kappa &= \hat{\mathbf{T}}_\kappa\left(\mathbf{F}, \dot{\mathbf{F}}, \theta, \mathbf{g}_\kappa\right), \\
\mathbf{q}_\kappa &= \hat{\mathbf{q}}_\kappa\left(\mathbf{F}, \dot{\mathbf{F}}, \theta, \mathbf{g}_\kappa\right), \\
\varepsilon &= \hat{\varepsilon}\left(\mathbf{F}, \dot{\mathbf{F}}, \theta, \mathbf{g}_\kappa\right), \\
\eta &= \hat{\eta}\left(\mathbf{F}, \dot{\mathbf{F}}, \theta, \mathbf{g}_\kappa\right), \\
\mathbf{\Phi}_\kappa &= \hat{\mathbf{\Phi}}_\kappa\left(\mathbf{F}, \dot{\mathbf{F}}, \theta, \mathbf{g}_\kappa\right),
\end{aligned} \tag{9}$$

where $\mathbf{g}_\kappa = \nabla\theta$, θ is regarded as an *empirical* temperature, which is some convenient measure of the hotness (or the coldness) of the thermodynamic state. For the purpose of determining the constitutive restrictions, the regularities of constitutive functions as well as the state variables are usually assumed to be as smooth as the contexts requires. Note that the density field $\rho(\mathbf{X}, t)$ is completely determined by the motion $\mathbf{x}(\mathbf{X}, t)$ and the density $\rho_\kappa(\mathbf{X})$ in the reference configuration. Therefore the thermodynamic process is define as the solution

$$\{\mathbf{x}(\mathbf{X}, t), \theta(\mathbf{X}, t)\} \tag{10}$$

of the field equations by introducing the constitutive relations for $\mathbf{T}_\kappa$, $\mathbf{q}_\kappa$, and ε into the balance laws of the linear momentum and energy.

To find the restrictions imposed on constitutive functions by the entropy principle is one of the major objectives in modern continuum thermodynamics.

I-Shih Liu has proposed in [9], a method of exploitation of the inequality (3) in a way which reminds the classical method of Lagrange multipliers in mechanics. Namely, instead of this inequality restricting the solution of field equations he proposed that solutions of an extended inequality which should hold for all fields. This can be done if we consider field equations as constrains on solutions of the energy inequality.

2.1. Method of Lagrange multipliers

According to Müller and I-Shih Liu, there exist Lagrange multipliers Λ^v and Λ^ε, depending on the state variables, such that the inequality

$$\rho_\kappa\dot{\eta} + \mathrm{Div}\mathbf{\Phi}_\kappa - \mathbf{\Lambda}^{\mathbf{v}}\cdot\left(\rho_\kappa\ddot{\mathbf{x}} - \mathrm{Div}\mathbf{T}_\kappa\right) - \Lambda^\varepsilon\left(\rho_\kappa\dot{\varepsilon} + \mathrm{Div}\mathbf{q}_\kappa - \mathbf{T}_\kappa\cdot\dot{\mathbf{F}}\right) \geq 0 \tag{11}$$

is valid under no constraints, i.e. valid for any field $\mathbf{x}(\mathbf{X}, t)$, $\theta(\mathbf{X}, t)$.

In addition to this we invoke the condition of material objectivity, which implies the following reduced constitutive equations for viscoelastic materials

$$\begin{aligned}
\mathbf{T}_\kappa &= \hat{\mathbf{T}}_\kappa\left(\mathbf{C}, \dot{\mathbf{C}}, \theta, \mathbf{g}_\kappa\right), \\
\mathbf{q}_\kappa &= \hat{\mathbf{q}}_\kappa\left(\mathbf{C}, \dot{\mathbf{C}}, \theta, \mathbf{g}_\kappa\right), \\
\varepsilon &= \hat{\varepsilon}\left(\mathbf{C}, \dot{\mathbf{C}}, \theta, \mathbf{g}_\kappa\right), \\
\eta &= \hat{\eta}\left(\mathbf{C}, \dot{\mathbf{C}}, \theta, \mathbf{g}_\kappa\right), \\
\mathbf{\Phi}_\kappa &= \hat{\mathbf{\Phi}}_\kappa\left(\mathbf{C}, \dot{\mathbf{C}}, \theta, \mathbf{g}_\kappa\right),
\end{aligned} \tag{12}$$

where $\mathbf{C} = \mathbf{F}^T\mathbf{F}$ is the right Cauchy-Green tensor.

Since the inequality (11) must hold for any $\mathbf{x}(\mathbf{X}, t)$, $\theta(\mathbf{X}, t)$, the values of $\left\{\theta, \mathbf{g}_\kappa, \mathbf{C}, \dot{\mathbf{C}}\right\}$ and $\left\{\dot{\theta}, \ddot{\mathbf{x}}, \dot{\mathbf{g}}_\kappa, \ddot{\mathbf{C}}, \nabla\mathbf{g}_\kappa, \nabla\mathbf{C}, \nabla\dot{\mathbf{C}}\right\}$ in (11) can be arbitrary given at any point and any instant.

First of all, from (11) we note that it is linear with respect $\ddot{\mathbf{x}}$. Also the coefficient of $\ddot{\mathbf{x}}$ is $\rho_\kappa \mathbf{\Lambda}^{\mathbf{v}}$ and therefore we conclude that

$$\mathbf{\Lambda}^{\mathbf{v}} = 0. \tag{13}$$

Thus (11) becomes

$$\rho_\kappa (\dot{\eta} - \Lambda^\varepsilon \dot{\varepsilon}) + \mathrm{Div}\mathbf{\Phi}_\kappa - \Lambda^\varepsilon \mathrm{Div}\mathbf{q}_\kappa + \Lambda^\varepsilon \mathbf{T}_\kappa \cdot \dot{\mathbf{F}} \geq 0. \tag{14}$$

Next, we write

$$\dot{\eta} - \Lambda^\varepsilon \dot{\varepsilon} = \left(\frac{\partial \eta}{\partial \theta} - \Lambda^\varepsilon \frac{\partial \varepsilon}{\partial \theta} \right) \dot{\theta} + \left(\frac{\partial \eta}{\partial \mathbf{g}_\kappa} - \Lambda^\varepsilon \frac{\partial \varepsilon}{\partial \mathbf{g}_\kappa} \right) \cdot \mathbf{g}_\kappa +$$
$$+ \left(\frac{\partial \eta}{\partial \mathbf{C}} - \Lambda^\varepsilon \frac{\partial \varepsilon}{\partial \mathbf{C}} \right) \cdot \dot{\mathbf{C}} + \left(\frac{\partial \eta}{\partial \dot{\mathbf{C}}} - \Lambda^\varepsilon \frac{\partial \varepsilon}{\partial \dot{\mathbf{C}}} \right) \cdot \ddot{\mathbf{C}},$$

$$\mathrm{Div}\mathbf{\Phi}_\kappa - \Lambda^\varepsilon \mathrm{Div}\mathbf{q}_\kappa = \left(\frac{\partial \mathbf{\Phi}_\kappa}{\partial \theta} - \Lambda^\varepsilon \frac{\partial \mathbf{q}_\kappa}{\partial \theta} \right) \cdot \mathbf{g}_\kappa + \left(\frac{\partial \mathbf{\Phi}_\kappa}{\partial \mathbf{g}_\kappa} - \Lambda^\varepsilon \frac{\partial \mathbf{q}_\kappa}{\partial \mathbf{g}_\kappa} \right) \cdot \nabla \mathbf{g}_\kappa +$$
$$+ \left(\frac{\partial \mathbf{\Phi}_\kappa}{\partial \mathbf{C}} - \Lambda^\varepsilon \frac{\partial \mathbf{q}_\kappa}{\partial \mathbf{C}} \right) \cdot \nabla \mathbf{C} + \left(\frac{\partial \mathbf{\Phi}_\kappa}{\partial \dot{\mathbf{C}}} - \Lambda^\varepsilon \frac{\partial \mathbf{q}_\kappa}{\partial \dot{\mathbf{C}}} \right) \cdot \nabla \dot{\mathbf{C}}.$$

Note that

$$\left(\frac{\partial \mathbf{\Phi}_\kappa}{\partial \mathbf{g}_\kappa} - \Lambda^\varepsilon \frac{\partial \mathbf{q}_\kappa}{\partial \mathbf{g}_\kappa} \right) \cdot \nabla \mathbf{g}_\kappa \tag{15}$$

in component form this reads as

$$\left(\frac{\partial \mathbf{\Phi}_\kappa}{\partial \mathbf{g}_\kappa} - \Lambda^\varepsilon \frac{\partial \mathbf{q}_\kappa}{\partial \mathbf{g}_\kappa} \right) \cdot \nabla \mathbf{g}_\kappa = \left(\frac{\partial \Phi_{\kappa K}}{\partial \theta_{,L}} - \Lambda^\varepsilon \frac{\partial q_{\kappa K}}{\partial \theta_{,L}} \right) \theta_{,LK} \tag{16}$$

The same rule holds for the other terms in the above expression.

Substituting these expressions into (14), by inspection, we conclude that this inequality is also linear with respect to the following derivatives

$$\left\{ \dot{\theta}, \ddot{\mathbf{x}}, \dot{\mathbf{g}}_\kappa, \ddot{\mathbf{C}}, \nabla \mathbf{g}_\kappa, \nabla \mathbf{C}, \nabla \dot{\mathbf{C}} \right\}.$$

As the inequality must hold for all fields we have eliminated the constraints imposed by the field equations. The coefficients of the above derivatives have to vanish identically. Otherwise we could choose the fields in such a way that one negative term would dominate all others and the inequality would be violated. Hence we obtain

$$\begin{aligned} &\mathbf{\Lambda}^{\mathbf{v}} = 0, \\ &\frac{\partial \eta}{\partial \theta} - \Lambda^\varepsilon \frac{\partial \varepsilon}{\partial \theta} = 0, \\ &\frac{\partial \eta}{\partial \mathbf{g}_\kappa} - \Lambda^\varepsilon \frac{\partial \varepsilon}{\partial \mathbf{g}_\kappa} = 0, \\ &\frac{\partial \eta}{\partial \dot{\mathbf{C}}} - \Lambda^\varepsilon \frac{\partial \varepsilon}{\partial \dot{\mathbf{C}}} = 0. \end{aligned} \tag{17}$$

$$\left(\frac{\partial \mathbf{\Phi}_\kappa}{\partial \mathbf{g}_\kappa} - \Lambda^\varepsilon \frac{\partial \mathbf{q}_\kappa}{\partial \mathbf{g}_\kappa} \right)_{sym} = 0,$$

$$\frac{\partial \mathbf{\Phi}_\kappa}{\partial \mathbf{C}} - \Lambda^\varepsilon \frac{\partial \mathbf{q}_\kappa}{\partial \mathbf{C}} = 0, \tag{18}$$
$$\frac{\partial \mathbf{\Phi}_\kappa}{\partial \dot{\mathbf{C}}} - \Lambda^\varepsilon \frac{\partial \mathbf{q}_\kappa}{\partial \dot{\mathbf{C}}} = 0.$$

Then the entropy inequality reduces to

$$\left(\frac{\partial \mathbf{\Phi}_\kappa}{\partial \theta} - \Lambda^\varepsilon \frac{\partial \mathbf{q}_\kappa}{\partial \theta}\right) \cdot \mathbf{g}_\kappa + \rho_\kappa \left(\frac{\partial \eta}{\partial \mathbf{C}} - \Lambda^\varepsilon \frac{\partial \varepsilon}{\partial \mathbf{C}}\right) \cdot \dot{\mathbf{C}} + \Lambda^\varepsilon \mathbf{T}_\kappa \cdot \dot{\mathbf{F}} \geq 0. \tag{19}$$

Making use of second Piola-Kirchhoff tensor $\mathbf{S}_\kappa = \mathbf{F}^{-1}\mathbf{T}_\kappa = J\mathbf{F}^{-1}\mathbf{T}\mathbf{F}^{-T}$, which is a symmetric tensor, and $\dot{\mathbf{C}} = \dot{\mathbf{F}}^T\mathbf{F} + \mathbf{F}^T\dot{\mathbf{F}} = 2\left(\dot{\mathbf{F}}^T\mathbf{F}\right)_{sym}$, the inequality (19) can be written in more compact form as

$$\sigma = \left(\frac{\partial \mathbf{\Phi}_\kappa}{\partial \theta} - \Lambda^\varepsilon \frac{\partial \mathbf{q}_\kappa}{\partial \theta}\right) \cdot \mathbf{g}_\kappa + \rho_\kappa \left(\frac{\partial \eta}{\partial \mathbf{C}} - \Lambda^\varepsilon \frac{\partial \varepsilon}{\partial \mathbf{C}} + \frac{1}{2\rho_\kappa}\Lambda^\varepsilon \mathbf{S}_\kappa\right) \cdot \dot{\mathbf{C}} \geq 0. \tag{20}$$

Moreover, from (17) we obtain

$$\mathrm{d}\eta = \Lambda^\varepsilon \,\mathrm{d}\varepsilon + \left(\frac{\partial \eta}{\partial \mathbf{C}} - \Lambda^\varepsilon \frac{\partial \varepsilon}{\partial \mathbf{C}}\right) \cdot \mathrm{d}\mathbf{C} \tag{21}$$

which is in the form of the thermostatic Gibbs relation.

3. Entropy flux relation for viscoelastic materials

For further evaluation of the consequences of the entropy principle, particularly in connection with relations (18), we invoke the material symmetry condition that has to be satisfied by $\{\varepsilon, \mathbf{T}_\kappa, \mathbf{q}_\kappa, \mathbf{\Phi}_\kappa, \eta\}$ for isotropic viscoelastic bodies. For instance, heat flux can be expressed as

$$\hat{\mathbf{q}}_\kappa\left(\mathbf{Q}\mathbf{C}\mathbf{Q}^T, \mathbf{Q}\dot{\mathbf{C}}\mathbf{Q}^T, \theta, \mathbf{Q}\mathbf{g}_\kappa\right) = \mathbf{Q}\hat{\mathbf{q}}_\kappa\left(\mathbf{C}, \dot{\mathbf{C}}, \theta, \mathbf{g}_\kappa\right), \quad \forall \mathbf{Q} \in O, \tag{22}$$

where O is the full orthogonal group. Thus $\hat{\mathbf{q}}_\kappa$ is an isotropic vector-valued function of and therefore is restricted in its dependence on the independent variables $\left(\mathbf{C}, \dot{\mathbf{C}}, \theta, \mathbf{g}_\kappa\right)$.

After lengthy calculation, from (18), Liu proved that Λ^ε must be independent of $\mathbf{C}$, $\dot{\mathbf{C}}$ and $\mathbf{g}_\kappa$. Thus

$$\Lambda^\varepsilon = \Lambda^\varepsilon(\theta). \tag{23}$$

Accordingly (21) becomes

$$\mathrm{d}\eta = \Lambda^\varepsilon \,\mathrm{d}\varepsilon + \frac{\partial \eta}{\partial \mathbf{C}}\left(\eta - \Lambda^\varepsilon \varepsilon\right) \cdot \mathrm{d}\mathbf{C}, \tag{24}$$

or

$$\mathrm{d}\eta = \Lambda^\varepsilon \left(\mathrm{d}\varepsilon - \frac{\partial \psi}{\partial \mathbf{C}} \cdot \mathrm{d}\mathbf{C}\right), \tag{25}$$

where

$$\psi = \varepsilon - \frac{1}{\Lambda^\varepsilon}\eta. \tag{26}$$

By comparison with the classical Gibbs relation in thermostatics, the function Λ^ε can be identify as the reciprocal of the absolute temperature θ, i.e.

$$\Lambda^\varepsilon = \frac{1}{\theta}. \tag{27}$$

Moreover, the following entropy flux relation

$$\mathbf{\Phi}_\kappa = \frac{1}{\theta}\mathbf{q}_\kappa \tag{28}$$

is valid.

Following the Müller-Liu procedure for viscoelastic bodies, given above, one can easily see that for isotropic elastic materials with state variables $(\mathbf{F}, \theta, \mathbf{g}_\kappa)$, the relation (27) holds.

3.1. Entropy flux of anisotropic elastic materials

We now come to the problem of the derivation of the relation between the entropy flux and the heat flux for anisotropic materials with state variables $(\mathbf{F}, \theta, \mathbf{g}_\kappa)$. The following relations have to be satisfied

$$\begin{aligned} &\frac{\partial \eta}{\partial \theta} - \Lambda^\varepsilon \frac{\partial \varepsilon}{\partial \theta} \quad = 0, \\ &\frac{\partial \eta}{\partial \mathbf{g}_\kappa} - \Lambda^\varepsilon \frac{\partial \varepsilon}{\partial \mathbf{g}_\kappa} = 0, \end{aligned} \tag{29}$$

$$\begin{aligned} &\left(\frac{\partial \mathbf{\Phi}_\kappa}{\partial \mathbf{g}_\kappa} - \Lambda^\varepsilon \frac{\partial \mathbf{q}_\kappa}{\partial \mathbf{g}_\kappa}\right)_{sym} = 0, \\ &\frac{\partial \mathbf{\Phi}_\kappa}{\partial \mathbf{C}} - \Lambda^\varepsilon \frac{\partial \mathbf{q}_\kappa}{\partial \mathbf{C}} = 0, \end{aligned} \tag{30}$$

At this stage we come to the problem of the material symmetry condition that has to be satisfied by $\{\varepsilon, \mathbf{T}_\kappa, \mathbf{q}_\kappa, \mathbf{\Phi}_\kappa, \eta\}$ for anisotropic elastic bodies.

The first paper dealing this problem, in fact for transversely isotropic elastic bodies, was published by Liu in [11], which relies on his paper [14]. The main result of this paper is based on the fact that many anisotropic materials possesses structures which can be characterized by certain directions, lines or planes, specifically, by some unit vectors $\mathbf{m}_1, \ldots, \mathbf{m}_a$ and some tensors $\mathbf{M}_1, \ldots, \mathbf{M}_b$. Let g be the group which preserves these characteristics, i.e.

$$g = \left\{\mathbf{Q} \in G; \quad \mathbf{Q}\mathfrak{m} = \mathfrak{m}, \quad \mathbf{Q}\mathfrak{M}\mathbf{Q}^T = \mathfrak{M}\right\}, \tag{31}$$

where G is a subgroup of O. Here we use the following abbreviations

$$\begin{aligned} \mathfrak{m} &= (\mathbf{m}_1, \ldots, \mathbf{m}_a), \\ \mathfrak{M} &= (\mathbf{M}_1, \ldots, \mathbf{M}_b). \end{aligned} \tag{32}$$

In other words g is characterized by the set $(\mathfrak{m}, \mathfrak{M})$ and the group $G \in O$, i.e.

$$g = (G; \mathfrak{m}, \mathfrak{M}). \tag{33}$$

Theorem. *A function $f(\mathbf{v}, \mathbf{A})$ is invariant to g if and only if it can be represent by*

$$f(\mathbf{v}, \mathbf{A}) = \hat{f}(\mathbf{v}, \mathbf{A}, \mathfrak{m}, \mathfrak{M}), \tag{34}$$

where $\hat{f}(\mathbf{v}, \mathbf{A}, \mathfrak{m}, \mathfrak{M})$ is invariant relative to G.

Here $\mathbf{v}$ is vector, $\mathbf{A}$ is tensor of second order and f stands for either scalar-valued, vector-valued or tensor valued.

Particularly, if $\hat{f}(\mathbf{v}, \mathbf{A}, \mathfrak{m}, \mathfrak{M})$ is isotropic function then:

for scalar-valued function

$$\hat{f}(\mathbf{Qv}, \mathbf{QAQ}^T, \mathbf{Q}\mathfrak{m}, \mathbf{Q}\mathfrak{M}\mathbf{Q}^T) = \hat{f}(\mathbf{v}, \mathbf{A}, \mathfrak{m}, \mathfrak{M}), \tag{35}$$

for vector-valued function

$$\mathbf{Q}\hat{f}(\mathbf{v}, \mathbf{A}, \mathfrak{m}, \mathfrak{M}) = \hat{f}(\mathbf{Qv}, \mathbf{QAQ}^T, \mathbf{Q}\mathfrak{m}, \mathbf{Q}\mathfrak{M}\mathbf{Q}^T), \tag{36}$$

tensor-valued function

$$\mathbf{Q}\hat{f}(\mathbf{v}, \mathbf{A}, \mathfrak{m}, \mathfrak{M})\mathbf{Q}^T = \hat{f}(\mathbf{Qv}, \mathbf{QAQ}^T, \mathbf{Q}\mathfrak{m}, \mathbf{Q}\mathfrak{M}\mathbf{Q}^T). \tag{37}$$

In the same paper Liu gives a list of 14 such groups g for some crystal classes.

In order to write the exact form of constitutive functions we used in further investigation we need several functional relations, particularly, among orthonormal vectors $\mathbf{n}_i$ and $\mathbf{N}_i$, i.e.

$$\mathbf{n}_i \cdot \mathbf{n}_j = \delta_{ij}. \tag{38}$$

and skew-symmetric tensors defined by

$$\mathbf{N}_i = e_{ijk}\mathbf{n}_j \otimes \mathbf{n}_k, \quad i,j,k = 1,2,3, \tag{39}$$

These basic relations are given in Appendix.

Liu [11] considered only two different classes of transversally isotropic bodies

$$g_2 = (O; \mathbf{Qn}_1 = \mathbf{n}_1),$$
$$g_5 = \left(O; \mathbf{Qn}_1 \otimes \mathbf{n}_1\mathbf{Q}^T = \mathbf{n}_1 \otimes \mathbf{n}_1\right),$$

where $\mathbf{n}_1$ is the preferred direction of transverse isotropy.

In applying the isotropic representation of constitutive functions he used the Green-St. Venant strain tensor $\mathbf{E}$, i.e.

$$\mathbf{E} = \frac{1}{2}(\mathbf{C} - \mathbf{I}) \tag{40}$$

which vanishes when there is no deformation, and considers constitutive functions $\mathbf{q}_\kappa$ and $\mathbf{\Phi}_\kappa$ of $(\mathbf{E}, \theta, \mathbf{g}_\kappa)$ up to bilinear terms in $\mathbf{E}$ and $\mathbf{g}_\kappa$, i.e.

$$\begin{aligned}
\mathbf{q}_\kappa &= (a_1 + a_2\mathrm{tr}\mathbf{E} + a_3\mathbf{n}\cdot\mathbf{En})\,\mathbf{g}_\kappa + a_4\mathbf{E}\,\mathbf{g}_\kappa + \\
&+ (b_1 + b_2\mathrm{tr}\mathbf{E} + b_3\mathbf{n}\cdot\mathbf{En})\,(\mathbf{n}\otimes\mathbf{n})\mathbf{g}_\kappa + b_4(\mathbf{n}\otimes\mathbf{En})\mathbf{g}_\kappa + b_5(\mathbf{En}\otimes\mathbf{n})\mathbf{g}_\kappa + \\
&+ (c_1 + c_2\mathrm{tr}\mathbf{E} + c_3\mathbf{n}\cdot\mathbf{En})\,\mathbf{n} + c_4\mathbf{En}, \\
\mathbf{\Phi}_\kappa &= (\alpha_1 + \alpha_2\mathrm{tr}\mathbf{E} + \alpha_3\mathbf{n}\cdot\mathbf{En})\,\mathbf{g}_\kappa + \alpha_4\mathbf{E}\,\mathbf{g}_\kappa + \\
&+ (\beta_1 + \beta_2\mathrm{tr}\mathbf{E} + \beta_3\mathbf{n}\cdot\mathbf{En})\,(\mathbf{n}\otimes\mathbf{n})\mathbf{g}_\kappa + \beta_4(\mathbf{n}\otimes\mathbf{En})\mathbf{g}_\kappa + \beta_5(\mathbf{En}\otimes\mathbf{n})\mathbf{g}_\kappa + \\
&+ (\gamma_1 + \gamma_2\mathrm{tr}\mathbf{E} + \gamma_3\mathbf{n}\cdot\mathbf{En})\,\mathbf{n} + \gamma_4\mathbf{En},
\end{aligned}$$

where all the material coefficients are functions of temperature θ only.

For the class of transversally isotropic bodies defined by

$$g_2 = (O; \mathbf{Qn}_1 = \mathbf{n}_1), \tag{41}$$

he was able to prove that Λ^ε is a function of temperature only, i.e.

$$\Lambda^\varepsilon = \Lambda^\varepsilon(\theta) = \frac{1}{\theta}, \tag{42}$$

as well as the entropy flux and the heat flux relation

$$\mathbf{\Phi}_\kappa = \frac{1}{\theta}\mathbf{q}_\kappa + k(\theta)\mathbf{n}_1. \tag{43}$$

Therefore, for this class of transversally isotropic bodies the classical result does not hold, in general.

For the class of transversally isotropic bodies defined by

$$g_5 = \left(O; \mathbf{Q}\mathbf{n}_1 \otimes \mathbf{n}_1\mathbf{Q}^T = \mathbf{n}_1 \otimes \mathbf{n}_1\right), \tag{44}$$

he also obtained

$$\Lambda^{\varepsilon} = \frac{1}{\theta}, \qquad \mathbf{\Phi}_{\kappa} = \frac{1}{\theta}\mathbf{q}_{\kappa}, \tag{45}$$

the classical results.

In all these cases we had first to find a functional forme of Λ^{ε} in order to determine the relation between entropy flux and heat flux. It appears that $\Lambda^{\varepsilon} = \Lambda^{\varepsilon}(\theta)$ holds in all these cases, i.e. $\Lambda^{\varepsilon} = \Lambda^{\varepsilon}(\theta)$ is necessary condition for the determination of relation between entropy flux and heat flux. We pose the question whether is it also sufficient condition? Having this in mind we proceed first by reexamining the above cases.

This assumption differs substantially from Green & Laws [18], as well as from Hutter [19] and Bargmann & Steinmann [20] postulates. In Green & Laws [18] the entropy flux and heat flux relation is defined as $\mathbf{\Phi}_{\kappa} = \frac{1}{\varphi}\mathbf{q}_{\kappa}$, where φ is a constitutive function which reduces to the absolute temperature θ in equilibrium. Hutter [19] postulated the classical entropy flux and heat flux relation. In their contribution Bargmann & Steinmann [20] adopted the Green & Naghdi approach for non-classical theory of thermoelasticity for isotropic materials and in order to obtain the entropy flux and heat flux relation, even in this case, made use of some mathematical assumptions.

This is also in accordance with Eringen's statement [22] that "it is always possible to express the entropy influx and entropy source as

$$\mathbf{\Phi} = \frac{1}{\theta}\mathbf{q} + \mathbf{\Phi}_1 \tag{46}$$

where $\mathbf{\Phi}_1$ is the entropy influx due to all other effects except heat input."

4. The consequence of the assumption that $\Lambda^{\varepsilon} = \Lambda^{\varepsilon}(\theta)$

Under this assumption we first reconsider isotropic viscoelastic bodies and transversally isotropic material bodies.

4.1. Isotropic viscoelastic bodies

The starting point is the set of equations (18)

$$\begin{aligned} \left(\frac{\partial \mathbf{\Phi}_{\kappa}}{\partial \mathbf{g}_{\kappa}} - \Lambda^{\varepsilon}\frac{\partial \mathbf{q}_{\kappa}}{\partial \mathbf{g}_{\kappa}}\right)_{sym} &= 0, \\ \frac{\partial \mathbf{\Phi}_{\kappa}}{\partial \mathbf{C}} - \Lambda^{\varepsilon}\frac{\partial \mathbf{q}_{\kappa}}{\partial \mathbf{C}} &= 0, \\ \frac{\partial \mathbf{\Phi}_{\kappa}}{\partial \dot{\mathbf{C}}} - \Lambda^{\varepsilon}\frac{\partial \mathbf{q}_{\kappa}}{\partial \dot{\mathbf{C}}} &= 0. \end{aligned} \tag{47}$$

Let

$$\mathbf{k} = \mathbf{\Phi}_{\kappa} - \Lambda^{\varepsilon}\mathbf{q}_{\kappa}. \tag{48}$$

Generally,

$$\mathbf{k} = \hat{\mathbf{k}}(\mathbf{C}, \dot{\mathbf{C}}, \theta, \mathbf{g}_\kappa). \tag{49}$$

Then (18) can be written as

$$\begin{aligned} \left(\frac{\partial \mathbf{k}}{\partial \mathbf{g}_\kappa}\right)_{sym} &= \mathbf{0}, \\ \frac{\partial \mathbf{k}}{\partial \mathbf{C}} &= \mathbf{0}, \\ \frac{\partial \mathbf{k}}{\partial \dot{\mathbf{C}}} &= \mathbf{0}. \end{aligned} \tag{50}$$

Thus $\mathbf{k} = \hat{\mathbf{k}}(\theta, \mathbf{g}_\kappa)$ must satisfy

$$\left(\frac{\partial \mathbf{k}}{\partial \mathbf{g}_\kappa}\right)_{sym} = \mathbf{0}. \tag{51}$$

For the moment we shall write it in componential form, i.e.

$$\frac{\partial k_i}{\partial g_j} + \frac{\partial k_j}{\partial g_i} = 0, \tag{52}$$

where k_i and g_i are components of $\mathbf{k}$ and $\mathbf{g}_\kappa$, respectively.

By differentiation we obtain

$$\frac{\partial^2 k_p}{\partial g_r \partial g_q} + \frac{\partial^2 k_q}{\partial g_r \partial g_p} = 0. \tag{53}$$

The other two relations

$$\begin{aligned} \frac{\partial^2 k_q}{\partial g_p \partial g_r} + \frac{\partial^2 k_r}{\partial g_p \partial g_q} &= 0, \\ \frac{\partial^2 k_r}{\partial g_q \partial g_p} + \frac{\partial^2 k_p}{\partial g_q \partial g_r} &= 0, \end{aligned}$$

are obtained by cyclic permutation. From them we have

$$\frac{\partial^2 k_p}{\partial g_r \partial g_q} = 0. \tag{54}$$

The solution of this simple set of differential equations is

$$k_p = A_{pq}(\theta) g_q + a_p(\theta), \qquad A_{(pq)} = 0. \tag{55}$$

We shall write it as

$$\mathbf{k}(\theta, \mathbf{g}_\kappa) = \mathbf{A}(\theta)\mathbf{g}_\kappa + \mathbf{a}(\theta), \tag{56}$$

where $\mathbf{A}(\theta)$ is skew symmetric.

Since we are dealing with isotropic viscoelastic bodies $\mathbf{k}(\theta, \mathbf{g}_\kappa)$ must be vector-valued isotropic function. Thus

$$\mathbf{Q}\mathbf{k}(\theta, \mathbf{g}_\kappa) = \mathbf{k}(\theta, \mathbf{Q}\mathbf{g}_\kappa) \tag{57}$$

must hold for every $\mathbf{Q} \in O$ and every $\mathbf{g}_\kappa$. Equivalently,

$$\mathbf{Q}\mathbf{A}(\theta)\mathbf{g}_\kappa + \mathbf{Q}\mathbf{a}(\theta) = \mathbf{A}(\theta)\mathbf{Q}\mathbf{g}_\kappa + \mathbf{a}(\theta). \tag{58}$$

Particularly for $\mathbf{Q} = -\mathbf{I}$ we have

$$\mathbf{a}(\theta) = \mathbf{0}. \tag{59}$$

Then

$$\mathbf{Q}\mathbf{A}(\theta)\mathbf{g}_\kappa = \mathbf{A}(\theta)\mathbf{Q}\mathbf{g}_\kappa. \tag{60}$$

We write it as

$$\mathbf{Q}\mathbf{A}(\theta)\mathbf{Q}^T\mathbf{Q}\mathbf{g}_\kappa = \mathbf{A}(\theta)\mathbf{Q}\mathbf{g}_\kappa. \tag{61}$$

Since this must hold for every $\mathbf{Q} \in O$ and every $\mathbf{g}_\kappa$ we have that

$$\mathbf{Q}\mathbf{A}(\theta)\mathbf{Q}^T = \mathbf{A}(\theta) \tag{62}$$

from which we have $\mathbf{A}(\theta) = \mathfrak{h}(\theta)\mathbf{I}$. Thus $\mathfrak{h}(\theta) = 0$ since $\mathbf{A}(\theta)$ is skew symmetric. Hence $\mathbf{A}(\theta) = \mathbf{0}$ and

$$\mathbf{k} = \mathbf{\Phi}_\kappa - \Lambda^\varepsilon \mathbf{q}_\kappa = \mathbf{0}. \tag{63}$$

4.2. Entropy flux relation for anisotropic elastic materials in general

Next, we consider **anisotropic bodies** with

$$g = \left\{\mathbf{Q} \in O; \quad \mathbf{Q}\mathfrak{m} = \mathfrak{m}, \quad \mathbf{Q}\mathfrak{M}\mathbf{Q}^T = \mathfrak{M}\right\}. \tag{64}$$

In other words g is characterized by the set $(\mathfrak{m}, \mathfrak{M})$ and the group O, i.e.

$$g = (O; \mathfrak{m}, \mathfrak{M}). \tag{65}$$

Then

$$\mathbf{k} = \hat{\mathbf{k}}(\theta, \mathbf{g}_\kappa, \mathfrak{m}, \mathfrak{M}) = \mathbf{A}(\theta, \mathfrak{m}, \mathfrak{M})\mathbf{g}_\kappa + \mathbf{a}(\theta, \mathfrak{m}, \mathfrak{M}) \tag{66}$$

is isotropic vector-valued function, i.e.

$$\mathbf{Q}\mathbf{k}(\theta, \mathbf{g}_\kappa, \mathfrak{m}, \mathfrak{M}) = \mathbf{k}(\theta, \mathbf{Q}\mathbf{g}_\kappa, \mathbf{Q}\mathfrak{m}, \mathbf{Q}\mathfrak{M}\mathbf{Q}^T), \tag{67}$$

or

$$\mathbf{Q}\mathbf{A}(\theta, \mathfrak{m}, \mathfrak{M})\mathbf{g}_\kappa + \mathbf{Q}\mathbf{a}(\theta, \mathfrak{m}, \mathfrak{M}) = \\ \mathbf{A}(\theta, \mathbf{Q}\mathfrak{m}, \mathbf{Q}\mathfrak{M}\mathbf{Q}^T)\mathbf{Q}\mathbf{g}_\kappa + \mathbf{a}(\theta, \mathbf{Q}\mathfrak{m}, \mathbf{Q}\mathfrak{M}\mathbf{Q}^T)$$

which must hold for every $\mathbf{Q} \in O$ and every $\mathbf{g}_\kappa$. Particularly for $\mathbf{g}_\kappa = \mathbf{0}$, we have

$$\mathbf{Q}\mathbf{a}(\theta, \mathfrak{m}, \mathfrak{M}) = \mathbf{a}(\theta, \mathbf{Q}\mathfrak{m}, \mathbf{Q}\mathfrak{M}\mathbf{Q}^T), \tag{68}$$

i.e. $\mathbf{a}(\theta, \mathbf{m}, \mathbf{M})$ is vector valued isotropic function of its arguments. Moreover,

$$\mathbf{Q}\mathbf{A}(\theta, \mathfrak{m}, \mathfrak{M})\mathbf{g}_\kappa = \mathbf{A}(\theta, \mathbf{Q}\mathfrak{m}, \mathbf{Q}\mathfrak{M}\mathbf{Q}^T)\mathbf{Q}\mathbf{g}_\kappa \tag{69}$$

or

$$\mathbf{Q}\mathbf{A}(\theta, \mathfrak{m}, \mathfrak{M})\mathbf{Q}^T\mathbf{Q}\mathbf{g}_\kappa = \mathbf{A}(\theta, \mathbf{Q}\mathfrak{m}, \mathbf{Q}\mathfrak{M}\mathbf{Q}^T)\mathbf{Q}\mathbf{g}_\kappa. \tag{70}$$

This must hold for any for every $\mathbf{Q} \in O$, and hence

$$\mathbf{Q}\mathbf{A}(\theta, \mathfrak{m}, \mathfrak{M})\mathbf{Q}^T = \mathbf{A}(\theta, \mathbf{Q}\mathfrak{m}, \mathbf{Q}\mathfrak{M}\mathbf{Q}^T), \tag{71}$$

i.e. $\mathbf{A}(\theta, \mathfrak{m}, \mathfrak{M})$ is skew symmetric tensor valued isotropic function of its arguments.

Now we need representations in three dimensional space for vector-valued and skew-symmetric tensor valued isotropic functions (See G.F. Smith [15], A. J.M. Spencer [21], ...). We shall write it for all groups of crystal classes given by Liu [14].

5. Conclusion

In this paper we investigated the consequences of the assumption that $\Lambda^{\varepsilon} = \Lambda^{\varepsilon}(\theta)$ irrespective of whether the classical entropy-flux relation is valid. We used this assumption to derive the relationship between the entropy flux and heat flux for all isotropic materials as well as for some crystal classes including transverse isotropy, orthotropy, triclinic systems and rhombic systems. Under this assumption we first re-examined the entropy flux-heat flux relation for viscoelastic materials, isotropic elastic materials, transversely isotropic elastic bodies and the transversely isotropic rigid heat conductors examined by I. Müller and I-Shih Liu [6]-[13]. For all these cases our analysis confirms that $\Lambda^{\varepsilon} = \Lambda^{\varepsilon}(\theta)$ is a sufficient condition for the determination of the entropy flux-heat flux relation.

Furthermore, we derived the entropy flux-heat flux relations for all the crystal classes, given by I-Shih Liu [14], for which representations of anisotropic functions with respect to the symmetry groups of these crystal classes can be expressed in terms of isotropic functions. Our derivation is very general in the sense that the constitutive relations are non-linear. One of our main results is the proof that all crystal elastic bodies, we considered, are hyperelastic. This is a generalization of I-Shih Liu's finding for transversely isotropic bodies, the only case he analysed, where our results fully agree with his.

Also, we derived the entropy flux-heat flux relations for the all crystal classes considered when assumed to be rigid heat conductors.

We would like to draw attention to the following three points:

i. The vector function $\mathbf{a}$ and skew-symmetric function $\mathbf{A}$ are isotropic functions depending only on the set $(\theta, \mathfrak{m}, \mathfrak{M})$ which simplifies the procedure,

ii. Generally the classical entropy flux-heat flux relation does not hold; it is true for all crystal classes investigated here except for g_2, $g_6 = g_{14}$.

iii. The heat flux in the absence of a temperature gradient is not zero for all crystal classes.

Of course, all our predictions have to be verified to show that $\Lambda^{\varepsilon} = \Lambda^{\varepsilon}(\theta)$ is also a necessary condition, at least for all crystal classes investigated above. This is a task for future investigation.

Appendix

>From (38) and (39) it is ease to see that

$$\begin{aligned}
&\mathbf{n}_i \otimes \mathbf{n}_j = (\mathbf{n}_i \otimes \mathbf{n}_j)^n \quad \text{for any natural number } n,\\
&\mathbf{N}_i\mathbf{v} \quad = -\mathbf{n}_i \times \mathbf{v},\\
&\mathbf{N}_i\mathbf{N}_j \quad = \mathbf{n}_i \otimes \mathbf{n}_j - \delta_{ij}\mathbf{I},\\
&\mathbf{N}_i\mathbf{N}_j\mathbf{v} \quad = (\mathbf{n}_i \cdot \mathbf{v})\mathbf{n}_j - \delta_{ij}\mathbf{v},\\
&\mathbf{N}_i^2\mathbf{N}_j \quad = -\delta_{ij}\mathbf{N}_i,\\
&\mathbf{w} \cdot \mathbf{N}_i\mathbf{v} \quad = \mathbf{w} \cdot (\mathbf{v} \times \mathbf{n}_i),\\
&\mathbf{w} \cdot \mathbf{N}_i\mathbf{N}_j\mathbf{v} = (\mathbf{n}_i \cdot \mathbf{v})(\mathbf{n}_j \cdot \mathbf{w}) - \delta_{ij}(\mathbf{v} \cdot \mathbf{w}),\\
&\mathrm{tr}\mathbf{N}_i \quad = 0,\\
&\mathrm{tr}\mathbf{N}_i\mathbf{N}_j \quad = -2\delta_{ij}
\end{aligned}$$

for any vectors $\mathbf{v}$ and $\mathbf{w}$.

We note also that

$$\begin{aligned}\mathbf{n}_i \otimes \mathbf{n}_j - \mathbf{n}_j \otimes \mathbf{n}_i &= e_{ijk}\mathbf{N}_k,\\ \mathbf{N}_i\mathbf{N}_j - \mathbf{N}_j\mathbf{N}_i &= -e_{ijk}\mathbf{N}_k.\end{aligned}$$

References

[1] Coleman B.D., Noll W (1963) The thermodynamics of elastic materials with heat conduction and viscosity, *Arch. Rational Mech. Anal.*, **13**, 167-178.

[2] Serrin, J., Ed., (1986) *New Perspectives in Thermodynamics*, Springer, Berlin.

[3] Šilhavý (1997) *The Mechanics and Thermodynamics of Continuous Media*, Springer.

[4] C. Truesdell and S. Bharatha (1977) *The concepts and logics of classical thermodynamics as a theory of heat engines*, Springer New York.

[5] Muschik Wolfgang, *Why so many "schools" of Themrodynamics?*, Atti dell'Accademia Peloritana dei Pericolanti Classe di Scienze Fisiche, Matematiche e Naturali, Vol. LXXXVI, CIS0801002 (2008) - Suppl. 1.

[6] Müller, I. (1971) The coldness, a universal function in thermoelastic bodies, *Arch. Rational Mech. Anal.*, **41**, 319-332.

[7] Müller, I., Die Kältefunktion, eine universelle Funktion in der Thermodynamik viskoser wärmeleitender Flüssigkeit, *Arch. Rational Mech. Anal.*, **40**, 1-36 (1971).

[8] Müller, I. (1967) On the entropy inequality, *Arch. Rational Mech. Anal.*, **26**, 118-141.

[9] Liu, I-Shih (1972) Method of Lagrange multipliers for explitation of the entropy principle, *Arch. Rational Mech. Anal.*, **46**, 131-148.

[10] Liu, I-Shih (2008) Entropy flux relation for viscoelastic bodies, *J. of Elasticity* **90**, 259-270.

[11] Liu, I-Shih (2009) On entropy flux of transversely isotropic elastic bodies, *J. Elast.* **96**, 97-104.

[12] I-Shih Liu (2009) Constitutive theory of anisotropic rigid heat conductors, *Journal of Mathematical Physics*, **50**, 083506,

[13] Liu, I-Shih (1996) On entropy flux-heat flux relation in thermodynamic with Langrange multipliers, *Continuum Mech. Thermody* **8**, 247-256.

[14] Liu, I-Shih., On Representation of Anisotropic Invariants, *Int. J. Engng Sci.* 1982.

[15] Smith, G.F. (1971) On isotropic functions of symmetric tensors, skew-symmetric tensors and vectors, *Int. J. Eng. Sci.* **9**, 899-916,

[16] Liu, I-Shih (2002) *Continuum mechanics*, Springer-Verlag, Berlin Heidelberg New York.

[17] Wilmanski, K. (2008) *Continuum Thermodynamics*, Series on advances in mathematics for applied sciences Vol. **77**, World Scientific Publishing Co. Pte. Ltd.

[18] Green A.E., Laws, N. (1972) On the Entropy Production Inequality, *Arch. Rational Mech. Anal.*, **45**, No.1, 47-53.

[19] Hutter, K. (1975) On thermodynamics and thermostatics of viscous thermoelastic solids in electromagnetic fields, *Arch. Rational Mech. Anal.*, **58**, 339-386 .

[20] Bargmann Swantje, Steinmann Paul (2007) Classical results for a non-classical theory: remarks on thermodynamic relations in Green-Naghdi thermo-hyperelasticity, *Continuum Mech. Thermodyn* pp. 59-66.

[21] Spencer, A.J.M. (1971) In *Continuum Physics* (Ed. by C. Eringen), Vol. I, Academic Press, New York.

[22] Eringen, A. C. (1967) *Mechanics of Continua*, John Wiley & Sons, Inc.

PROPERTIES OF COMPOSITE MATERIALS MADE WITH THE ADDITION OF RECYCLED RUBBER

Dragica Jevtić[1], Dimitrije Zakić[2], Aleksandar Savić[3], Aleksandar Radević[4]

[1]Professor, B.Sc.M.Sc.Ph.D., Faculty of Civil Engineering,
University of Belgrade, Bulevar kralja Aleksandra 73, 11000 Beograd, Serbia,
e-mail: dragica@imk.grf.bg.ac.rs,
[2]Assistant, B.Sc.M.Sc.Ph.D., Faculty of Civil Engineering,
University of Belgrade, Bulevar kralja Aleksandra 73, 11000 Beograd, Serbia,
e-mail: dimmy@imk.grf.bg.ac.rs,
[3]Teaching fellow, Faculty of Civil Engineering,
University of Belgrade, Bulevar kralja Aleksandra 73, 11000 Beograd, Serbia,
e-mail: sasha@imk.grf.bg.ac.rs,
[4]Ph.D. student, Faculty of Civil Engineering,
University of Belgrade, Bulevar kralja Aleksandra 73, 11000 Beograd, Serbia,
e-mail: aradevic@grf.bg.ac.rs

Abstract:
Wide spread application of car tires has led to huge amount of waste tires which need to be handled. According to EU directive 1999/31/EC, since the year of 2003. it is no longer permitted to dispose whole waste tires and since 2006. neither the pieces of waste tires in the environment. Recycling and reusing waste tires is a significant contribution to sustainability through a decrease of emissions of toxic gasses and conservation of natural resources. Results of own experimental investigation on concrete made with recycled rubber aggregate are presented in this paper. Density, consistency and air content were investigated on fresh state concretes. Mechanical properties (compressive and tensile strength), as well as durability investigations were made on composites in hardened state. At last, an overview of possibilities for utilization of recycled rubber in civil engineering is given.
Key words: concrete, composite, recycled rubber, mechanical properties, deformation properties, durability.

1. Introduction

Civil engineering represents a field in which natural resources are consumed in large amounts. For example, in global concrete production around 9 billion tons of aggregate are used each year. Respecting the sustainability postulates, the main goal is to find alternative sources of raw materials. Waste tyres may be regarded as a valuable raw material, because it can be completely recycled and reused for different purposes – among others as a partial substitute for concrete aggregates.

The primary product in the waste tire recycling process is the rubber granulate; the mass of so obtained grains represents 55-65% of the total mass of recycled tyres. The secondary product in this process is the steel wire with amount of 25-30% and the tertiary product are textile fibers with quantity of approximately 10% of the initial waste tyre mass [1,7].

Wide application of natural and artificial rubber materials in the last 200 years, especially in the car industry, has led to huge amount of used tyres which need to be handled. For instance, it is estimated (lacking accurate official data) that more than 28000 tons of waste tyres are "generated" in Serbia each year – of which around 7000 tons end up as fuel for cement industry. Recently, "Tigar" factory from Pirot has started to manufacture recycled-tyre products in its department for pressed rubber [2].

The basic problem for recycled tyres disposal sites represent the size and geometry of a tyre, i.e. the fact that 75% of the space it occupies is actually empty. Also, large quantities of used tyres at disposal sites are becoming a health hazard, being an excellent ground for pests (insects and rodents) and potentially a serious fire threat.

According to the EU 1999/31/EC Directive, since the year of 2003 the disposal of whole car tyres is forbidden and since 2006 even the disposal of cut (shredded) tyres is not allowed anymore.

In this paper, the results of own experimental research on rubberized concrete (i.e. concrete made with recycled rubber as a partial substitute for classic aggregate) will be presented.

2. Experimental part

Thanks to the kindness of "Tigar" corporation representatives, the Material Testing Laboratory of the Faculty of Civil Engineering in Belgrade received a certain quantity of recycled tyre aggregate in size 0.5-4.0 mm. This granulate was used as the first fraction of aggregate in order to investigate the physical-mechanical properties of concrete based on recycled rubber addition.

With the intention of establishing and monitoring any changes in properties of concrete (both in fresh and hardened state) due to addition of recycled aggregate, certain amount of normal aggregate was substituted with waste rubber. Thus, three different concrete mixes were designed: reference concrete (marked as mixture number "1") with 0% of recycled tyre aggregate, mixture number "2" with 10% and mixture number "3" with 20% of waste rubber content in relation to the total mass of aggregate.

3. Testing of physical-mechanical properties of component materials

Considering the fact that the influence of the addition of waste rubber aggregate on properties of normal concrete was investigated, the usual amounts of component materials were used. Therefore, the quantity of cement in all three concrete mixtures was the same: 350 kg/m^3. Also, the water/cement ratio was constant and it amounted to 0.5. The projected consistency of all mixtures corresponded to the usual practical applications ranging between plastic and semi-plastic condition. For recycled rubber concrete mix design (i.e. for mixtures "2" and "3") an admixture was also applied: superplasticizer *Sika ViscoCrete 5-800* based on modified polycarboxilate, in amount of 0.5% related to the mass of cement.

Such composition of concrete points to the fact that mixtures "2" and "3" can be placed into category of lightweight concrete composites (with density in fresh state less than 2000 kg/m^3). The actual composition of all investigated concrete mixtures is presented in the following Table 1.

Table 1 – Designed concrete mixtures

Concrete	ω	m_c (kg/m^3)	m_{ad} (kg/m^3)	m_w (kg/m^3)	m_a (kg/m^3)	m_I (kg/m^3)	m_{II} (kg/m^3)	m_{III} (kg/m^3)	m_{rr} (kg/m^3)
"1"	0.5	350	-	175	1804	769	393	642	-
"2"	0.5	350	1.75	175	1464	624	319	521	146
"3"	0.5	350	1.75	175	1232	525	269	439	246

Symbols used in the table: ω – water/cement ratio, m_c – mass of cement, m_{ad} – mass of superplasticizer, m_w – mass of water, m_a – mass of aggregate, m_I – mass of the first fraction of aggregate, m_{II} – mass of the second fraction of aggregate, m_{III} – mass of the third fraction of aggregate, m_{rr} – mass of recycled rubber.

The specific gravity of recycled rubber granulate was determined using pyknometer test. Considering the fact that diameter of the rubber grains ranged between 0 and 4 mm, and that any additional cutting was not possible, these grains were only dried in the oven before the test. For this testing, terpentine with density of 0.85 g/cm^3 was applied. The average specific gravity of the recycled rubber granulate was determined to be γ_{sr}=1.144 g/cm^3.

Based on the glass jar method, the average value of rubber aggregate density was adopted to be γ_r=0.470 g/cm^3.

Determination of grain size distribution of recycled rubber was conducted using the dry sieving method according to *SRPS EN 933-1:2009* standard, which is the same procedure as for the natural aggregate. The results of this test are presented in Table 2. Most part of the applied recycled rubber aggregate (even 71.6%) had grain size between 1 and 2 mm, which can be seen in Figure 1.

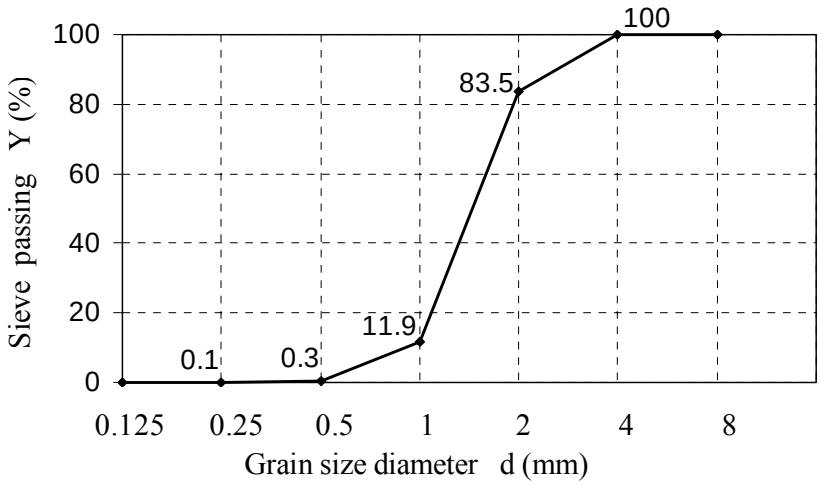

Figure 1 – Grain size distribution curve of recycled rubber aggregate

As a binder, Portland cement type *PC 20M(S-L) 42.5R "Lafarge"Beočin* was used, with measured specific gravity of 3.05 g/cm^3. Natural river coarse aggregate "Moravac" was also applied. The grain size distribution of all aggregates (three standard fractions of river aggregate + rubber granulate) is shown in Table 2.

Table 2 – Grain size distribution of applied aggregates

Sieve opening (mm)	0.125	0.25	0.5	1	2	4	8	16	31.5	45
I (0/4 mm)	1.9	14	54.2	68.2	83.4	98.2	100	100	100	100
II (4/8 mm)	0	0	0	0	0.6	16.3	95.4	100	100	100
III (8/16 mm)	0	0	0	0	0	0.5	4.5	99.2	100	100
Rubber granulate	0	0.1	0.3	11.9	83.5	100	100	100	100	100

As it was already mentioned, in order to improve the consistency of concrete mixtures "2" and "3", *Sika ViscoCrete 5-800* admixture was used in amount of 0.5%. It is a third generation superplasticizer, usually applied for concrete with prolonged transportation and placing time, when significant water reduction is needed (up to 30% in relation to reference concrete) as well as high workability of mixtures. The density of this admixture was 1.077 g/cm^3, and its pH value 4.5-5.5. According to the producer's technical sheets the recommended dosage of the admixture varies between 0.3-0.8% (of cement mass) for normal concrete, i.e. 0.8-1.6% for flowing consistency and Self Compacting Concrete.

The following mixing procedure was adopted for concrete number "1":

- The prescribed quantities of cement and aggregates were measured;
- These components were put into the mixing drum in the following order-first the coarse fractions II and III, then cement and finally the fine aggregate fraction I;
- Next, the prescribed quantity of water was measured;
- The dry components were mixed for 30 seconds*;*
- At last, the measured quantity of water was added into the mixer during the next 30 seconds and the mixing of fresh concrete was continued for total time of 90 seconds.

Considering the usually poor adhesion between the artificial (rubber) and natural (stone) aggregate, somewhat modified mixing procedure was adopted for concrete mixtures "2" and "3". Namely, in this case, first water and cement were mixed together, for a period of approximately 90 seconds. Next, the rubber granulate was added to the mixture in order to allow the cement paste to surround the rubber grains – preparing them for better connection with the natural aggregate. During the next period of 120 seconds, the chemical admixture (i.e. superplasticizer) was gradually put into the mixing drum. At last, the two fractions of the natural aggregate were added and the fresh concrete was mixed for another 120 seconds.

All three concrete mixtures were placed into molds using vibrating table with smaller amplitude and frequency – due to the high possibility of segregation (i.e. separation of the rubber granulate from the fresh concrete mix). For the same reason, during the mixing process of mixtures "2" and "3", the vibrating time was reduced for one third.

After placing, the concrete specimens were cured in a chamber protected from vibrations and impact, at min 95% relative air humidity and temperature of 20±2°C, for the first 24 hours. After this initial period, the specimens were demolded and put into the 20±2°C warm water to be cured until the day of testing.

4. Fresh concrete testing

The consistency of fresh concrete mixtures was determined according to the *SRPS EN 12350-2:2010* standard. Slump values of 50 mm, 65 mm and 51 mm were obtained for concrete mixtures "1", "2" and "3", respectively. These results correspond to the semi-plastic grade of consistency, defined as the class S2.

Density of concrete in the fresh state was determined according to the *SRPS EN 12350-6:2010* standard. First, the concrete samples were compacted on the vibrating table and after that the density was measured. The average values of density for concrete mixtures "1", "2" and "3" (each one based on 28 testing results), are presented in the Table 3, together with slump and entrained air content values.

Table 3 – Testing results for fresh concrete

Concrete mixture	"1"	"2"	"3"
Density (kg/m^3)	2382	2004	1748
Slump (mm)	50	65	51
Air content (%)	3.1	4.8	6.4

These testing results indicate that the density of fresh concrete is decreasing with the increment of rubber content - almost with linear rate, which corresponds with the conclusions made by other researchers in this field [3-5].

5. Hardened concrete testing

The investigation performed on hardened concrete included: testing of compressive strength at 7 and 28 days (marked as $f_{c,7}$ and $f_{c,28}$), axial tensile strength ($f_{t,28}$) and splitting tensile strength ($f_{st,28}$), deformation properties, as well as simultaneous aggressive action of frost and deicing salts.

The results acquired during the strength testing of all three concrete mixtures in hardened state, are presented in Table 4. Below that, there is a Figure 2 showing compared values of compressive strength of concretes "1", "2" and "3" at 7 and 28 days of age.

Table 4 – Results of compressive and tensile strength testing [MPa]

Concrete	$f_{c,7}$	$f_{c,28}$	$f_{t,28}$	$f_{st,28}$
"1"	39.8	41.8	2.82	2.98
"2"	10.9	13.5	1.27	1.68
"3"	6.2	6.6	0.63	0.62

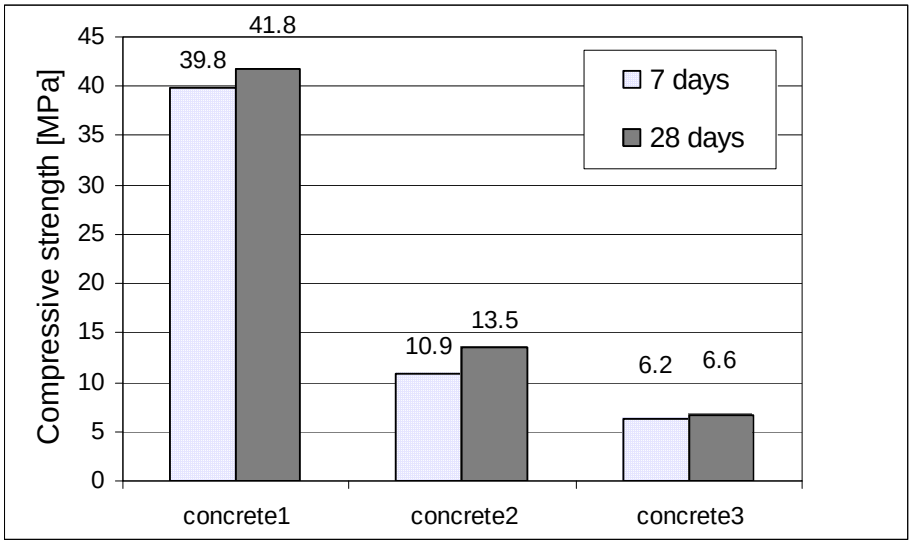

Figure 2 – Compressive strength of concrete at 7 and 28 days of age

Axial tensile strength and splitting tensile strength were determined according to the dispositions shown in the following photos (Figure 3).

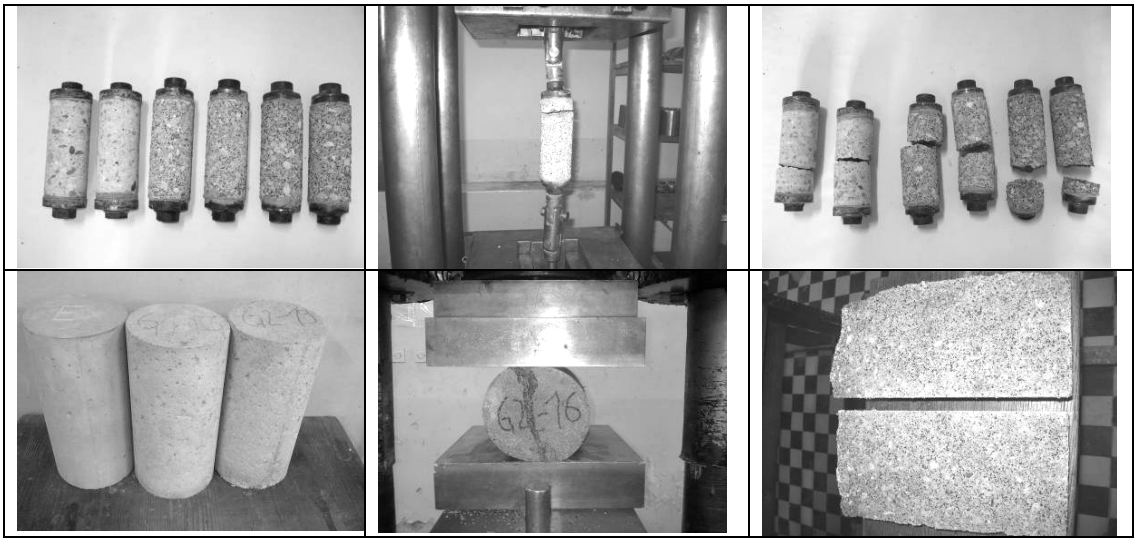

Figure 3 – Appearance of concrete specimens before, during and after the axial tensile test (upper row of photos) and the splitting tensile test (lower row of photos)

Deformation characteristics of composites conducted by deflections (Fig. 4) and using ultrasonic pulce velocity method as well as measuring the dynamic modulus of elasticity through resonant frequency (Fig. 5).
Obtained results of these measurements are presented in Table 5.

Figure 4 – Testing of static modulus of elasticity

Figure 5 – Ultrasonic pulse velocity measurements

Table 5 – Results of static and dynamic modulus of elasticity

Concrete	Density (kg/m^3)	E_s (GPa)	E_D (GPa)	v (m/s)	μ (/)
"1"	2370	30.9	38.8	4211	0.18
"2"	1931	17.1	18.4	3123	0.23
"3"	1702	6.3	9.1	2415	0.25

The testing of simultaneous action of frost and deicing salts consisted of cyclic frost/thaw periods (25 cycles) using three concrete specimens (per each mixture) with upper surface subjected to the NaCl water solution – according to the Serbian standard *SRPS U.M1.055:1984.* After the prescribed treatment, the visual evaluation of concrete surface degradation was performed. This procedure showed that there were no visible traces of degradation on any of the concrete specimens.

6. Conclusions

Based on the experimental research results, the conclusion can be drawn that the waste rubber granulate can be successfully applied as aggregate for cement based composites. It is important to stress out that the rubber content (i.e. the percentage of natural aggregate's substitution) has significant influence on properties of concrete, both in fresh and hardened state. The influence on fresh concrete properties is mostly visible when changes in density, air content and mixing procedure are concerned, but there is also increased need for superplasticizer application in order to achieve the target consistency.

The addition of recycled rubber has also considerable influence on hardened concrete properties – leading to reduced mechanical strengths. Namely, both compressive and tensile strength tend to decline with increased content of applied rubber aggregate. This conclusion was also reached and documented in several previous investigations [3-5].

The so-called rubberized concrete belongs to the category of lightweight cement composites
(density: $\gamma<2000$ kg/m^3), with possible wide-range application in civil engineering.

Observing the deformation characteristics through resonant frequency, ultrasonic pulse velocity and modulus of elasticity it is obvious that rubberized composite materials have shown the decrease of these values.

As far as the durability of such composite materials is concerned, the experimentally proved fact that they are substantially resistant to the combined action of frost and deicing salts is very promising.

Due to its advantages, such as elasticity, durability and frost/thaw resistance, the waste rubber granulate has already found different applications in the field of road construction. Namely, for a long period recycled tyre has been used as addition to the asphalt mixtures, in order to exploit fully the advantages of this material – such as: traffic noise reduction, decreased stopping distance, as well as prolonged service life of pavement combined with

better resistance to cracks. Recycled rubber based composites are also widely applied for production of precast concrete elements in road and railroad construction, such as: parking and traffic barriers, curbs, grade crossings, railroad track ties, rubber panels, speed reducers, bumps, etc.

Considering the facts that rubberized concrete has high capacity of vibration and sound absorption, as well as lower sensitivity to temperature changes, recycled tyres can also be applied for roof insulation, soundproofing barriers, water-tight membranes, porous bitumen binders, pipes, sport fields and playground areas, pavements in parks and pedestrian zones, etc.

Acknowledgement. The research described in this paper is a part of Project N^{o} 36017: "Utilization of by-products and recycled waste materials in concrete composites in the scope of sustainable construction development in Serbia: Investigation and environmental assessment of possible applications" financed by Ministry of Science and Technological Development, Republic of Serbia.

Literature

[1] D. Raghavan, H. Huynh and C.F. Ferraris: *Workability, mechanical properties and chemical stability of a recycled tyre rubber-filled cementitious composite*, J Mater Sci 33 (1998), pp. 1745–1752.,
[2] J. Hodolič, M. Stević, Đ. Vukelić, A. Zajac: *Reciklaža i prerada otpadnih pneumatika, Festival Kvaliteta, 3. konferencija o kvalitetu života*, Kragujevac, maj 2008.,
[3] Topcu, I.B., 1995.: *The properties of rubberized concrete*, Cement and Concrete Research 25 2, pp. 304–310.,
[4] N.I. Fattuhi and L.A. Clark: *Cement-based materials containing shredded scrap truck tyre rubber*, Construction and Building Materials 10 (1996), pp. 229–236.,
[5] A.M. Ghaly and J.D. Cahill IV: *Correlation of strength, rubber content, and water to cement ratio in rubberized concrete*, Can J Civil Eng 32 (6) (2005), pp. 1075–1081.,
[6] R.M. Mercedes, J.S.C. Astorqui and M.G. Cortina: *Viability analysis and constructive applications of lightened mortar (rubber cement mortar)*, Constr Build Mater 21 (2007), pp. 1785–1791.,
[7] *SRPS EN 933-1:2009. - Ispitivanje geometrijskih svojstava agregata - Deo 1: Određivanje granulometrijskog sastava - Metoda prosejavanja*
[8] *SRPS EN 12350-2:2010 – Ispitivanje svežeg betona - Deo 2: Ispitivanje sleganja*.,
[9] *SRPS EN 12350-6:2010 – Ispitivanje svežeg betona - Deo 6: Zapreminska masa*.,
[10] *SRPS U.M1.055.:1984 - Beton - Ispitivanje otpornosti površine betona na dejstvo mraza i soli za odmrzavanje.*
[11] D. Jevtić, D. Zakić, A. Savić and A. Radević (2011): *The possibility of use of recycled rubber as aggregate in concrete type composites*, XIII International conference YUCCORR, Tara.
[12] M. Aćić, D. Jevtić, (2011): *Mogućnosti korišćenja recikliranih materijala kao agregata za beton u savremenoj građevinskoj praksi,* VII Međunarodni naučno stručni skup ZIBL Banja Luka.

EFFECT OF CREEP AND SHRINKAGE ANALYSIS ON DEFLECTIONS OF CONTINUOUS COMPOSITE BEAMS

S. Kostić[1], B. Deretić-Stojanović[2], S. Stošić[3]

[1] Faculty of Civil Engineering,
University of Belgrade, Bul. kralja Aleksandra 73, 11000 Belgrade, Serbia
e-mail: svetlana@grf.bg.ac.rs
[2] Faculty of Civil Engineering,
University of Belgrade, Bul. kralja Aleksandra 73, 11000 Belgrade, Serbia
e-mail: biljads@grf.bg.ac.rs
[3] Faculty of Civil Engineering,
University of Belgrade, Bul. kralja Aleksandra 73, 11000 Belgrade, Serbia
e-mail: sasa@grf.bg.ac.rs

Abstract. Creep and shrinkage of concrete affect the behavior of steel-concrete composite beams and should be taken into account in the analysis of these structures. A number of methods which have different level of accuracy are available for the time analysis of composite structures. Eurocode 4, the contemporary European code for design of steel-concrete composite structures, recommends simple methods for calculation of creep and shrinkage effects. In this paper, the deflections of continuous composite beams calculated with method proposed by Eurocode 4 and the more accurate Age Adjusted Effective Modulus Method (AAEM) are compared. Cracking of concrete is also considered. Through a set of numerical examples, accuracy of methods proposed by Eurocode 4 is discussed.

1. Introduction

Creep and shrinkage of concrete affect behavior of continuous composite steel-concrete beams. Due to these viscous deformations, the redistribution of stresses and change in deformations of composite beam occur in time. Therefore, the analysis should include these effects [1].
There are several methods that with different accuracy take into account the viscous deformations. In this paper, two methods are explained and studied: method proposed by Eurocode 4 [2] which is based on the Effective Modulus Method (EM) and the Age Adjusted Effective Modulus Method (AAEM) [3].

2. Creep and shrinkage effects according to Eurocode 4

Eurocode 4 [2], the contemporary European code for design of steel-concrete composite structures, recommends a simple method for including viscous deformations of concrete into analysis. According to this code, creep and shrinkage effects can be taken into account using the following modular ratio n_L for the concrete:

$$n_L = n_0\left(1+\psi_L\varphi_t\right) \tag{1}$$

with:

n_0 the modular ratio between modulus of elasticity of steel and concrete for short term loading E_a/E_{cm},

E_{cm} the secant modulus of elasticity of concrete for short-term loading

φ_t the creep coefficient determined according to Eurocode 2 [4]

ψ_L the creep multiplier which depends on the type of loading and is equal to 1.1 for permanent loading, 0.55 for effects of shrinkage and 1.5 for prestressing by imposed deformations.

This method is based on the well-known Effective Modulus Method (EM) [3] with the effective modulus of concrete $E_{c,eff}$ given by the expression:

$$E_{c,eff} = \frac{E_{cm}}{1+\psi_L\varphi_t}. \tag{2}$$

The stress-strain relation for concrete in time *t* is linear:

$$\sigma_c(t) = E_{c,eff}\left(\varepsilon_c - \varepsilon_{sh}\right) \tag{3}$$

where ε_c is the concrete strain and ε_{sh} is the shrinkage strain.

Therefore, according to this method, analysis of composite beam under long-term loading is equivalent to the analysis of composite beam under short-term loading, with the difference that instead of modulus of elasticity of concrete E_{cm}, the effective modulus of concrete $E_{c,eff}$ is used.

3. AAEM method

The assumed stress-strain relation for concrete in time *t* according to the AAEM method is:

$$\sigma_c(t) = E_{c,aeff}\left(\varepsilon_c - \varepsilon_{sh}\right) - \rho_c\sigma_{co} \tag{4}$$

where

$E_{c,aeff}$ is the age-adjusted effective modulus of concrete equal to:

$$E_{c,aeff} = \frac{E_{co}}{1+\chi\varphi_t} \tag{5}$$

E_{co} is the modulus of concrete at the time of loading t_0;

χ is the aging coefficient with values in the range (0.6-0.9);

ρ_c the coefficient equal to $(1-\chi)\varphi_t / (1+\chi\varphi_t)$

Analysis according to this method is, because of the accepted stress-strain relation (4), more complex than EC4 analysis, but, due to consideration of the aging of concrete, it is also more accurate.

4. Numerical study

In order to compare the maximal deflections of continuous composite beams obtained with taking into account creep and shrinkage effects through the two previously explained methods, the following numerical examples are studied.

Four continuous composite beams with spans commonly used in building structures are analyzed with the computer program "Kontinualac" [5]. The study is limited to girders applied in buildings, not mainly intended for storage, not pre-stressed by controlled deformations and constructed as propped. A brief description of beams follows.

Beam 1 is the two span continuous composite beam (Fig. 1) with equal span lengths $L_1=L_2=10$m. Dead loading is 16 kN/m and live loading is 24 kN/m.

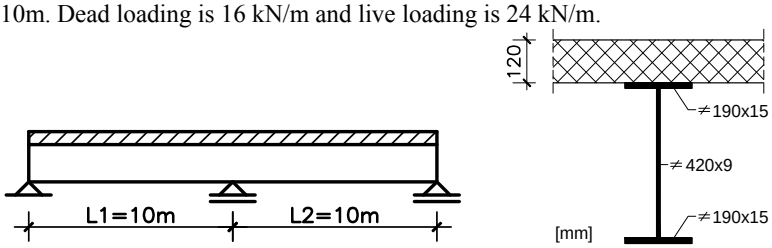

Figure 1. Beam 1 and its cross-section.

Spacing between adjacent beams is 5m, reinforcement in the slab is Ø10/12.5cm with $f_{sk}=42$kN/cm^2 and $E_s=210$kN/mm^2, constructional steel grade is S235 and concrete class is C25/30.

Beam 2 is the two span continuous composite beam (Fig. 2) with equal span lengths $L_1=L_2=12$m. Dead loading is 17.1 kN/m and live loading is 25.6 kN/m.

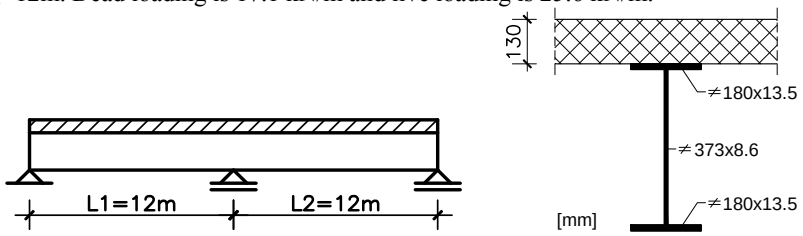

Figure 2. Beam 2 and its cross-section.

Spacing between adjacent beams is 3m, reinforcement in the slab is Ø12/15cm with $f_{sk}=50$kN/cm^2 and $E_s=210$kN/mm^2, constructional steel grade is S355 and concrete class is C25/30.

Beam 3 is the two span continuous composite beam (Fig. 3) with equal span lengths $L_1=L_2=9.5$m. Dead loading is 21.8 kN/m and live loading is 20 kN/m.

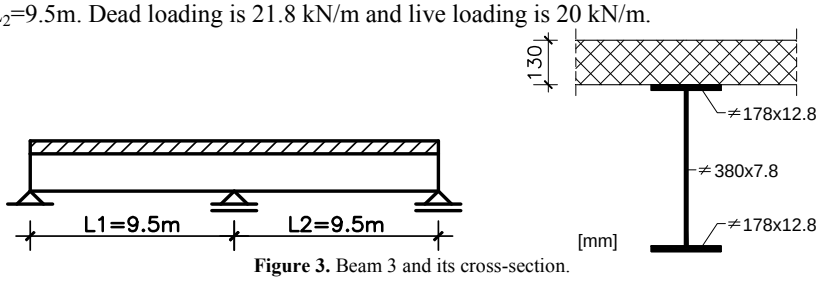

Figure 3. Beam 3 and its cross-section.

Spacing between adjacent beams is 4m, reinforcement in the slab is Ø8/10cm with f_{sk}=46kN/cm^2 and E_s=210kN/mm^2, constructional steel grade is S355 and concrete class is C25/30.

Beam 4 is the three span continuous composite beam (Fig. 4) with equal span lengths L_1=L_2= L_3=9m. Dead loading is 22 kN/m and live loading is 25 kN/m.

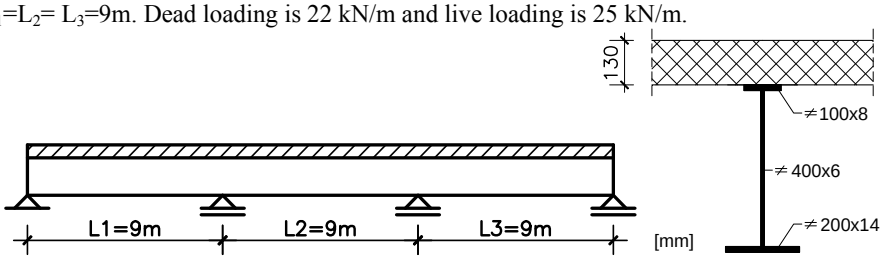

Figure 4. Beam 4 and its cross-section.

Spacing between adjacent beams is 3m, reinforcement in the slab is Ø12/10cm with f_{sk}=42kN/cm^2 and E_s=210kN/mm^2, constructional steel grade is S235 and concrete class is C25/30.

4.1. Type of analyses

According to EC4 [2], for verification of serviceability limit states, the creep effects need to be taken into account. The effects of shrinkage of concrete in some cases can be neglected [6]. Also, cracking of concrete in the area of intermediate supports has to be included in the analysis. EC4 [2] allows two simple methods for taking into account this effect: "15% cracked" analysis and "cracked analysis".

In the "15% cracked" analysis, the following variation of flexural stiffness over the length of a beam is assumed: within the support range, over 15% of the field length, flexural rigidity is EaI_2 of the cracked section (Ea is modulus elasticity of steel, I_2 is second moment of area of the equivalent steel section neglecting concrete in tension but including reinforcement); in the remaining regions, flexural rigidity is the "uncracked" section rigidity, EaI_1 (I_1 is second moment of area of the effective equivalent steel section assuming that concrete in tension is uncracked). Flexural rigidity EaI_2 does not include the tension stiffening effect.

The "cracked" analysis is an iterative procedure. In the first iteration, internal forces and moments are calculated assuming uncracked concrete slab (stiffness EaI_1). In the areas where concrete tensile stresses exceed prescribed value ($2.0f_{ctm}$, f_{ctm} is the mean value of the axial tensile strength of concrete), flexural rigidity is reduced to the value of the cracked section (EaI_2). The second iteration starts with this new distribution of flexural rigidities, and so on.

Referring to the shear lag effect, the constant effective width is assumed over each span with widths found from the expressions given in EC4 [2].

Considering all mentioned effects, the following 4 analyses suitable for serviceability limit state verifications are performed in order to found maximal deflections:

Analysis 1: The effects of shrinkage are neglected; creep effects are taken into account by using two different modular ratios n_o and n_L for short-term and long-term loadings. Variations of this method, related to cracking of concrete effect, are explained below:

a) "15% cracked" analysis is applied
b) "cracked" analysis is applied

Analysis 2: The creep effects are taken into account by using two different modular ratios n_o and n_L for short-term and long-term loadings. Shrinkage effects are calculated using the appropriate modular ratio n_s. The same variations of this method a) and b), related to cracking of concrete effect, are performed.
Analysis 3: The effects of shrinkage are neglected. Separate analyses for long-term and short-term loadings are done and long-term effects are calculated according to AAEM method. The a) and b) variations of this method, related to cracking of concrete effect, are performed.
Analysis 4: The effects of shrinkage are included. Separate analyses for long-term and short-term loadings are done and long-term effects are calculated according to AAEM method. The a) and b) variations of this method, related to cracking of concrete effect, are performed.

4.2. Results

Results of the analysis are given in Table 1 and Table 2.

Table 1 Maximal deflection in [m], Analysis 1 and 2

Beam type:	Analysis 1		Analysis 2	
	a)	b)	a)	b)
1	0,0183	0,0171	0,0223	0,0199
2	0,0344	0,0336	0,0405	0,0390
3	0,0212	0,0199	0,0255	0,0230
4	0,0191	0,0180	0,0233	0,0213

Table 2 Maximal deflection in [m], Analysis 3 and 4

Beam type:	Analysis 3		Analysis 4	
	a)	b)	a)	b)
1	0,0184	0,0172	0,0222	0,0198
2	0,0347	0,0340	0,0405	0,0390
3	0,0214	0,0200	0,0255	0,0230
4	0,0192	0,0181	0,0232	0,0212

According to the results of Analysis 1 and Analysis 3, the deflections found by the AAEM method are very slightly greater than found by EC4 method. However, these differences between the results are negligible.

According to the results of Analysis 2 and Analysis 4, when shrinkage effects are also included, differences between results of the two analyses completely disappear.

Therefore, the application of simple method proposed by EC4 is fully legitimate for deflection analysis of continuous composite beams.
The effects of shrinkage increase maximal deflections by approximately 20%. Also, in all studied cases the “15% cracked” analysis gave larger deflections than “cracked” analysis, which is on the safe side.

5. Conclusions

EC4 allows use of simple method based on the EM method for taking into account the creep and shrinkage effects. Results for maximal deflections for set of four continuous composite girders obtained with this analysis are compared with the results obtained with more accurate AAEM method. The results have shown that the differences in results are negligible, and that is, therefore, EC4 method suitable for practical applications due to its simplicity.

Acknowledgement. The first author would like to thank the Ministry of Science of the Republic of Serbia for financial support under the project TR36046.

References

[1] Johnson R P (2004) *Composite Structures of Steel and Concrete: Beams, Slabs, Columns and Frames for Buildings*, 3rd e., Blackwell Publishing, Oxford.
[2] EN 1994-1-1(2004): *Eurocode 4: Design of composite Steel and Concrete Structures – Part 1-1: General Rules and Rules for Buildings*, CEN.
[3] Deretić-Stojanović B and Kostić S (2009) Creep and Shrinkage Analysis According to EC4, *Proceedings of the 13th International MASE Symposium*, 14-17 October, Ohrid, Macedonia, pp. 175-180.
[4] EN 1992-1-1: (2004) *Eurocode 2: Design of Concrete Structures – Part 1-1: General Rules and Rules for Buildings*, CEN.
[5] Seizović S (2006) *Analysis of Continuous Composite Steel and Concrete Beam*, Master thesis, Faculty of Civil Engineering, University of Belgrade.
[6] Kostić S and Deretić-Stojanović B (2010) Proračun skupljanja i tečenja pri analizi spregnutih kontinualnih nosača prema EC4, *GNP 2010 – Treći internacionalni naučno-stručni skup: Građevinarstvo – nauka i praksa*, Žabljak, pp. 609-614.

TENSILE FEATURES OF HOLE IN PLATE SPECIMEN TESTING BY THERMOGRAPHY AND CONVENTIONAL METHOD

M. Kutin[1], S. Ristic[1], M. Puharic[1], M. Ristic[1]

[1]Institut Goša, Milana Rakica 35, Belgrade, Serbia

e-mail: s1avce@yahoo.com

Abstract The paper shows the results obtained in the simultaneously testing of the hole in plate specimen made of structural steel, using conventional methods and thermography. The main aim of testing was to relate the temperature changes of the spacemen, continuously recorded by thermography, with stress – extension diagram. It enables to predict reaching the critical stresses, which cause the appearance of fractures and to define the criteria on determining the maximum sample temperature alteration in the field of the elastic and elastic-plastic strains. The testi of specimens was carried out on the electromechanical testing machine, with the displacement and the strain (extension) control at room temperature. Infrared camera Therma CAM SC640, FLIR Systems, was used for the thermograms recordings. The tests using the methods of fracture mechanics were applied due to the safety assessment of metal structures. The conventional methods were applied simultaneously. The numerical simulation of stress is made for the same sample. The tensile test and thermography give visible data of surface stress distribution. This proves that the variations in temperature captured by the IR camera are strongly correlated to the loads actually applied to the specimen. Numerical simulation of stress distribution on the same model under same condition is presented, too.

Keywords: thermography, fracture techniques, tension, steel

1. Introduction

The characteristics, which describe the appearance and growth of the fatigue cracks under the impact of the static and dynamic loads, are the most important for exploitation safety of the complex metal structures. The conventional testing methods of the metal structures are well known [1-3]. The properties, obtained by tension tests describe the global mechanical behavior of the materials.

Thermography stands among the different NDT&E techniques, as an attractive tool for fast inspection of large surfaces. Thermography is a method which provides the analysis of thermoelastic stress, based on the measurement of infrared radiation, emitted by the object surface, which is exposed to dynamic or static, linear elastic or plastic strain and its conversion into visible image, named thermogram [3]. The surfaces emitting various amounts of infrared radiation can be differentiated on the thermogram by various colors or brightness

levels, whereas the surfaces emitting the equal heat amounts have the same color (isothermal surfaces).

In order to calculate the temperature of the monitored object from the radiation reaching the camera sensor and link it with stresses, it is necessary to know emissivity of the object surface, temperature of the surrounding objects, camera distance from the tested object, thermal losses, air temperature and relative humidity [2,3]. Because of that, it is very difficult to apply infrared thermography for quantitative, large objects inspection in the exploitation conditions.

Benefits of applying thermography as a nondestructive technique for inspection, monitoring and maintenance surveys of complex structures, operating in the real conditions of the static and dynamic loads, would be better used, if calibration diagrams (obtain in laboratory conditions) for structural materials and specific shape exist [2-8].

This paper presents some results relating to simultaneously testing of the contractual hole in plate specimen using conventional methods and thermography. The main aim of testing was to relate the temperature changes of the spacemen, continuously recorded by thermography, with stress – extension diagram.

Numerical simulation of stress distribution on the same model and same condition is presented, too. Finite element method (FEM) was chosen to simulate operating conditions (boundary conditions and load) [9-13]. The CATIA (Computer Aided Three-dimensional Interactive Application) software package has been used for generating finite element meshes, composed of tetrahedron type, three-dimensional finite elements [14]. FEM is based on a physical discretization of the considered parts of a continuum of finite dimensions and simple shapes called finite elements (FE). All finite elements are connected by common nodes to form the original structure. The basic types of finite elements are: one-dimensional (rods, beams, pipe fittings), two-dimensional (triangular, rectangular, membranes, plates and shells), three-dimensional (tetrahedron, prism, axisymmetric and others). In FEM studied domain (the strain body) is shared by using fictitious line on a number of finite elements. Set of finite elements for the entire domain make a network of finite elements. Stress and strains are described by interpolation functions and a finite number of parameters in the nodes. They are the basic parameters of the FEM. When the basic relations in the FEM are setting up, using the same principles and procedures, that are valid beyond the classical discrete models, they relate force and stress and stress and strain. By grouping the basic equations finite elements gets the equation structure in matrix form.

2. Experimental procedure

Experimental setup for structural steel, hole in plate specimen's tensile test is illustrated on the fig. 1. The testing of specimens was carried out on the electromechanical testing machine RM400, with displacement and the tension control at room temperature. The tension speed was 5 mm/min. The extension was registered using double extensometer. The precision of extensometer measurement is ±0,001 mm. Tensile testing and thermographic measurements were performed simultaneously.

Elements with circular hole in plate are often integral parts of the complex structures. For this reason, a series of spacemen have been investigated.

In Figure 2, the tested specimen is presented, schematic presentation of specimen before and after stretching (a), and photo of the same specimen after tensile test.

The samples have been coated using grey paint with known uniform emissivity, in order to improve their emissive properties.

Thermo CAM SC640 Infrared camera, FLIR Systems, has been used for recording thermogram. The camera resolution is 640 x 480 pixels. It was positioned on the distance of 0.5m related to the sample surface. Camera sensitivity is 60mK at 30°C, field of view is 24°x18°, minimum focus distance is 0.3m, spatial resolution is 0.65 rad, recording frequency is 30 Hz and electronic zoom is 1-8x continuously. Detector type is Focal Plane Array, non-cooled micro bolometer 640 x 480 pixels [3]. Camera spectral range is 7.5 to 13μm, whereas the temperature range is from -40°C to +1,500°C, with precision of ±2°C, ±2.

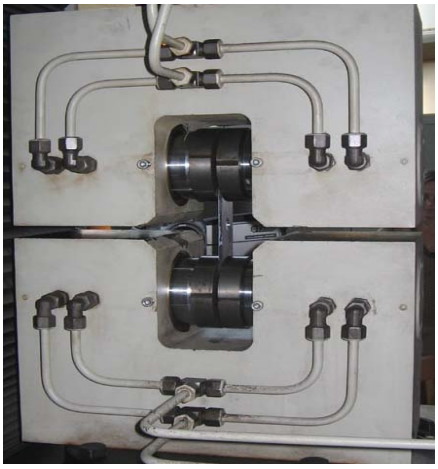

Figure 1. Specimens with a circular hole in RM400

During tests, thermography camera detected the temperature changes on spacemen surface and made the continuous track. The thermograms, as track sequences, were selected in characteristic time, which was chosen on the stress VS extension curve: force impact start, (elastic strain start), plastic strain start (Yield stress), point where is reached of maximum force, (end of homogeneous plastic strain), up to the final specimen fracture and finally after crack.

For real-time and static image analysis the associated software is used, because it contains powerful measurement and analysis functions for extensive temperature analysis, including isotherms, line profiles, area histograms, image subtraction capability and many more [3].

3. Results and discussions

The testing results are shown simultaneously in order to comprehend the possibilities based on the comparative analysis and to define the criterion for applying the thermography in predictions material and plate elements with hole behavior during inspection, monitoring and maintenance surveys of complex structures operating in the real conditions of the static and dynamic loads.

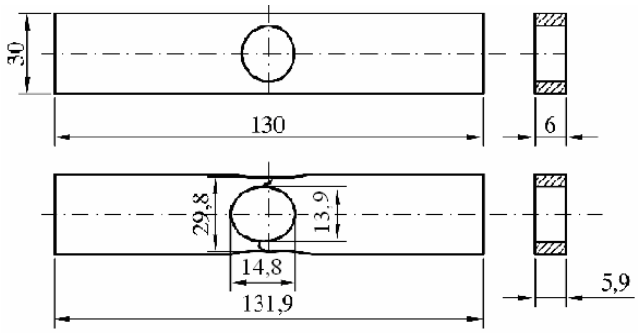

a

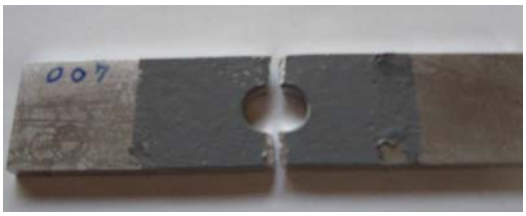

b

Figure 2. Specimen with a circular hole, a-shematic presentation, b-photo after specimen crack

With the help of the Thermo CAM Researcher software, the measuring areas were positioned around the hole of the specimen thermogram, AR01 bellow, AR02 above the hole, AR03 left and AR04 right of hole [2,3]. For a more precise analysis of the temperature variations on the tested specimen surface and its link to the mechanical properties, the detailed analysis has been conducted into the areas.

The upper left corner presents the recorded thermograms, right corner field indicates the minimum, average and maximum temperatures at the moment of recording. The bottom field contains the temperature distribution into the measuring areas. Figure 3a gives the distribution of maximum and minimum temperatures in the first 14 s after the test start, 3b after 7th s to 22nd s, while 3c gives the same information in same time interval, but only for minimum temperature changing. Fig 3d gives the temperature in marked areas during time interval 14th to 28th s.

The temperature monitoring during the test by thermography, provides the detection of the initial temperature variation, indicating where the conditions for the crack initiation under the load impact are.

The experiment lasted about 28s. to monitor The minimum temperature is monitored on the surfaces AR01 and AR02, while the maximum temperature values in the AR03 and AR04. The tested sample temperature was in equilibrium with the environment. Ambient temperature was 29 º C. Temperatures recorded at the surface of the sample were in the range of 28-30 º C, which is the result of different surface sample emissivity. Fig 3a shows that there were small variations of temperature in the first 18 s of tensile test. After that there was a sudden rise of temperature, on the right side (AR03 to 37.5 º C) and on the left one (AR04 to 32.5 º C). The right side was broken. The temperature on both sides declined to 30.3 ºC after 3s. In 22.5th seconds (4.5 seconds after the first fracture of the sample) there was a sudden rise of temperature on the left, to the value of 37 º C and fracture of the sample on the left side (fig 3d). The temperature of the sample was 33.5 º C on both sides of the circular hole after 3 s, and it remained to the end of the test.

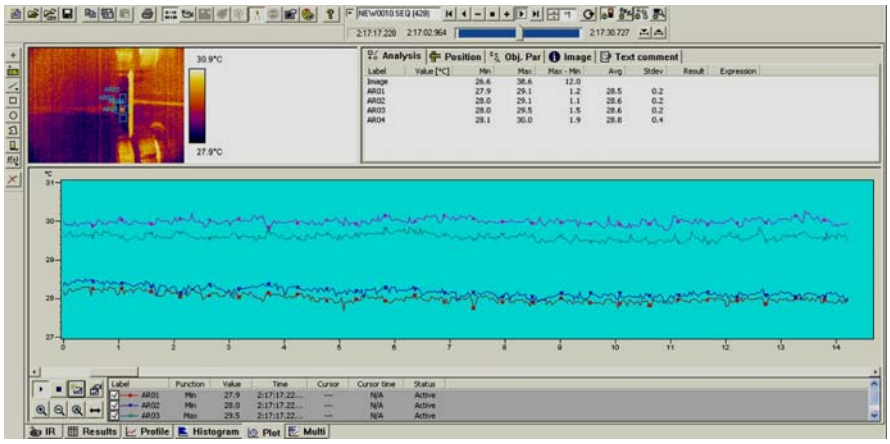

a

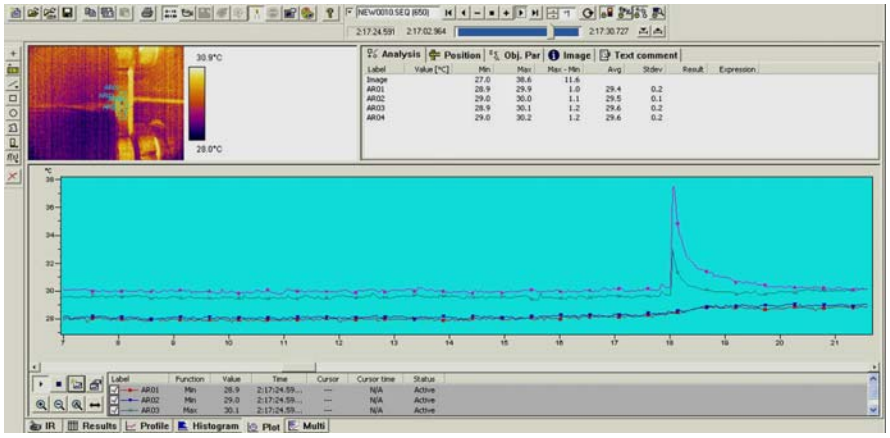

b

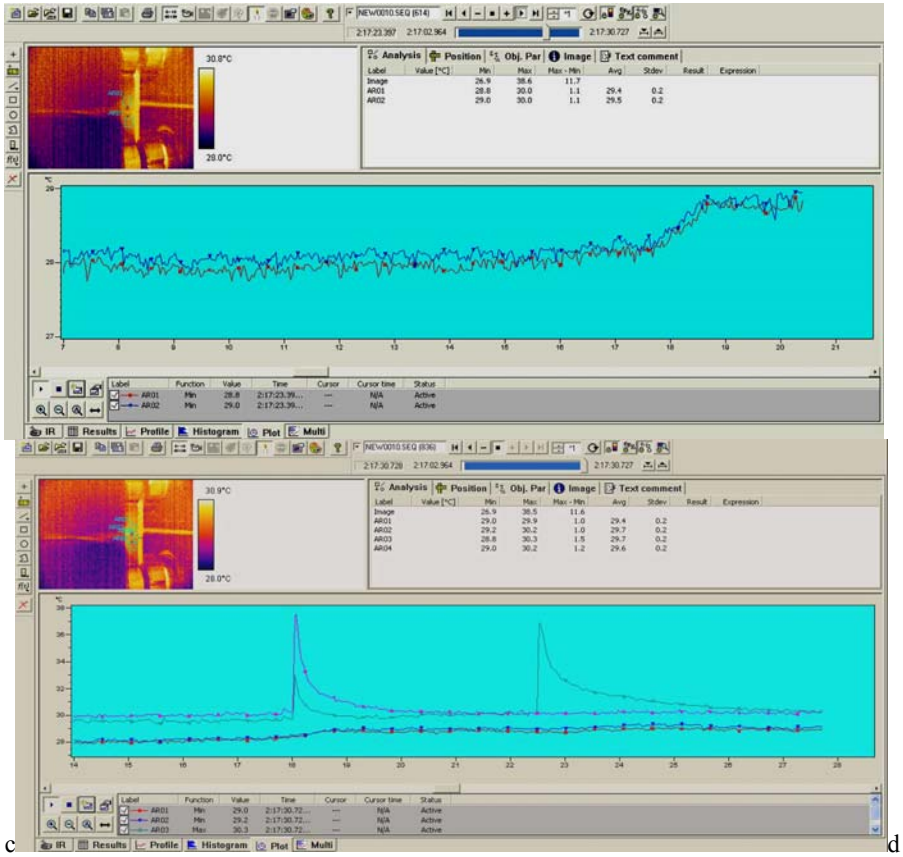

c d

Figure 3. The temperature around the hole on the surface of the structural steel specimen

At the same time, the minimum temperatures in the zones AR01 and AR02 ware changed. The temperature rose from 28 to 28.8 ° C at the time of first fracture and that value is retained until the end of the experiment (fig 3c and 3d).

Fig.4 shows the diagrams of stress vs. extension and maximum temperature vs. time on the surface of the sample. Some characteristic points are illustrated with corresponding thermograms: the beginning of elastic deformation, the beginning of plastic deformation, reaching maximum force, the homogeneous plastic deformation to the final fracture of the specimen.

The analysis of the results presented in Fig.4 shows that in the first 18 seconds the force reaches 42 kN. The temperature of the sample was not changed and elastic deformation occurred within the specimen. The total elongation is 1, 5 mm. The increase in force of only a few N leads to the appearance of plastic deformation and fracture of right side. The maximum stress in that moment was 8.954 N/m^2. From 18s to 19,5s, the temperature decreases from 310,8K to 303,6K on the right and from 306 to 303,4K on the left side. The

specimen total elongation in 22th s was 1,85mm. Then a rapid increase in temperature occurs on the left side of circular hole. Immediately before 23th s, the left side was cracked. The total elongation of the sample was 1,9mm. This value of elongation is measured after the test (fig 2a). Figures 4a-4c show stress distribution for a plate in tension containing a centrally located hole, under applied uniform stress.

It is evident that, crack initiation is a highly localized event which is strongly affected by the random distribution of material properties and defects that exist at the micro structural level. The temperature monitoring during thermography test provide the detection of the initial temperature changes, indicating where are conditions for appearance and growth of cracks under the load impact.

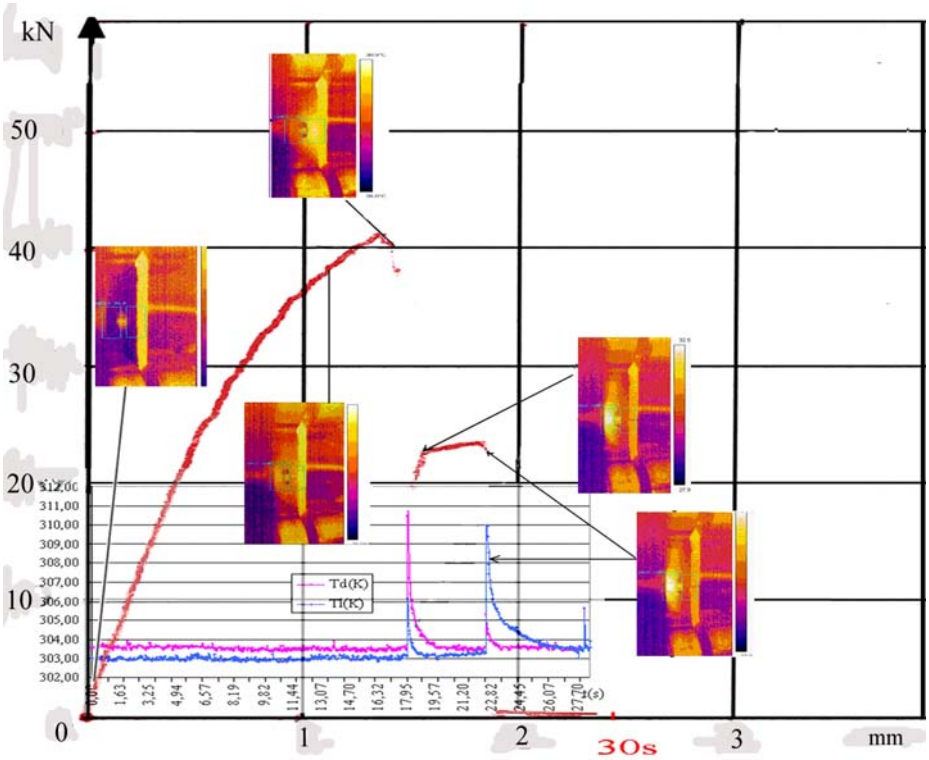

Figure 4. Flow chart of tested specimens

4. Numerical simulation

Stress analysis of hole in plate specimen is made with FEM. It is an efficient and reliable numerical procedure for modeling both, linear and nonlinear behavior of materials and structures [ ]. Numerical method FEM has been used in order to confirm the ability of thermography to predict the crack of spacemen. Elastoplastic, numerical analysis of the hole in plate made of structural steel is made. The primary aim was to obtain the maximum

strain that correspond to the experiment. The finite tetrahedron type element and model specimen with finite element mesh are shown in fig.5 and fig.6.

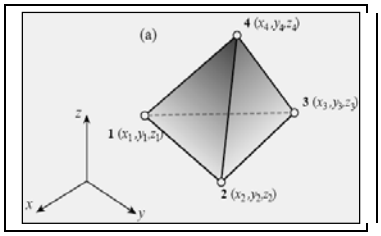

Figure 5. Finite element type tetrahedron

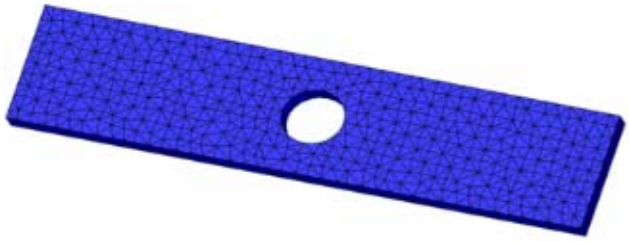

Figure 6. Model specimen with finite element mesh before tensile test

Finite element mesh is consisted of 6,178 elements and 11,099 nodes with three degrees of freedom, so the system has a total of 33,297 equations. A global stiffness matrix system of finite element meshes in this case has 33297 x 33297elements. Using equations which link displacement and strain, and the equations of deformation and stress, stress distribution is determined. External load were entered into the model on the front surface of the board, while the other plate wedged.

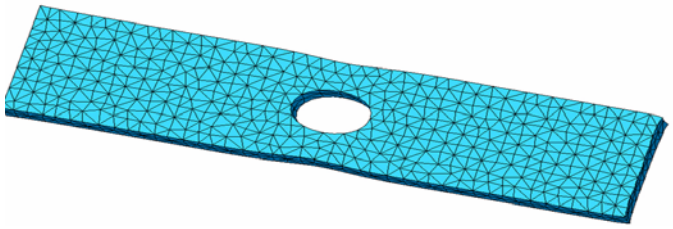

Figure 7. Model specimen with finite element mesh after tensile test

Specimen with the Von Mises stresses is shown in Fig. 8.

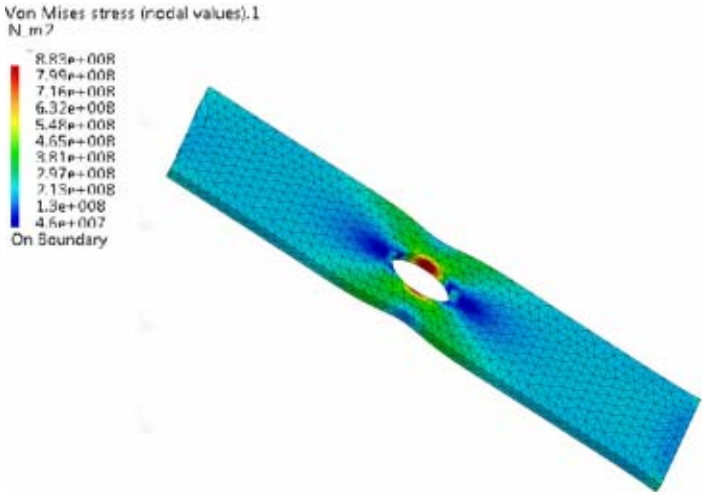

Figure 8. Tensile test simulation, specimen with the Von Mises stresses,

The highest stress in the plate, around the hole, is $8.83 \cdot 10^8$ N/m^2 (Fig. 9). Numerical results demonstrate a good agreement with experiment ($8.95 \cdot 10^8$ N/m^2). The static stress concentration factor in the elastic range, K_t, is defined as the ratio of the maximum stress, σ_{max}, to the nominal stress, s_{nom}. For the infinite plate containing a hole and loaded in tension, $K_t = 3$. [10]. As the width of the plate decreases, the maximum stress becomes less than three times the nominal stress at the zone containing the hole.

The zoomed part of specimen around the hole with Von Miss stress distribution is presented in fig. 9.

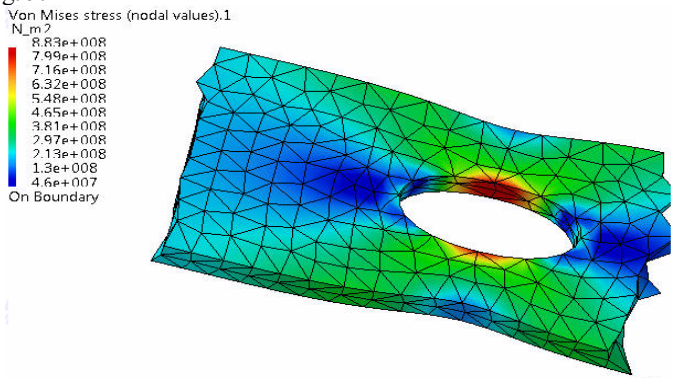

Figure 9. Increase part of specimen with the field of stress

Figure 10 shows the point with the maximum stress, where the initiation of crack started, while figure 11 show temperature distribution in left area of specimen (AR03) based on recorded thermogram immediately before crack.

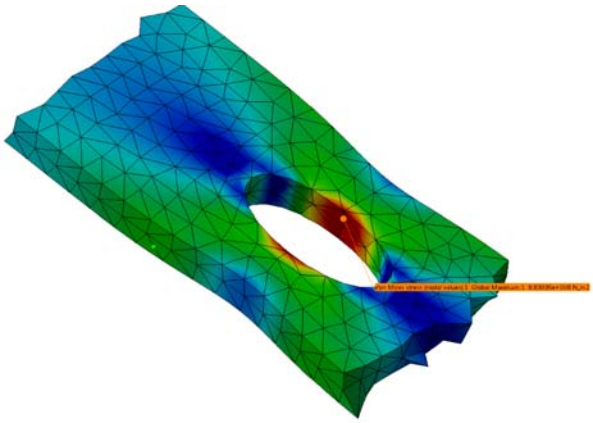

Figure 10. Point with maximum of stress

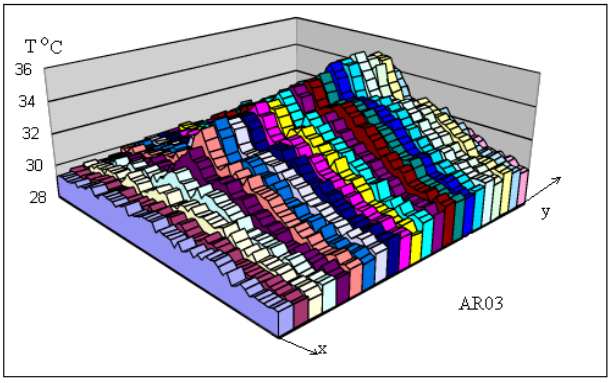

Figure 11. Temperature distribution in left area of specimen (AR03) based on recorded thermogram

5. Conclusion

The experiments and results of thermography application, simultaneously with the conventional methods, for testing the tensile properties of metal spacemen with complex shape are presented. The main aim of testing was to relate the temperature changes of the spacemen, continuously recorded by thermography, with stress – extension diagram. As a conclusion can be pointed out that:

-The obtained results confirm that it is very useful to use thermography for early diagnostics of the complex structures in the exploitation or service conditions.

-This technology enables conducting stress analysis and estimation of fatigue limits in a nondestructive and non-contact method within a shorter period. The tensile test allowed obtaining visible data of surface stress distribution using thermography. The numerical simulation determined the maximum stress value and distribution, which was very similar to experimentally obtained.

-This proves that the variations in temperature captured by the IR camera were strongly correlated to the stress and strain as result of loads applied to the specimens.
-The results, considered in this paper, show that its can be used for someone quickly to make a conclusion that critical zone appeared in that place if the temperature increase.
-Thermography provides simple and fast location of the defects in the material which could be the spots of the potential cracks initiation and growth.
-Infrared thermography has proven to be an invaluable tool to solve a wide range of scientific questions and problems related to the reliable assessment of the structure integrity and life time.

Acknowledgments

The authors would like to thank the Ministry of Science and Technological Development of Serbia for financial support under the project number TR 34028A.

6. References

1. Harwood, N., and Cummings, W.M., Thermoelastic Stress Analysis, (1991), IOP Publishing ltd, Adam Hilger imprint, Bristol
2. Maldague, X. P., (1993), Nondestructive evaluation of materials by infrared thermography, Springer-Verlag, London
3. Flir Systems, The Ultimate Infrared Handbook for R&D Professionals
4. Luong, M.P., (1998), Fatigue limit evaluation of metals using an infrared thermographic technique", Mechanics of Materials, vol. 28, pp. 155-163
5. Man-Yong C., Jung-Hak P., Ki Soo K., Won-Tae K., (2006), Application of Thermography to analysis of thermal stress in the NDT for compact tensile specimen, Proceedings of 12th A-PCNDT 2006 – Asia-Pacific Conference on NDT, Auckland, New Zealand, 2006.
6. Kutin M., Ristić S., Puharić M.a, Burzić Z., (2010), Tensile features of steel spacemen testing by thermography, Scientific Technical Review, Vol 60 , br.1 , Beograd, pp.66-70
7. Kutin M., Ristić S., Radović N., Vasović I., (2010), Application of thermography to analysis of thermal. stress for compact tensile specimen, 4th International Conference PROCESSING AND STRUCTURE OF MATERIALS (PSM4), Palic, Serbia 27 to 29 May, pp.171-177
8. Castanedo, C., (2005), Quantitative subsurface defect evaluation by pulsed phase thermography, depth retrieval with the phase, Thèse (Ph.D.), Faculté des sciences et de génie université laval québec.
9. Petkovic Z. , (2005), Metalne konstrukcije u mašinogradnji, Metal structures in the machine building 2, MF Belgrade
10. Roark's Formulas for Stress and Strain Ch-17 (www.eBookByte.com)
11. Salvatore S. Ligarò and Paolo S. Valvo, (2000), Stress distribution around discontinuities in soft elastic membranes**,** Computational Methods for Shell and Spatial Structures IASS-IACM 2000, M. Papadrakakis, A. Samartin and E. Onate (Eds.), ISASR-NTUA, Athens, Greece
12. Bojić N., Jugović Z., Popović M., Uticaj oblika otvora na naponsko stanje delova mašinskih konstrukcija pri jednoosnomzatezanju ploča**,** IMK-14 Istraživanje i razvoj, Godina XVI, Broj (35) 2/2010, pp.17-22
13. http://www.openfoam.com/docs/user/plateHole.php
14. Cozzens R., (2008), Catia V5 version 17, SDC publication

Forward and inverse kinematics for vertical 5-axis turning center with angular head of non-intersectional axes, with compensation for table moving caused by base thermal dilatation

Vladimir Kvrgić[1],Jelena Vidaković[1], Vladimir Kaplarević[1], Mihailo Lazarević[2]

[1] Lola Institute, Kneza Višeslava 70a 11030 Belgrade,
e-mail: vladimir.kvrgic@li.rs,
vidakovic.jelena@gmail.com , vladimir.kaplarevic@li.rs
[2] Faculty of Mechanical Engineering,
The University of Belgrade, Kraljice Marije 16, 11120 Belgrade 35
e-mail: mlazarevic@mas.bg.ac.rs

Abstract. The paper presents the solution for forward and inverse kinematics of the vertical 5-axis turning centers with 2 linear and 3 rotational axes (C_y, X, Z, B_t and C_t) which for the 5-axis milling achieves the motion accomplished by 3 linear and 2 rotational axes (X, Y, Z, B_t and C_y). It has been done in such a way to provide for machine motion programming as if machining were performed on a 5-axis gantry milling machine. This has essentially facilitated machine programming, because tool positions and orientations required for programming are determined disregarding the workpiece swiveling during machining and current positions and orientations taken by the tool during machining relative to the workpiece. Turning center has a 2-rotary-axis head with axes C_t and B_t which do not intersect. This type of angular head has increased the possibilities of machining and allowed for performing certain types of machining without machine's taking the singular positions, but it has made the machine control algorithm more complex. A high number of rotating of the table, required for turning, causes heating of the table bearing support and base thermal dilatation. If milling or drilling is done immediately after turning, the table and X axis motion control should be corrected to eliminate the error in machining appeared due to dilatation, as has been done in this paper.
Keywords: Vertical five-axis turning centers; Forward and inverse kinematics; Thermal errors

1. Introduction

Nowadays, the precision and productivity that users demand from 5-axis machining of complex workpiece surfaces is gradually increasing. To satisfy this requirement different structures of the 5-axis machines are developed. The machine denominations, where L is a linear axis and R is a rotation axis, will be given now. LLLRR-The cutting tool is supported by a two-rotary-axis head, one for head rotation and another for tool tilting. This configuration is used in large gantry machine tools. RRLLL-The workpiece is supported by a double turning table, i.e. the work table has two rotational axes. This configuration is commonly used in small compact machines or in machines with auxiliary rotary tables. RLLLR-The workpiece is supported by a rotary turning table and the tool has one rotational degree of freedom (swivelling head).

The present paper deals with the control algorithm development for vertical 5-axis turning centre, where the work table becomes the axis of auxiliary motion (C_y axis), whose swivelling, with cutting tool motion along the X axis according to the corresponding law, produces motion corresponding to the motion along the Y axis, not existing here. The ram carrying turning tools is replaced by the turning, drilling and milling unit for rotating tools. By addition of the replaceable two-axis angular head to this unit, the 5-axis milling and drilling is possible to achieve. This way, a machine with 2 linear and 3 rotational axes was obtained, which for the 5-axis machining achieves the motion accomplished by 3 linear and 2 rotational axes. A machine with C_y, X, Z, B_t and C_t axes, the RLLRR machine type, was thus obtained.

In the control algorithm given in this paper, the compensation for error caused by machine base thermal dilatation has been carried out, because it is the biggest error and because it is very difficult to eliminate it by corresponding structure, cooling and mounting. When workpiece turning is performed with a large number of revolutions there occurs a substantial heating of the work table bearing support. The bearing support temperature is transferred to the machine base, causing its thermal dilatation. This causes the table rotational axis shift by a few tenths of a millimetre. The work table moving along the X and Y axes (δ_{xc} and δ_{yc}) has impact on milling and drilling accuracy. To eliminate the influence of the work table thermal dilatation on machining accuracy, real-time measurements and machine control algorithm correction are required, as has been done in this paper.

Control algorithm of a vertical 5-axis turning centre was integrated into its control system, developed at Lola Institute too. The control system was obtained by extending the Lola-Industrial Robot Language [1] with commands for machine tool, by integration of the new solutions for forward and inverse kinematics of this machine in this control system and by adapting of its trajectory planner to novel commands for tool moving.

In this paper, forward and inverse kinematics has been solved for such machine with an angular head, where axes do not intersect (Fig. 1). Such angular head increases the machining possibilities and helps to avoid singularity positions of the machine work table. Some possible singular positions of the work table have been discussed. Control algorithm for the work table and C_t axis has been given, eliminating their singular positions.

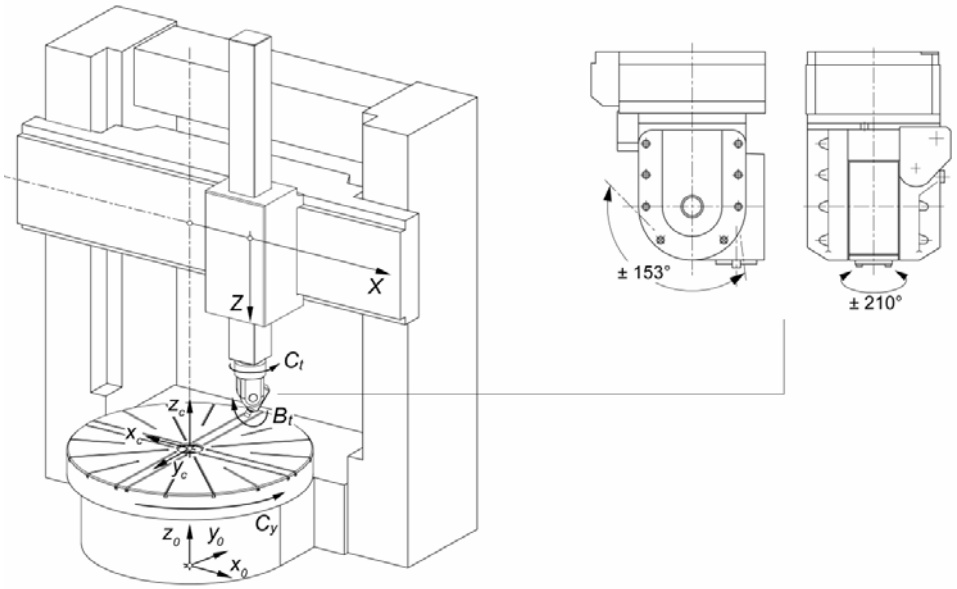

Figure 1. Vertical 5-axis turning center with two axis head.

2. Coordinate frames of machine components and matrices determining their relations

This section defines coordinate frames for the components of vertical 5-axis turning centre and matrices determining their relations. Machine components, their links and coordinate frames are denoted using the Denavit-Hartenberg convention (D-H) [2,3,4]. The machine is viewed as a system consisting of two entities performing cooperative motion; one entity comprises a work table with a workpiece, swivelling according to a certain law, and another is a serial mechanism with 2 translational and 2 rotational axes, carrying the cutting tool. (Fig. 2) shows frames for machine components. The machine base is denoted by *0*, and the last serial component by *4*. The table rotation by angle *c* is denoted with C_y. The first 2 serial links are translational and another 2 rotational, so the corresponding translatory movements d_1 and d_2 and angles θ_3 and θ_4 are variables. It was adopted that the angle θ_3 is positive when the component's 3 rotation is in the negative mathematical direction, and that the angles θ_4 and *c* are positive when the component's 4 rotation and the rotating table is in the positive mathematical direction. D-H parameters of machine components are given in Tab. 1.

Table 1 D-H parameters of vertical 5-axis turning centre components

Link	Variable	a [mm]	a_y [mm]	d [mm]	α [°]	θ [°]
1-Z	d_1	*0*	*0*	d_{1c}	$\alpha_1=90, \alpha'_1=90$	$\theta_{1a}=90$
2-X	d_2	*0*	*0*	*0*	*0*	*0*
3	$(-)\theta_3$	a_3	*0*	*0*	$\alpha_3=90$	$\theta_{3a}=90$
4	θ_4	*0*	*0*	*0*	$\alpha_4=-90$	*0*
5-C_y	*C*	δ_{xc}	δ_{yc}	*0*	*0*	*0*

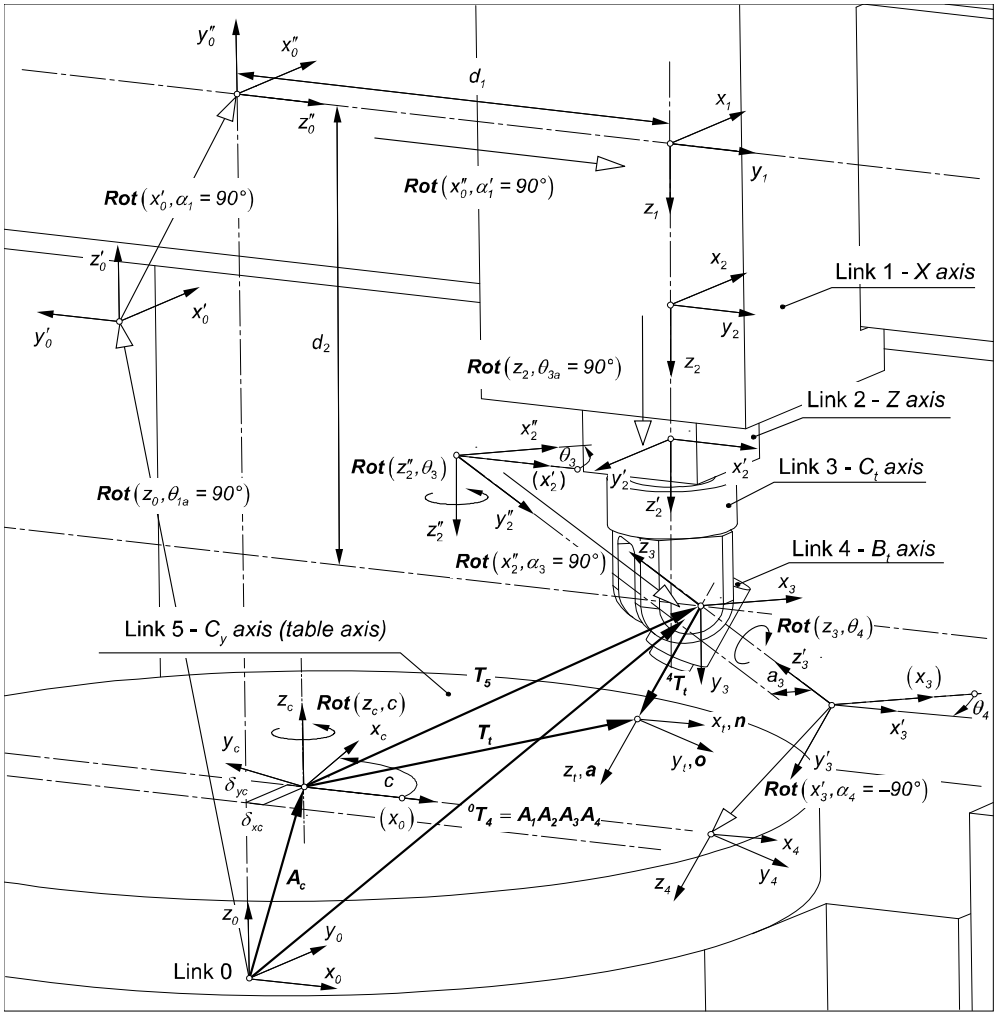

Figure 2. Coordinate frames of vertical 5-axis turning centre components.

The homogenous matrix that transforms the coordinates of a point from frame $x_n y_n z_n$ to frame $x_m y_m z_m$ is denoted by ${}^{n}\boldsymbol{T}_{m}$. The homogenous transformation describing the relation between one link and the next is called $\boldsymbol{A}_i=\boldsymbol{A}(i\text{-}1,i)$ matrix [4]. The following homogenous matrices for the coordinate frames of the machine links are defined to derive the kinematic equations for the machine:

$$\boldsymbol{A_1} = \boldsymbol{A}(0,1) = \boldsymbol{Trans}(z_0, d_{1c})\boldsymbol{Rot}(z_0, \theta_{1a})\boldsymbol{Rot}(x'_0, \alpha_1)\boldsymbol{Trans}(z''_0, d_1)\boldsymbol{Rot}(x''_0, \alpha'_1)$$

$$\boldsymbol{A_2} = \boldsymbol{A}(1,2) = \boldsymbol{Trans}(z_1, d_2)$$

$$\boldsymbol{A_3} = \boldsymbol{A}(2,3) = \boldsymbol{Rot}(z_2, \theta_{3a})\boldsymbol{Rot}(z''_2, \theta_3)\boldsymbol{Trans}(x''_2, a_3)\boldsymbol{Rot}(x''_2, \alpha_3)$$

$$\boldsymbol{A_4} = \boldsymbol{A}(3,4) = \boldsymbol{Rot}(z_3, \theta_4)\boldsymbol{Rot}(x'_3, \alpha_4)$$

By using the convenient shorthand notation $sin(\varphi)=s_\varphi$ and $cos(\varphi)=c_\varphi$ the transformation matrices defined above are written as follows:

$$\boldsymbol{A_1}=\begin{bmatrix} 0 & 1 & 0 & d_1 \\ 1 & 0 & 0 & 0 \\ 0 & 0 & -1 & d_{1c} \\ 0 & 0 & 0 & 1 \end{bmatrix}, \boldsymbol{A_2}=\begin{bmatrix} 1 & 0 & 0 & 0 \\ 0 & 1 & 0 & 0 \\ 0 & 0 & 1 & d_2 \\ 0 & 0 & 0 & 1 \end{bmatrix},$$

$$\boldsymbol{A_3}=\begin{bmatrix} s_3 & 0 & c_3 & s_3 a_3 \\ c_3 & 0 & -s_3 & c_3 a_3 \\ 0 & 1 & 0 & 0 \\ 0 & 0 & 0 & 1 \end{bmatrix}, \boldsymbol{A_4}=\begin{bmatrix} c_4 & 0 & -s_4 & 0 \\ s_4 & 0 & c_4 & 0 \\ 0 & -1 & 0 & 0 \\ 0 & 0 & 0 & 1 \end{bmatrix},$$

$$\boldsymbol{A_c}=\begin{bmatrix} c_c & -s_c & 0 & \delta_{xc} \\ s_c & c_c & 0 & \delta_{yc} \\ 0 & 0 & 1 & 0 \\ 0 & 0 & 0 & 1 \end{bmatrix}. \qquad (1)-(5)$$

3. Programming of the machine

5-axis programs are generated by CAD/CAM systems or, manually, by G codes. Programming of the milling operations on the vertical 5-axis turning centre is performed in the movable working table coordinate system $x_cy_cz_c$ and not in the machine basic coordinate system $x_0y_0z_0$ (Fig. 2).

In programming by G codes the tool orientation is given in Euler angles or RPY angles via A_t, B_t, and C_t (in degrees) or by the tool direction vector which points from the tool tip towards the toolholder. If we define the approach vector $\boldsymbol{a}=a_{x5}\boldsymbol{i}+a_{y5}\boldsymbol{j}+a_{z5}\boldsymbol{k}$, where $\boldsymbol{i}$, $\boldsymbol{j}$ and $\boldsymbol{k}$ are unit vectors along the x_c, y_c and z_c coordinate axes of the rotating table, which lies in the z_t direction from which the tool approaches the workpiece (Fig. 2), the components of the tool direction vector would be: $-a_{x5}$, $-a_{y5}$ and $-a_{z5}$.

The output of the CAM systems is cutter locations, X_t, Y_t, Z_t, $-a_{x5}$, $-a_{y5}$ and $-a_{z5}$, which define the tool positions and the tool direction vectors with respect to the workpiece coordinate system given in the CL data file [5,6,3]. The tool path between two CL points is a straight line relative to the workpiece. CL motion commands from the CL data file are further converted in motion commands of the NC program (in G code).

Afterward, the tool path, given in NC program, is converted in the sequence of consecutive positions of all machine axes that will produce the desired tool location (inverse kinematics). The calculation of inverse kinematics can be performed either by the CAD/CAM system, by the post-processor or by the NC unit. The control system developed in Lola Institute for vertical 5-axis turning centre calculates complete path interpolation and inverse kinematics in real time.

4. Forward kinematics

The forward kinematics is used to calculate the tool position and orientation X_t, Y_t, Z_t, B_t and C_t from the machine axis variables: c, d_1, d_2, θ_3 and θ_4. In vertical 5-axis turning centre we will determine the position and orientation of the component 4 and the tool relative to the rotating table. It is obvious from (Fig. 2) that the component 4 position and orientation relative to the machine base is given by the equation ${}^0\boldsymbol{T}_4=\boldsymbol{A}_1\boldsymbol{A}_2\boldsymbol{A}_3\boldsymbol{A}_4$ and relative to the rotating table by the equation

$$\boldsymbol{T}_5=\begin{bmatrix} n_{x5} & o_{x5} & a_{x5} & X_5 \\ n_{y5} & o_{y5} & a_{y5} & Y_5 \\ n_{z5} & o_{z5} & a_{z5} & Z_5 \\ 0 & 0 & 0 & 1 \end{bmatrix}=\boldsymbol{A}_c^{-1}\boldsymbol{A}_1\boldsymbol{A}_2\boldsymbol{A}_3\boldsymbol{A}_4= \tag{6}$$

$$=\begin{bmatrix} c_c c_{34}+s_c s_3 c_4 & c_c s_3-s_c c_3 & -c_c c_3 s_4-s_c s_{34} & X_5 \\ -s_c c_{34}+c_c s_3 c_4 & -s_c s_3-c_c c_3 & s_c c_3 s_4-c_c s_{34} & Y_5 \\ -s_4 & 0 & -c_4 & Z_5 \\ 0 & 0 & 0 & 1 \end{bmatrix}$$

where is: $X_5=c_c(d_1+c_3a_3-\delta_{xc})+s_c(s_3a_3-\delta_{yc})$,

$Y_5=-s_c(d_1+c_3a_3-\delta_{xc})+c_c(s_3a_3-\delta_{yc})$, $Z_5=d_{1c}-d_2$

Tool position relative to the rotating table is determined by matrix:

$$\boldsymbol{T}_t=\boldsymbol{T}_5\,{}^4\boldsymbol{T}_t=\boldsymbol{T}_5\begin{bmatrix} 1 & 0 & 0 & -r_t \\ 0 & 1 & 0 & 0 \\ 0 & 0 & 1 & l_t \\ 0 & 0 & 0 & 1 \end{bmatrix} \tag{7}$$

Here l_t is length, r_t is radius and ${}^4\boldsymbol{T}_t$ is tool position matrix relative to the component 4 (Fig. 2). In an initial position it is: $c=\theta_3=\theta_4=C_t=B_t=0°$,

$$\boldsymbol{T}_t=\begin{bmatrix} 1 & 0 & 0 & d_1-r_t \\ 0 & -1 & 0 & 0 \\ 0 & 0 & -1 & d_{1c}-d_2-l_t \\ 0 & 0 & 0 & 1 \end{bmatrix} \tag{8}$$

Now, using the tool orientation matrix terms [***n o a***], obtained by Eq. (6), tool orientation angles will be determined.

4.1. Calculations of the RPY tool orientation angles

There follows the analysis and discussion of the solutions used to calculate angles $-90°\le B_t\le 90°$ and $-180°\le C_t\le 180°$ defined by RPY orientation angles. Tool orientation matrix for

RPY angles and for the case when $A_t=180°$ reads:
$ORIZYX(C_t,B_t,A_t)$ = $\mathbf{Rot}(z,C_t)$ $\mathbf{Rot}(y,B_t)$ $\mathbf{Rot}(x,A_t)$, i.e.

$$\begin{bmatrix} n_{x5} & o_{x5} & a_{x5} \\ n_{y5} & o_{y5} & a_{y5} \\ n_{z5} & o_{z5} & a_{z5} \end{bmatrix} = \begin{bmatrix} c_{C_t}c_{Bt} & s_{C_t} & -c_{C_t}s_{Bt} \\ s_{C_t}c_{Bt} & -c_{C_t} & -s_{C_t}s_{Bt} \\ -s_{Bt} & 0 & -c_{Bt} \end{bmatrix} \tag{9}$$

From here it is obtained $\mathbf{Rot}(z,C_t)^{-1}$ $[\mathbf{n\ o\ a}]$ = $\mathbf{Rot}(y,B_t)$ $\mathbf{Rot}(x,A_t)$, i.e.

$$\begin{bmatrix} c_{C_t}n_{x5}+s_{C_t}n_{y5} & c_{C_t}o_{x5}+s_{C_t}o_{y5} & c_{C_t}a_{x5}+s_{C_t}a_{y5} \\ -s_{C_t}n_{x5}+c_{C_t}n_{y5} & -s_{C_t}o_{x5}+c_{C_t}o_{y5} & -s_{C_t}a_{x5}+c_{C_t}a_{y5} \\ n_{z5} & o_{z5} & a_{z5} \end{bmatrix} = \begin{bmatrix} c_{B_t} & 0 & -s_{B_t} \\ 0 & -1 & 0 \\ -s_{B_t} & 0 & -c_{B_t} \end{bmatrix} \tag{10}$$

and $[\mathbf{n\ o\ a}]$ $\mathbf{Rot}(x,A_t)^{-1}$ $\mathbf{Rot}(y,B_t)^{-1}$ = $\mathbf{Rot}(z,C_t)$,

$$\text{i.e.} \begin{bmatrix} c_{B_t}n_{x5}-s_{B_t}a_{x5} & -o_{x5} & -s_{B_t}n_{x5}-c_{B_t}a_{x5} \\ c_{B_t}n_{y5}-s_{B_t}a_{y5} & -o_{y5} & -s_{B_t}n_{y5}-c_{B_t}a_{y5} \\ c_{B_t}n_{z5}-s_{B_t}a_{z5} & -o_{z5} & -s_{B_t}n_{z5}-c_{B_t}a_{z5} \end{bmatrix} = \begin{bmatrix} c_{C_t} & -s_{C_t} & 0 \\ s_{C_t} & c_{C_t} & 0 \\ 0 & 0 & 1 \end{bmatrix} \tag{11}$$

Using terms of the matrix Eqs. (9), (10) and (11), it is possible to determine the angles B_t and C_t in a few ways. These solutions will be analyzed now. Some solutions differ mutually by $\pm 180°$, however, in some cases, when the argument of a function *atan2* reads *0,0* inaccurate results are obtained, which are inapplicable.

The solutions of equations that yield values of the angles B_t and C_t will be analyzed using Eq. (9) to obtain tool orientation angle, by virtue of known values for these angles. Afterward, using the terms of this matrix, orientation angles will be calculated. Only solutions that for each tool orientation position yield solutions equal to starting tool orientation angles will be adopted.

4.1.1. Calculations of the angle B_t

The terms (3,1) and (3,3) of matrix Eqs. (9) and (10) yield:

$$B_t = atan2(-n_{z5}, -a_{z5}) \tag{12}$$

This solution is independent of the angle C_t, while the components n_{z5} and a_{z5} (Fig. 3) of the argument of a function *atan2* are not simultaneously equal to zero in any position of the tool, which would result in ambiguity or inaccurate solution. Consequently, this solution gives an accurate result in any tool position.

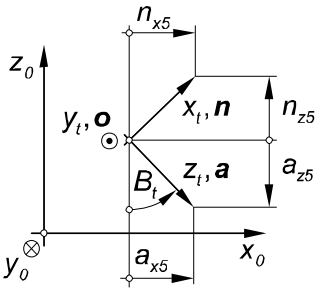

Figure 3. Tool orientation vectors.

If calculations for the angle B_t are done after those for the angle C_t, then other expressions can be also used. Using terms (1,3) and (3,3) or (1,3) and (1,1) or (3,1) and (1,1), respectively, of Eq. (10) the expressions (13), (14) and (15) can be obtained. Like the expression (12), the expressions (13), (14) and (15) always yield accurate results.

$$B_t = atan2(-c_{C_t} a_{x5} - s_{C_t} a_{y5}, -a_{z5}) \tag{13}$$

$$B_t = atan2(-c_{C_t} a_{x5} - s_{C_t} a_{y5}, c_{C_t} n_{x5} + s_{C_t} n_{y5}) \tag{14}$$

$$B_t = atan2(-n_{z5}, c_{C_t} n_{x5} + s_{C_t} n_{y5}) \tag{15}$$

The term (1,3) of Eq. (11) (Fig. 3) yields the solutions

$$B_t = atan2(a_{x5}, -n_{x5}) \quad \text{and} \quad B_t = atan2(-a_{x5}, n_{x5}) \tag{16), (17}$$

The values for these two solutions differ mutually by $\pm 180°$. If $C_t \in (90°, 180°]$ or if $C_t \in (-90°, -180°]$ an accurate result is obtained by Eq. (16), and if $C_t \in (-90°, 90°)$ an accurate result is obtained by Eq. (17). However, for the values of $C_t = -90°$ and $C_t = -90°$, the components n_{x5} and a_{x5} are always equal to zero. Therefore, these two equations are inapplicable in these cases.

The term (2,3) of Eq. (11) gives the solutions

$$B_t = atan2(a_{y5}, -n_{y5}) \quad \text{and} \quad B_t = atan2(-a_{y5}, n_{y5}) \tag{18), (19}$$

The values for these solutions also differ mutually by $\pm 180°$. If $C_t \in (0°, 180°)$, an accurate result is obtained by Eq. (19), and if $C_t \in (0°, -180°)$ an accurate result is obtained by Eq. (18). However, for the values of $C_t = 0°$ and $C_t = 180°$, the components n_{y5} and a_{y5} are always equal to zero. Therefore, these two equations in these two cases are inapplicable.
Sine of the angle B_t can be calculated, for the known value of the angle C_t, using the terms (1,3) or (2,3) of Eq. (9), therefore $sin(B_t) = -a_{x5}/c_{Ct}$ or $sin(B_t) = -a_{y5}/s_{Ct}$. Cosine of the angle B_t can be calculated, in this case, using the terms (1,1) or (2,1) of mentioned equation, therefore $cos(B_t) = n_{x5}/c_{Ct}$ or $cos(B_t) = n_{y5}/s_{Ct}$. However, using these terms does not always yield accurate results, and in some cases there occurs division by zero, so these terms are not suitable for calculations of the angle B_t.

4.1.2. Calculations of the angle C_t

The terms (1,2) and (2,2) of Eq. (11) give

$$C_t = atan2(o_{x5}, -o_{y5}) \tag{20}$$

The components o_{x5} and o_{y5} of the argument of a function *atan2* are independent of the angle B_t, they always lie in the x_0y_0 plane ($o_{z5}=0$) and are never simultaneously equal to zero. Therefore, the expression (20) can be used to calculate the angle C_t.

When the value of angle B_t is known, the angle C_t can be calculated using the expressions obtained by the terms (2,1) and (1,1) or (1,2) and (1,1) or (2,2) and (1,1) of Eq. (11), respectively.

$$C_t = atan2(c_{B_t} n_{y5} - s_{B_t} a_{y5}, c_{B_t} n_{x5} - s_{B_t} a_{x5}) \tag{21}$$

$$C_t = atan2(o_{x5}, c_{B_t} n_{x5} - s_{B_t} a_{x5}) \tag{22}$$

$$C_t = atan2(c_{B_t} n_{y5} - s_{B_t} a_{y5}, -o_{y5}) \tag{23}$$

Like Eq.(20), the Eqs. (21, 22 and 23) always yield accurate results.

The term (2,3) of Eq. (10) gives the solutions

$$C_t = atan2(a_{y5}, a_{x5}) \text{ and } C_t = atan2(-a_{y5}, -a_{x5}) \tag{24), (25}$$

The values of these two solutions differ mutually by $\pm 180°$. If $B_t \in [-90°, 0°)$ accurate results are obtained by Eq. (24), and if $B_t \in [0°, 90°)$ accurate results are obtained by Eq. (25). However, for $B_t = 0°$ the components a_{x5} and a_{y5} are always equal to zero. Hence, these two equations in this case are inapplicable.

The term (1,2) of Eq. (10) gives the solutions

$$C_t = atan2(n_{y5}, n_{x5}) \text{ and } C_t = atan2(-n_{y5}, -n_{x5}) \tag{26), (27}$$

If $B_t \in (-90°, 90°)$ Eq. (26) yields an accurate result, while Eq. (27) yields the result differing by $\pm 180°$. However, for $B_t = \pm 90°$, the components n_{x5} and n_{y5} are always equal to zero. Consequently, these two equations in this case are inapplicable.

5. Inverse kinematics

The inverse kinematics is used to determine the set of axis variables c, d_1, d_2, θ_3 and θ_4 that will produce the desired cutter location (X_t, Y_t, Z_t, $-a_{x5}$, $-a_{y5}$ and $-a_{z5}$) given in the CL data file, or X_t, Y_t, Z_t, C_t and B_t given in G codes. Control unit primarily utilizes the inverse kinematics. In this case, during machining in each interpolation period, i.e. for each interpolated point of motion, it determines the cutting tool position and orientation relative to the swivelling table, respectively movable work table coordinate system. This section discusses some possible machine singular positions. Control algorithms are given for the work table and the axis C_t that eliminate their singular positions.

Here we will determine machine component positions in virtue of its tool position relative to the rotating table (C_y axis) given by the matrix $\boldsymbol{T}_t$, Eq. (7). The component 4 position relative to the rotating table is defined by the expression:

$$\boldsymbol{T}_5 = \boldsymbol{T}_t\, {}^4\boldsymbol{T}_t^{-1} \tag{28}$$

This way, for tool orientation defined by RPY and for $A_t=180^\circ$ the preceding equation reads:

$$\boldsymbol{T}_5 = \begin{bmatrix} c_{C_t}c_{B_t} & s_{C_t} & -c_{C_t}s_{B_t} & c_{C_t}c_{B_t}r_t + c_{C_t}s_{B_t}l_t + X_t \\ s_{C_t}c_{B_t} & -c_{C_t} & -s_{C_t}s_{B_t} & s_{C_t}c_{B_t}r_t + s_{C_t}s_{B_t}l_t + Y_t \\ -s_{B_t} & 0 & -c_{B_t} & -s_{B_t}r_t + c_{B_t}l_t + Z_t \\ 0 & 0 & 0 & 1 \end{bmatrix} \tag{29}$$

Multiplying both sides of Eq. (6) by the matrix $\boldsymbol{A}_c$ on the left side we obtain Eq. $\boldsymbol{A}_c\boldsymbol{T}_5 = {}^0\boldsymbol{T}_4 = \boldsymbol{A}_1\boldsymbol{A}_2\boldsymbol{A}_3\boldsymbol{A}_4$, i.e.

$$\begin{bmatrix} c_c n_{x5} - s_c n_{y5} & c_c o_{x5} - s_c o_{y5} & c_c a_{x5} - s_c a_{y5} & c_c X_5 - s_c Y_5 + \delta_{xc} \\ s_c n_{x5} + c_c n_{y5} & s_c o_{x5} + c_c o_{y5} & s_c a_{x5} + c_c a_{y5} & s_c X_5 + c_c Y_5 + \delta_{yc} \\ n_{z5} & o_{z5} & a_{z5} & Z_5 \\ 0 & 0 & 0 & 1 \end{bmatrix} =$$

$$= \begin{bmatrix} c_{34} & s_3 & -c_3 s_4 & d_1 + c_3 a_3 \\ s_3 c_4 & -c_3 & -s_{34} & s_3 a_3 \\ -s_4 & 0 & -c_4 & d_{1c} - d_2 \\ 0 & 0 & 0 & 1 \end{bmatrix} \tag{30}$$

Multiplying Eq. (30) consecutively by $\boldsymbol{A}_1^{-1}$, then by $\boldsymbol{A}_2^{-1}$ and lastly by $\boldsymbol{A}_3^{-1}$ on the left side we obtain Eq. $\boldsymbol{A}_3^{-1}\boldsymbol{A}_2^{-1}\boldsymbol{A}_1^{-1}\boldsymbol{A}_c\boldsymbol{T}_5 = {}^3\boldsymbol{T}_4 = \boldsymbol{A}_4$, i.e.

$$\begin{bmatrix} .... & .... & s_3(s_c a_{x5} + c_c a_{y5}) + c_3(c_c a_{x5} - s_c a_{y5}) & .... \\ .... & .... & -a_{z5} & .... \\ .... & .... & c_3(s_c a_{x5} + c_c a_{y5}) - s_3(c_c a_{x5} - s_c a_{y5}) & .... \\ 0 & 0 & 0 & 1 \end{bmatrix} = \begin{bmatrix} c_4 & 0 & -s_4 & 0 \\ s_4 & 0 & c_4 & 0 \\ 0 & -1 & 0 & 0 \\ 0 & 0 & 0 & 1 \end{bmatrix} \tag{31}$$

5.1. Calculation of the angle c

The term (2,4) of Eq. (30) reads:

$$s_c X_5 + c_c Y_5 + \delta_{yc} = s_3 a_3 \tag{32}$$

The term (1,2) of Eq. (30) yields $s_3 = c_c o_{x5} - s_c o_{y5}$ (33)

The terms (2,3) and (3,1) of Eq. (30) yield $s_3 = (s_c a_{x5} + c_c a_{y5}) / n_{z5}$ (34)

The terms (2,1) and (3,3) of Eq. (30) yield $s_3 = (-s_c n_{x5} - c_c n_{y5}) / a_{z5}$ (35)

It is possible to calculate s_3 only by the help of the components of vector $\boldsymbol{a}$, obtained from CL data file, but in this case it is needed to have the information on the sign of the angle θ_4. Namely, for $\theta_4 \neq 0°$, the terms (2,3) and (3,3) of Eq. (30) yield

$$s_3 = (-s_c a_{x5} - c_c a_{y5}) \Big/ (sign(\theta_4) \sqrt{1 - a_{z5}^2}) \quad (36)$$

and for $\theta_4 = 0°$ is $s_3 = 0$.

Now, Eq. (32) can be written in the following form:

$$\frac{tan(c)}{\sqrt{1 + tan^2(c)}} p_x + \frac{p_y}{\sqrt{1 + tan^2(c)}} = -\delta_{yc} \quad (37)$$

Eqs. (33) and (37) yield $p_x = X_5 + o_{y5}\, a_3$ and $p_y = Y_5 - o_{x5}\, a_3$ (38)

Eqs. (34) and (37) yield $p_x = X_5 - a_{x5}\, a_3 / n_{z5}$ and $p_y = Y_5 - a_{y5}\, a_3 / n_{z5}$ (39)

Eqs. (35) and (37) yield $p_x = X_5 + n_{x5}\, a_3 / a_{z5}$ and $p_y = Y_5 + n_{y5}\, a_3 / a_{z5}$ (40)

Eqs. (36) and (37) yield $p_x = X_5 + a_{x5}\, a_3 \Big/ (sign(\theta_4) \sqrt{1 - a_{z5}^2})$ and

$p_y = Y_5 + a_{y5}\, a_3 \Big/ (sign(\theta_4) \sqrt{1 - a_{z5}^2})$ for $\theta_4 \neq 0°$ (41)

and $p_x = X_5$ and $p_y = Y_5$ for $\theta_4 = 0°$.

Eq. (37) can be written in the form $p_x\, tan(c) + p_y = -\delta_{yc} \sqrt{1 + tan^2(c)}$ and

$p_x^2 tan^2(c) + p_y^2 + 2 p_x p_y tan(c) = \delta_{yc}^2 (1 + tan^2(c))$ i.e.

$(p_x^2 - \delta_{yc}^2) tan^2(c) + 2 p_x\, p_y\, tan(c) + p_y^2 - \delta_{yc}^2 = 0$.

The solution for the preceding equation is

$: c = arctan((-p_x p_y \pm \sqrt{p_x^2 p_y^2 - (p_x^2 - \delta_{yc}^2)(p_y^2 - \delta_{yc}^2)}) / (p_x^2 - \delta_{yc}^2)$.

As the table swivelling angle decreases with the table moving in the direction of the y_o axis, caused by thermal dilatations ($\delta_{yc} > 0$), the sign – will be adopted in the preceding expression, such that:

$$c_{90} = a\tan 2(-p_x p_y - \delta_{yc} \sqrt{p_x^2 + p_y^2 - \delta_{yc}^2}\,,\, p_x^2 - \delta_{yc}^2) \quad (42)$$

The table swivelling angle c in the expression (42) is denoted by c_{90} for the reason that this

expression always gives angle c in the range [$-90°$,$90°$], except when $p_x^2 < \delta_{yc}^2$, which is a special case. For the case when the angular head axes intersect, $a_3=0$, and there is no thermal dilatation, $\delta_{yc}=0$, the solution for Eq. (32) would read: $c=atan2(-Y_5,X_5)$.

5.1.1. Algorithm for calculations of the angle c

The X axis feed will be limited so that the cutting tool moves from the table axis to the maximum positive value. To achieve this, and given that the value of X_5 can be negative too, the table swivelling angle c should be in the minimum range of [$-180°$,$180°$]. In order to reduce the additional positioning of the workpiece and angular head during milling, the range of [$-360°+c_{90}$,$360°+c_{90}$] will be adopted for the table swivelling angle c. Hence, it is necessary to extend the range of the angle c, obtained by the expression (42), from [$-90°$,$90°$] to [$-360°+c_{90}$,$360°+c_{90}$]. To achieve this, but also to avoid uncontrolled work table swivelling in singular positions by approximately $\pm 180°$ or $\pm 360°$, this paper proposes a novel algorithm for calculating the angle c. It consists of three steps presented below.

Step 1. Step 1 involves the calculations of the angle c for the case without thermal dilatation. The range of the angle c obtained here is [$-180°$,$180°$]. For $\delta_{yc}=0$, the expression (42) reads:

$$c = a\tan 2(-p_y, p_x) \tag{43}$$

Let angle c be denoted by c_{prev} for the previous interpolation period. The angle c increment for the next interpolation period will be

$$\Delta c = c - c_{prev} \tag{44}$$

Step 2. In Step 2 it is checked if the value of the angle c, calculated in Step 1 for a single interpolation period, changes by approximately $\Delta c \pm 180°$ or $\Delta c \pm 360°$. The procedure is presented, which makes this impossible and which, if necessary, extends the range of the angle c from [$-180°$,$180°$] to [$-360°$,$360°$]. For calculations of the angle c in the next interpolation step, the value will be assigned to $c_{prev}=c$.

Step 3. In Step 3 the angle c is determined for the case if $\delta_{yc} \neq 0$. First, in virtue of the expression (42) the value of the angle c_{90} is calculated. Using this and the value of the angle c obtained in Step 2, the range of the angle c is extended from [$-90°$,$90°$] to [$-360°+c_{90}$,$360°+c_{90}$].

The difference between the angle c_{90} obtained by the expression (42) and the angle c calculated in Step 2 will be denoted by

$$\Delta c_{90} = c_{90} - c \tag{45}$$

Now, the value of the table swivelling angle (c_{90}) will be corrected by $\pm 180°$ or by $\pm 360°$ as follows:
If $\Delta c < -7\pi/4$, then $c=c_{90}+2\pi$,

If $\Delta c \in [-\pi/4,-5\pi/4]$, then $c=c_{90}+\pi$,
If $\Delta c \in [\pi/4,5\pi/4]$, then $c=c_{90}-\pi$,
If $\Delta c > 7\pi/4$, then $c=c_{90}-2\pi$,
Else $c=c_{90}$;

Note: If $p_x^2 + p_y^2 < \delta_{yc}^2$ in the expression (42), the discriminate of the argument of a function in this expression (42) being smaller than zero, therefore its argument is not a real number. In this case, the solution does not exist for angle c that will lead the surface of machining to the machine X axis. It should be waited for the table base to cool and for the table axis to return to the zero position.

5.2. Work table singular positions

A special issue associated with rotary axes is the problem of singular configuration. Sometimes the singular configuration represents the borderline between two possible solutions for the inverse kinematics, but most often the singular configuration is at the end position of one of the rotary axes. The problem with the singularity is that the C axis sometimes has to make a quick turn, often $\pm 180°$, in order to produce the desired tool motion. In the subsection 5.1.1. the algorithm given prevents the work table to swivel by $\pm 180°$ or $\pm 360°$, in a single interpolation period.
This algorithm has also extended the table swivelling range to $[-360° + c_{90}, 360° + c_{90}]$, whereby many singular positions were avoided as well.

Some possible singular positions of the work table have still remained. They will be discussed now. Analyzing the expression (42), it is noticeable that in some specific situations, in order to correct motion caused by thermal dilatation δ_{yc}, the work table swivelling occurs by $\pm 180°$ or $\pm 90°$ in short time intervals. These singular positions will be presented below.

1. If $p_x=0$, then $c = atan2(-\sqrt{p_y^2 - \delta_{yc}^2}, -\delta_{yc})$. This entails that for the case when $p_y \to \delta_{yc}$, and for $\delta_{yc}>0$, there holds $c \to 180°$, and for $\delta_{yc}<0$, it holds $c \to 0°$. If $p_y \le \delta_{yc}$, the discriminate $D = p_y^2 - \delta_{yc}^2$ is smaller than or equal to zero, therefore the assigned motion is not achievable.
2. If $p_y=0$, then $c = atan2(-\delta_{yc}, \sqrt{p_x^2 - \delta_{yc}^2})$. This entails that for the case when $p_x \to \delta_{yc}$ and for $\delta_{yc}>0$, there holds $c \to 90°$, and for $\delta_{yc}<0$, it holds $c \to 90°$. If $p_x \le \delta_{yc}$, the discriminate $D = p_x^2 - \delta_{yc}^2$ is smaller than zero, therefore the assigned motion is not achievable.
3. A special case of machining is when $p_y=0$ and $\delta_{yc}=0$. Then $c=atan2(0,p_x)$ holds, so in changing the sign of the parameter p_x, there occurs the table swivelling by the angle of $\pm 180°$. Table swivelling is performed here at programmed velocity and programmed acceleration, while the remaining 4 axes do not rotate. The control algorithm itself provides for further continuation of motion along the X axis in a positive direction.

During previous 3 motions the machine passes through singular points, so abrupt table swivelling occurs. Owing to the two-axis angular head with the axis that do not intersect it is possible in singular position to change its orientation in the way to change the angle C_t for $\pm 180°$ and to change the sign of the angle B_t. This will change the parameters p_x and p_y in Eq. (42), and thereby avoid work table singular positions.

5.3. Calculations of the angle θ_3

The angle θ_3, similar to the angle C_t, as described in subsection 4.2.2, can be calculated in a number of ways. In case that programming is done in G code and if tool orientation is assigned by the angles B_t and C_t, using Eq. (9), we can calculate tool orientation matrix coefficients. Afterward, using terms (1,2) and (2,2) of Eq. (30), we can calculate the angle θ_3 by the equation:

$$\theta_3 = atan2(c_c o_{x5} - s_c o_{y5}, -s_c o_{x5} - c_c o_{y5}) \tag{46}$$

In 4.1.2. it has been shown that components o_{x5} and o_{y5} of the argument of a function *atan2* do not depend on the angle B_t, that they always lie in the x_0y_0 plane and that they are never simultaneously equal to zero. Hence, for this case, the expression (46) can be used for calculations of the angle θ_3. When the table swivelling angle c equals zero, the expression (20) used to calculate the angle C_t is identical to the expression (46), which now reads: $\theta_3 = atan2(o_{x5}, -o_{y5})$.

As mentioned in section 3, when CAD/CAM system is used in programming, its output are the assigned tool position and direction vector $\boldsymbol{a}$ given in the CL data file. This means that in this case in order to determine the machine axis position all 9 tool orientation matrix terms cannot be used, but only the components a_{x5}, a_{y5} and a_{z5}. The term (3,3) of Eq. (31) yields

$$\theta_3 = atan2(s_c a_{x5} + c_c a_{y5}, c_c a_{x5} - s_c a_{y5}) \tag{47}$$

And:

$$\theta_3 = atan2(s_c a_{x5} + c_c a_{y5}, c_c a_{x5} - s_c a_{y5}) \tag{48}$$

Previous 2 equations, for the case when the work table swivelling angle c equals zero, are identical to Eqs. (24) and (25). As mentioned in 4.1.2. the values of these two solutions mutually differ by $\pm 180°$. For $B_t = 0°$ the components a_{x5} and a_{y5} equal zero, so Eq. (47) always yields $\theta_3 = 0°$, while Eq. (48) always gives here $\theta_3 = 180°$, irrespective of the current value of the angle θ_3. Now, we will present the algorithm that will in the application of either of the two previous equations prevent abrupt angular head swivelling around the vertical axis and that will yield solution for the angle θ_3 for $B_t = 0°$. Let θ_{3prev} denote the angle θ_3 in the previous interpolation period.
If $\theta_3 - \theta_{3prev} \in [\pi/2, 3\pi/2]$, then $\theta_3 = \theta_3 - \pi$,
If $\theta_3 - \theta_{3prev} \in [-\pi/2, 3-\pi/2]$, then $\theta_3 = \theta_3 + \pi$,
If $a_{x5} = 0$ and $a_{y5} = 0$, then $\theta_3 = \theta_{3prev}$;

5.4. Calculations of the angle θ_4

When programming is performed in CAD/CAM system, by the help of the CL data file, the angle θ_4 can be calculated using the terms (1,2) and (2,2) of Eq. (31), such that:

$$\theta_4 = a\tan 2(c_3(s_c a_{y5} - c_c a_{x5}) - s_3(s_c a_{x5} + c_c a_{y5}), -a_{z5}) \tag{49}$$

In case that tool orientation is given by the angles B_t and C_t, the angle θ_4 can be calculated in other manner using different terms of Eqs. (30) and (31), such as, e.g.

$$\theta_4 = a\tan 2(-n_{z5}, -a_{z5}) \tag{50}$$

5.5. Calculations of the parameters d_1 and d_2 (the X and Z axes positions)

The term (1,4), Eq. (30), determining motion along the *X* axis yields:

$$X = d_1 = c_c X_5 - s_c Y_5 - c_3 a_3 + \delta_{xc} \tag{51}$$

The term (3,4), Eq. (30), determining motion along the *Z* axis yields:

$$Z = d_2 = d_{1c} - Z_5 \tag{52}$$

This way, using the cutting tool position relative to the work table, matrix $\boldsymbol{T}_t$, by the help of the expressions (42), (46) or (47) or (48), (49) or (50), (51) and (52), respectively, we have calculated the positions c, θ_3, θ_4, d_1 and d_2 of machine

6. Conclusion

It has been shown that on the 5-axis turning centre with 2 linear and 3 rotational axes, besides the turning, it is possible to achieve 5-axis milling, drilling and boring identical to that on the milling machine with 3 linear and 2 rotational axes. Control algorithm allowing for this was presented. Thanks to the proposed control algorithm, machine programming is possible in identical way as done for the 5-axis milling machine, which essentially simplifies writing the machining program or taking over the CL data from CAD/CAM systems developed for the milling machines.
Forward and inverse kinematics has been solved for the case of utilizing the 2-axis angular head with non-intersecting axes, which increases the achievability of machining in some cases. For the case of control of the angular head with intersecting axes, the mentioned algorithm is simplified.

The proposed algorithm fully eliminates the inaccuracy of machining caused due to base thermal extension. Here the solving of the table swivelling angle was a specific problem. The algorithm was given that performs compensation of the base thermal extension error by correcting mentioned angle. Also, this algorithm extends the angle range, so it is greater than $\pm 360°$. Thus, additional positioning of the work table and angular head during machining is decreased.

If necessary, it is possible to incorporate into the control algorithm the compensations for some other errors of the machine, such as, for example, the error caused due to cross-bar deflection carrying the ram with angular head, whose weight is significant.

Acknowledgement. This research is supported by the Ministry of Science and Technological Development of Serbia under the project: Research and development of the new generation of vertical 5-axis turning centre (2008-2010), no. 14026.

References

[1] M. Pavlović (1994) L-IRL: High Level Programming Language for Robots, *Proceedings of the European Robotics and Intelligent Systems Conference, Malaga, Spain*, V. Kvrgić, D. Velašević, (Eds.).
[2] A. Lamikiz (2007) The Denavit and Hartenberg approach applied to evaluate the consequences in the tool tip position of geometrical errors in five-axis milling centres, *Int J Adv Manuf Technol* DOI **10**.1007/s00170-007-0956-5, L.N. López de Lacalle, O. Ocerin, D. Díez & E. Maidagan, (Eds.).
[3] R.S. Lee and Y.H. Lin (2010) Development of universal environment for constructing 5-axis virtual machine tool based on modified D–H notation and OpenGL, *Robotics and Computer-Integrated Manufacturing* **26** 253–262.
[4] R.P. Paul (1984) *Robot manipulators: Mathematics, Programing and Control*, The MIT Press, Cambrigde MA.
[5] R.S. Lee and C.H. She (1997) Developing a postprocessor for three types of five-axis machine tools. *Int J Adv Manuf Technol* **13(9)**: 658–665.
[6] K. Sørby (2007) Inverse kinematics of five-axis machines near singular configurations, *International Journal of Machine Tools & Manufacture* **47** 299–306.